

**INVESTIGATION ON DIELECTROPHORETIC ASSEMBLY OF NANOSTRUCTURES
AND ITS APPLICATION ON CHEMICAL SENSORS**

by

Quan Tao

Bachelor of Science, Nanjing University of Aeronautics and Astronautics, China, 2009

Master of Science, University of Pittsburgh, 2011

Submitted to the Graduate Faculty of
Swanson School of Engineering in partial fulfillment
of the requirements for the degree of
Doctor of Philosophy in Electrical Engineering

University of Pittsburgh

2015

UNIVERSITY OF PITTSBURGH
SWANSON SCHOOL OF ENGINEERING

This dissertation was presented

by

Quan Tao

It was defended on

April 20th, 2015

and approved by

Mahmoud El Nokali, Ph.D, Associate Professor, Department of Electrical and Computer
Engineering

Kevin P. Chen, Ph. D, Associate Professor, Department of Electrical and Computer
Engineering

Ching-Chung Li, Ph.D, Professor, Department of Electrical and Computer Engineering

Mingui Sun, Ph.D, Professor, Department of Neurological Surgery, Department of Electrical
and Computer Engineering

Dissertation Director: Guangyong Li, Ph.D, Associate Professor, Department of Electrical
and Computer Engineering

Copyright © by Quan Tao

2015

**INVESTIGATION ON DIELECTROPHORETIC ASSEMBLY OF
NANOSTRUCTURES AND ITS APPLICATION ON CHEMICAL SENSORS**

Quan Tao, PhD

University of Pittsburgh, 2015

Because of their extraordinary characteristics such as quantum confinement and large surface-to-volume ratio, semiconducting nanostructures such as nanowires or nanotubes hold great potential in sensing chemical vapors. Nanowire or nanotube based gas sensors usually possess appealing advantages such as high sensitivity, high stability, fast recovery time, and electrically controllable properties. To better predict the composition and concentration of target gas, nanostructures made from heterogeneous materials are employed to provide more predictors. In recent years, nanowires and nanotubes can be synthesized routinely through different methods. The techniques of fabricating nanowire or nanotube based sensor arrays, however, encounter obstacles and deserve further investigations. Dielectrophoresis (DEP), which refers to the motion of submicron particles inside a non-uniform electric field, has long been recognized as a non-destructive, easily implementable, and efficient approach to manipulate nanostructures onto electronic circuitries. However, due to our limited understandings, devices fabricated through DEP often end up with unpredictable number of arbitrarily aligned nanostructures.

In this study, we first optimize the classical DEP formulas such that it can be applied to a more general case that a nanostructure is subjected to a non-uniform electric field with arbitrary

orientation. A comprehensive model is then constructed to investigate the trajectory and alignment of DEP assembled nanostructures, which can be verified by experimental observations. The simulation results assist us to fabricate a gas sensor array with zinc oxide (ZnO) nanowires and carbon nanotubes (CNTs). It is then demonstrated that the device can well sense ammonia (NH_3) at room temperature, which circumvents the usually required high temperature condition for nanowire based gas sensor application. An effective approach to recover the device using DC biases to locally heat up the nanostructures is then proposed and implemented to accelerate the recovery process of the device without the requirement of heating up the whole device. As the sensors are characterized under different NH_3 concentrations, the outputs are analyzed using regression methods to estimate the concentration of NH_3 . The quadratic model with the lasso is demonstrated to provide best performance for the collected data.

TABLE OF CONTENTS

1.0	INTRODUCTION.....	1
1.1	MOTIVATION AND OBJECTIVE	2
1.2	DISSERTATION ORGANIZATION.....	3
2.0	BACKGROUND	5
2.1	NANOWIRE BASED GAS SENSOR.....	5
2.1.1	ZnO nanowire based gas sensor	6
2.1.2	Carbon nanotube (CNT) based gas sensor.....	8
2.1.3	Nanowire based gas sensor array.....	9
2.2	DIELECTROPHORESIS	10
3.0	DEP ASSEMBLY OF SINGLE NANOWIRE IN 2-D SPACE	17
3.1	DEP FORCE AND DEP TORQUE ON NANOWIRE IN 2-D SPACE.....	17
3.1.1	Optimization on DEP force and DEP torque.....	17
3.1.2	Frequency and conductivity dependence of DEP force	19
3.2	INVESTIGATION ON TRAJECTORY AND ALIGNMENT OF NANOWIRE ASSEMBLED BY DEP	22
3.2.1	Hydrodynamic drag force and drag torque	22
3.2.2	Brownian motion	24
3.2.3	Trajectory of DEP controlled nanowire	26

3.2.4	Alignment of DEP controlled nanowire.....	29
3.2.5	Experimental validation.....	37
4.0	DEP ASSEMBLY OF SINGLE NANOWIRE IN 3-D SPACE	44
4.1	3-D MODELING ON NANOWIRE.....	44
4.1.1	DEP force and DEP torque.....	44
4.1.2	Hydrodynamic drag force and drag torque	46
4.1.3	Rigid body dynamics	48
4.2	SIMULATION STUDIES BASED ON 3-D MODELING.....	55
4.2.1	Numerical simulation of nanowire’s trajectory	55
4.2.2	Determining the boundary for successful alignment by simulation	59
5.0	NANOWIRE BASED GAS SENSOR ARRAY.....	65
5.1	FABRICATION OF NANOWIRE BASED GAS SENSOR ARRAY	65
5.2	GAS SENSING SYSTEM SETUP.....	67
5.3	ZNO NANOWIRE AND CNT BASED NH ₃ SENSOR.....	69
5.3.1	ZnO nanowire based NH ₃ sensor	70
5.3.2	CNT based NH ₃ sensor.....	72
5.4	NANOWIRE BASED GAS SENSOR ARRAY	73
5.5	ESTIMATION OF NH ₃ CONCENTRATION	78
5.5.1	Model selection.....	79
5.5.2	Quadratic model and regularization.....	83
6.0	DISCUSSION	91
7.0	CONCLUSION.....	94
	BIBLIOGRAPHY.....	96

LIST OF TABLES

Table 1 Estimated boundary in x axis for each vertical plane (in unit of μm).....	61
Table 2 Estimated boundaries for three different situations in the vertical plane along the electrodes	63
Table 3 Response of two sensors at different concentrations of NH_3	78
Table 4 Prediction and relative error of quadratic model and quadratic model with ridge regression on both training set and test set	87

LIST OF FIGURES

Figure 1. Schematics of (a) chemiresistor and (b) chemical FET configurations of nanowire based gas sensor. Red dots indicate adsorbed gas molecules.	6
Figure 2. Machine learning in gas sensing scenario. The gas type classification is achieved by pattern recognition procedure, while the gas concentrations are estimated by non-linear regression technique.....	10
Figure 3. Schematic showing a dielectric particle translates in a non-uniform electric field.	11
Figure 4. Schematic showing a homogeneous prolate ellipsoidal particle with semi-axes a , b , and c is subjected to an electric field \mathbf{E}	14
Figure 5. Schematic showing a homogeneous prolate ellipsoidal particle with semi-axes a , b , and c is subjected to an electric field \mathbf{E} in x - y plane.....	16
Figure 6. Even discretization of the nanowire to calculate the DEP force and DEP torque.....	19
Figure 7. (a) The magnitude of the electric field \mathbf{E} . (b) The magnitude of the gradient form $\nabla \mathbf{E} ^2$. (c) The vector plot of the electric field \mathbf{E} . (d) The vector plot of the gradient form $\nabla \mathbf{E} ^2$	20
Figure 8. (a) The DEP force that a 10 μm -long, 60 nm in diameter nanowire receives under the electric field generated by rectangular electrodes versus frequency; (b) The DEP force that a 3 μm -long, 200 nm in diameter nanowire receives under the electric field generated by triangular electrodes versus frequency.....	21
Figure 9. (a) Decomposition of the velocity to calculate the drag force. (b) Discretization of the nanowire to obtain the total drag torque.	23
Figure 10. Representation of a nanowire in global $x - y$ coordinate and local $x - y$ coordinate.	25
Figure 11. (a) Trajectory of a 10- μm -long nanowire. (b) Trajectory of a 5- μm -long nanowire. .	28
Figure 12. The nanowire contacts one electrode.	30

Figure 13. Electric field distribution generated by a pair of triangular electrodes with 4 μm gap. (a) The magnitude of the electric field \mathbf{E} . (b) The magnitude of the gradient form $\nabla \mathbf{E} ^2$. (c) The vector plot of the electric field \mathbf{E} . (d) The vector plot of the gradient form $\nabla \mathbf{E} ^2$	32
Figure 14. Alignments of nanowires with different lengths onto 1 μm gap electrodes. (a) 1- μm -long nanowire. (b) 3- μm -long nanowire. (c) 5- μm -long nanowire. (d) 7- μm -long nanowire.....	33
Figure 15. Alignments of nanowires with different lengths onto 4 μm gap electrodes. (a) 3- μm -long nanowire. (b) 5- μm -long nanowire. (c) 7- μm -long nanowire. (d) 10- μm -long nanowire.....	34
Figure 16. (a) Comparison of nanowires orientation with electric field and gradient of electric field directions at different positions. (b) A zoomed-in view of two nanowires that closet to the end of the electrodes.	35
Figure 17. Fabrication process of microelectrodes.	38
Figure 18. AFM image of a pair of electrodes with a gap smaller than 1 μm . Right figure is a zoomed-in view of left one.	39
Figure 19. SEM image of synthesized ZnO nanowires before suspension. Scale bar is 5 μm for figure, and 0.5 μm for inset.....	40
Figure 20. AFM images of electrodes with ZnO nanowires assembled (Dashed red lines indicate predicted alignments of ZnO nanowires at the corresponding positions).....	41
Figure 21. AFM images of electrodes with CNTs assembled (Dashed red lines indicate predicted alignments of CNTs at the corresponding positions).....	42
Figure 22. Discretization of the nanowire in 3-D space to characterize the DEP force, DEP torque and the torque generated by DEP forces.....	46
Figure 23. Decomposition of the velocity to calculate the drag force on the nanowire.	47
Figure 24. Even discretization of the nanowire to estimate the drag torque in 3-D space.	48
Figure 25. The motion of single nanowire in 3D space.....	49
Figure 26. The electric field distribution generated by triangular electrodes in the vertical XOZ plane. (a) The magnitude of the electric field \mathbf{E} . (b) The magnitude of the gradient form $\nabla \mathbf{E} ^2$. (c) The vector plot of the electric field \mathbf{E} . (d) The vector plot of the gradient form $\nabla \mathbf{E} ^2$	55
Figure 27. (a) The trajectory of nanowire starting from (0, 0, 30) μm . (b) The final alignment of the nanowire.....	57

Figure 28. (a) The trajectory of nanowire starting from (30, 0, 30) μm . (b) The final alignment of the nanowire.....	58
Figure 29. Initial positions of nanowire considered in the simulation.....	60
Figure 30. Different views of the whole boundary.....	62
Figure 31. Comparison of the boundaries for three different situations.	64
Figure 32. Electrode array fabricated on a 1 inch \times 1 inch quartz substrate.	67
Figure 33. Gas sensing system setup.	69
Figure 34. AFM images of assembled (a) ZnO nanowires and (b) CNTs on two electrode pairs of the same chip.....	70
Figure 35. Sensing and recovery of ZnO nanowire based NH ₃ sensor.	72
Figure 36. Sensing and recovery of CNT based NH ₃ sensor.	73
Figure 37. I-V curves of sensing elements of the sensor array under different conditions (a) ZnO nanowire (b) CNT.....	75
Figure 38. Conductance-Voltage curves of sensing elements of the sensor array under different conditions (a) ZnO nanowire (b) CNT.....	76
Figure 39. Response of the sensor array in the presence of NH ₃ of different concentrations (a) ZnO nanowire based sensor (b) CNT based sensor.....	77
Figure 40. A schematic display of splitting 16 observations into training set and test set, and 5-fold cross-validation. Numbers are indices of data in Table 3. The observations in orange are held out as validation sets.	82
Figure 41. 5-fold cross-validation was implemented 10 times, each with a different random split of the training data.	83
Figure 42. Comparison between real concentrations of NH ₃ and predicted concentrations using quadratic model on (a) training set (b) test set.....	86
Figure 43. The cross-validation mean squared error for ridge regression predictions, as a function of λ	88
Figure 44. The cross-validation mean squared error for the lasso predictions, as a function of λ	90

PREFACE

The life at the University of Pittsburgh in the past six years has been challenging. I encountered my hard time when everything was frustrating, but I also enjoyed the delightful moments when the simulations and experiments turned out as expected. After overcoming many obstacles, I feel greatly honored to obtain my PhD degree. At this time, I am grateful to all the people that had provided me generous supports and inspirational guidance during my PhD study.

First and foremost, I would like to express my sincere gratitude to my PhD advisor, Professor Guangyong Li for his continuous support and insightful advisory. More importantly, Professor Li has taught me correct attitudes, creative thinking, and hands-on abilities on scientific technologies, which is more important for my career development.

I sincerely appreciate committee members Professor Mahmoud El Nokali, Professor Kevin P. Chen, Professor Ching-Chung Li, and Professor Mingui Sun for their constructive comments.

I also want to thank my colleagues and friends in Pittsburgh, Liming Liu, Fanan Wei, Haitao Yang, Fei Lan, Minlin Jiang, Yicheng Bai, Yaofeng Yue, Chengliu Li, Yuecheng Li, Yaojun Zhang, Haifeng Xu, Xiang Chen, and Yan Fang, for their inspiring discussions and kind help.

Special thanks to A.C. Milan, San Antonio Spurs, and Pittsburgh Steelers for the gorgeous delights they bring all along.

Finally, I want to sincerely thank my dearest girl, Jianing, my parents, and all of my family members for their constant and warmest love, support, and encouragement during my life in the USA.

1.0 INTRODUCTION

Because of the progressive industrialization of the society and modernization of military weapons, the technology of measuring gases is of vital importance to protect soldiers in the battlefields and mining workers underground, and to monitor toxic or flammable gases in suburban and metropolitan areas. Although bulk and thick film semiconducting material based gas sensors have been widely utilized [1-5], people are seeking portable alternatives with better sensitivity. Semiconducting nanowires are promising candidates because of their superb characteristics such as quantum confinement, extremely small size, and large surface-to-volume ratio [6, 7]. Previous studies show that the sensitivity of ZnO nanowire based gas sensors is several orders higher than that of bulk or thin film based gas sensors made from the same material [8]. Moreover, nanowire based gas sensors usually possess other advantages including high stability [9], fast response and recovery time [10, 11], and electrically controllable properties [9-12]. However, nanowire based gas sensors suffer the problem of relative low selectivity [13], which could be addressed by an array of sensors made from heterogeneous materials for multiplex sensing. More types of materials also provide more predictors, or features, to estimate the concentration of target gas. During the past decade, nanowires can be synthesized routinely through different methods [6, 14-17]. The techniques of fabricating nanowire based sensor arrays yet are immature and deserve long-term investigations.

1.1 MOTIVATION AND OBJECTIVE

Stable electrical connections between nanowires and nanoscale circuitry are essential to fabricate nanowire-based sensors. Usually, either a top-down monolithic fabrication or a bottom-up direct assembly is used to make electrical connections. In top-down approach, nanostructures and the front-end electronic circuitry are both fabricated from the same bulk wafer using monolithic fabrication technologies, thus it is easy to integrate the readout circuitry with the sensing elements [18]. However, complex sensing is hindered because of the difficulty to make heterogeneous nanostructures on the same chip. In addition, devices made from top-down approach often suffer from process-induced degradation such as excessive surface traps that significantly reduce the sensitivity of the devices [19]. In bottom-up approach, nanowires are synthesized first and then integrated with electronic circuitry by many kinds of assembly approaches such as dielectrophoretic (DEP) assembly [20-22], fluidic flow-directed assembly [23, 24], and Langmuir-Blodgett assembly [25-27]. The advantage of bottom-up approach is its better control over the quality and properties of nanowires. However, method that allows bottom-up assembly of heterogeneous nanostructures with precise control of number and orientations of nanowires at predetermined locations has not yet been reported [28]. Dielectrophoresis (DEP), which refers to the motion of a dielectric particle inside a non-uniform electric field [29-31], has long been recognized as a non-destructive, easily implementable, and efficient approach to manipulate nanowires. Unfortunately, due to the limited understanding on DEP assembly, people have little control over the nanowires assembled by DEP. Nanowire based gas sensors assembled by DEP often end up with unpredicted number of nanowires aligning at random orientations [22], thus a large variation among devices making the calibration of these devices extremely difficult.

In view of the obstacles in fabricating of nanostructure based sensor arrays, one objective of this work is to explore new nanomanufacturing approach to enable controllable assembly of heterogeneous nanostructures for complex sensing. We first propose comprehensive models in both 2-D and 3-D space to better characterize the underlying mechanism of DEP assembly. Based on the theoretical models, the investigation on the trajectory and final alignment of single nanowire is performed, which provides useful guidance on experimental implementation. The DEP assembly, is then utilized to manipulate different nanowires onto a same chip to construct a gas sensor array.

Gas sensors usually require high temperature to achieve fast sensing and recovery, which is not practical when the power is limited. Another objective of this work is to experimentally achieve sensing and fast recovery of the sensors at room temperature through locally heating up the nanostructures by DC biases. Once the gas sensor array can be repeatedly characterized under different concentrations of target gas, we then calibrate the sensor array based on the collected data to predict the concentration of the target gas using regression methods.

1.2 DISSERTATION ORGANIZATION

While Chapter 1 briefly introduces the background, motivation, and objective of this work and outlines the organization of this dissertation, Chapter 2 reviews the related background on nanowire based gas sensor and the technique of DEP assembly. Chapter 3 describes the theoretical model on nanowire's trajectory in 2-D space. Based on this model, a series of simulation were performed on DEP force and nanowire's trajectory and alignment, which subsequently were consolidated by the experimental observations. Chapter 4 extends the model

that applies to a more realistic situation in 3-D space. The simulation based on the 3-D model not only unveils the trajectory and alignment of single nanowire in 3-D space, but also predicts a neighborhood in which the nanowire is more likely to bridge the electrodes. The finding of this neighborhood is expected to provide practical guidance on using DEP in assembling nanowire based devices. Chapter 5 illustrates experimental details on DEP assembly application on gas sensor array. Different regression methods are then implemented to estimate the concentration of target gas from the collected data. Finally, Chapter 6 discusses the future work and Chapter 7 summarizes the achievements of this work.

2.0 BACKGROUND

2.1 NANOWIRE BASED GAS SENSOR

Since nanowires can be synthesized routinely through different techniques, researchers have performed extensive investigations on nanowire applications. Because of their appealing characteristics such as quantum confinement, large surface-to-volume ratio, and unique crystal structure, nanowires hold great promise in a variety of device applications like chemical sensors [32, 33], light-emitting diodes [34, 35], and field effect transistors (FETs) [36, 37]. In chemical transducer application, the sensing process is fulfilled because of the surface charges that generated by the adsorption of target analytes. A large surface-to-volume ratio indicates a large portion of the nanowire is exposed to gases, which results in high sensitivity of the transducer. And since Debye length is comparable to the small size of the nanowire, a large portion of the nanowire is depleted or accumulated with surface charges, therefore enhancing the sensitivity of the sensor. A small size also implies low diffusion time and short response time to reach adsorption equilibrium. There are two major configurations for nanowire based gas sensors that convert the presence or even concentration of target gases to electrical signals [38]: chemiresistor [39, 40] and back-gated chemical FET [41, 42], as shown in Figure 1. In the chemiresistor configuration, single nanowire or nanowire network bridges two microelectrodes through which the current is conducting. The adsorption of target gas molecules on the surface of nanowires

results in carrier transfer between gas molecules and nanowires, which alters the conductance of the device. The chemical FET has similar configuration except the tuning on the conductance of nanowires between drain and source electrodes by the back-gate electrode. Because of the tuning effect from the back-gate electrode, nanowire based gas sensors in chemical FET structures usually have larger sensitivities than those in chemiresistor configurations. However, from the fabrication perspective, the chemical FETs are more complicated.

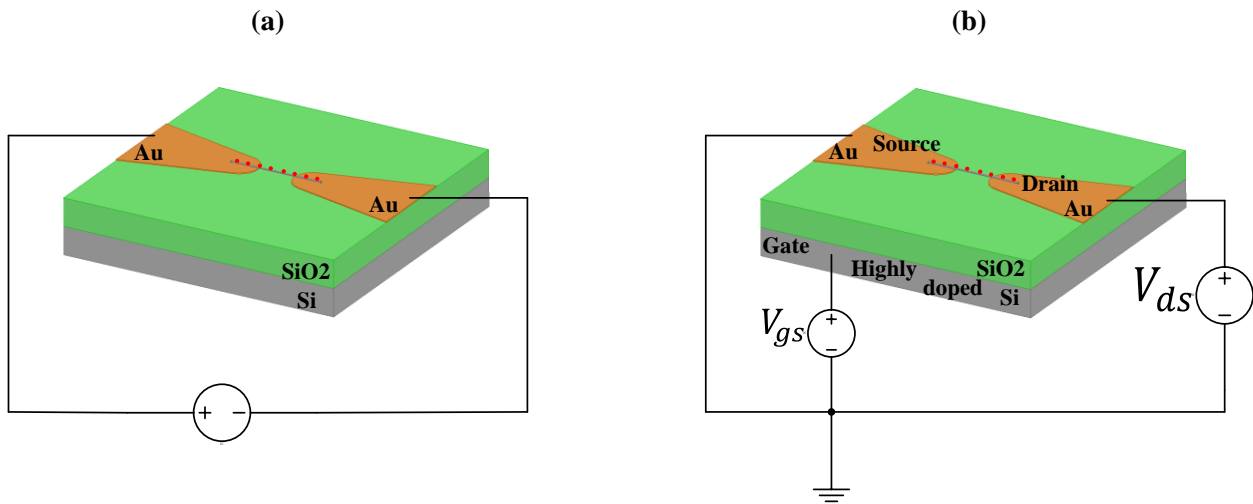


Figure 1. Schematics of (a) chemiresistor and (b) chemical FET configurations of nanowire based gas sensor. Red dots indicate adsorbed gas molecules.

2.1.1 ZnO nanowire based gas sensor

As a chemically stable n-type semiconductor, ZnO has a large exciton binding energy of 60 meV and a wide band gap of 3.4 eV. Because of these appealing properties, ZnO nanowires are widely utilized in the applications of biological and chemical sensors as well as transistors. ZnO

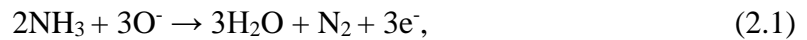
nanowires can be synthesized through two common methods: chemical vapor deposition (CVD), and solution-based method.

For most reported ZnO nanowire growth via CVD method, the vapor-liquid-solid (VLS) process is involved. It is capable of growing aligned ZnO nanowires on sapphire and nitride substrates, such as GaN, AlN, and AlGaN. At a very high temperature (over 900 °C), Zn vapor can be dissolved in an Au catalyst. Zn precipitates are then oxidized to form ZnO nanowires. The growth direction of nanowires is affected by their epitaxial relationship with the substrate. And the quality of nanowires is determined by oxygen partial pressure, chamber pressure, and thickness of catalyst layer [6, 7]. A catalyst-free approach has been reported to grow ZnO nanowires via the precursors Diethylzinc (DEZn) and oxygen gas at relatively low temperature (700 °C) [43]. ZnO nanowires obtained from CVD and metal-organic chemical vapor deposition (MOCVD) have high crystalline qualities, which is of vital importance in the application of solar cells. However, the high working temperature as well as impurity particles around the end of nanowires limit their applications.

The solution-based method is implemented from zinc salts in solution. The hydrolysis of zinc nitrate in water with the introduction of hexamethylenetetramine, and the decomposition of zinc acetate in trioctylamine are two common methods to grow ZnO nanowires via water bath [44]. The much lower temperature for solution-based method provides the possibility to fabricate flexible devices on substrates with low melting points.

While bulk and thin film ZnO has limited sensitivity in detecting chemical gases, ZnO nanowire based gas sensor possesses the advantages of high sensitivity and short response time because of the large surface-to-volume ratio and small size of ZnO nanowires. Previous studies have shown that ZnO nanowires are promising transducers in sensing O₂ [45, 46], H₂ [11, 16,

47], O₃ [47], CO [48, 49], NH₃ [42, 50], NO₂ [41, 51], H₂S [52], and ethanol [10]. The sensing mechanism of ZnO nanowires is related to the interaction of the adsorbed gas molecules and the nanowires, thereby varying the conductance. Oxygen vacancies are common defects in as-grown ZnO nanostructures, which provide more favored adsorption sites for target molecules. Reducing gases, such as CO and NH₃, behave as charge donors to increase the concentration of the major carriers, thereby enhancing the conductance of ZnO nanowires. On the contrary, oxidizing gases, such as NO₂ and O₂, perform as charge acceptors to decrease the concentration of the major carriers, therefore reducing the conductance of ZnO nanowires [53]. Concretely, the interaction between ZnO nanowires and the reducing gas (NH₃) is:



while the interaction between ZnO nanowires and the oxidizing gas (NO₂) is:



2.1.2 Carbon nanotube (CNT) based gas sensor

Since Iijima's discovery of carbon nanotubes (CNTs) in 1991, this one-dimensional nanostructures has been extensively studied in a variety of biological, optical, and electrical applications. Similar to ZnO nanowires, CNTs have also been demonstrated as promising transducers for chemical vapors. However, as a p-type material, CNT based gas sensors behave oppositely compared to ZnO nanowire based gas sensors. Concretely, exposure of CNT to reducing gas (NH₃), results in a decrease of major carrier concentration, consequently a decrease of conductance. On the other hand, the conductance of CNT exposed to oxidizing gas such as NO₂, is supposed to increase because of an enhancement of major carrier concentration [54]. In

addition, the conductance of CNT exposed to ethanol is expected to reduce because of similar mechanism [55].

Different from ZnO nanowires, pristine CNTs, however, are not satisfactory sensing elements for chemical gases other than NH₃, NO₂, and ethanol. Many researchers have performed extensive investigation to improve the sensitivities of CNTs to other common chemical gases. Dai *et al* reported the sensitivity of Pd-decorated CNTs to ppm levels of H₂ gas [56]. Ong *et al* demonstrated the sensitivity of a wireless passive CNT-based gas sensor to CO₂ [57]. Lu *et al* fabricated CH₄ sensors based on CNTs loaded with Pd nanoparticles [58].

2.1.3 Nanowire based gas sensor array

Nanowire based gas sensors have the advantages of much higher sensitivity and stability, and fast response time compared to traditional bulk or thin-film gas sensors. However, the nanowire based gas sensors usually have very low selectivity, which means they can be sensitive to a variety of analytes rather than single specific target gas. For example, many reducing gases such as CO, NH₃, and H₂ can boost the conductance of ZnO nanowires. Because of the so-called cross-sensitivity, one cannot simply tell the presence of a specific chemical gas while observing the variation on the conductance of ZnO nanowires. Consequently, a powerful technique to recognize which gases are the components of the target gases is imperative. In addition, an extension study should be the estimation of the concentrations of the gas components.

To achieve the two challenging goals, researchers have coupled gas sensor arrays with machine learning algorithms to interpret sensor signals and provide classification and regression capabilities [13, 59]. The scenario for both classification and regression is depicted in Figure 2.

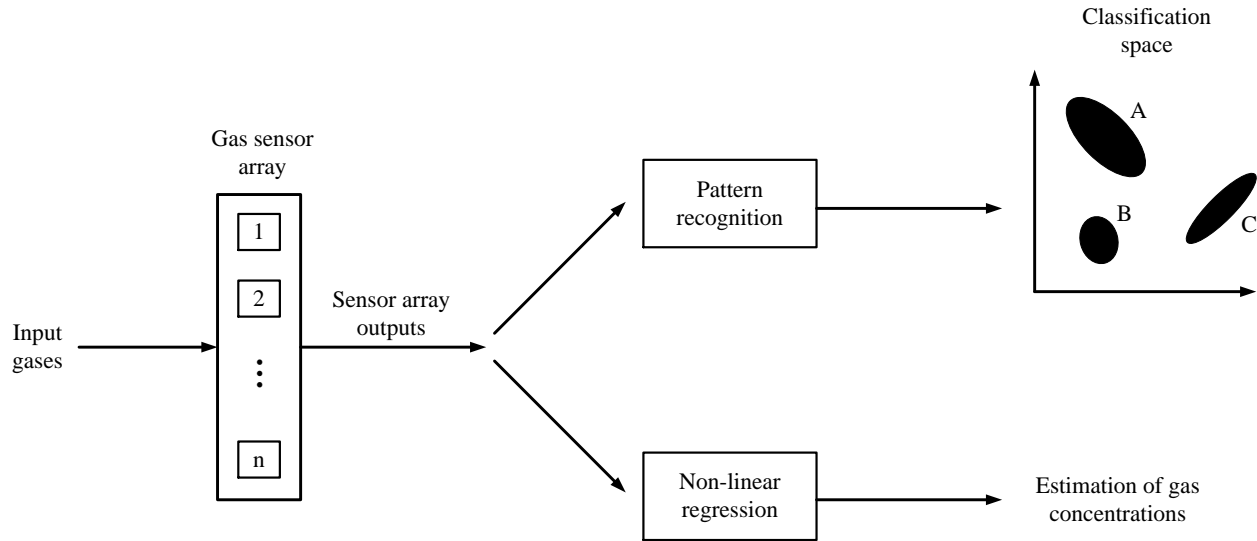


Figure 2. Machine learning in gas sensing scenario. The gas type classification is achieved by pattern recognition procedure, while the gas concentrations are estimated by non-linear regression technique.

2.2 DIELECTROPHORESIS

Dielectrophoresis (DEP), discovered by H. A. Pohl [29], refers to the motion of a dielectric particle caused by the interaction between a non-uniform electric field and the particle. The intuitive physics of DEP is illustrated in Figure 3. Once a dielectric particle in fluid is subjected to a non-uniform electric field, charges of opposite signs accumulate at either side of the particle. Because of the non-uniformity of the electric field, the electrical forces applying on each side cannot be balanced, resulting in the motion of the particle. Depending on the polarizability of the particle compared to that of the surrounding medium, the particle is either attracted to (positive DEP) or repelled from (negative DEP) the strong electric field region [31], which increases the flexibility in controllable assembly of nanostructures. While DEP was initially applied to

manipulate biological cells since its discovery [60, 61], researchers have also demonstrated it can assemble nanostructures efficiently.

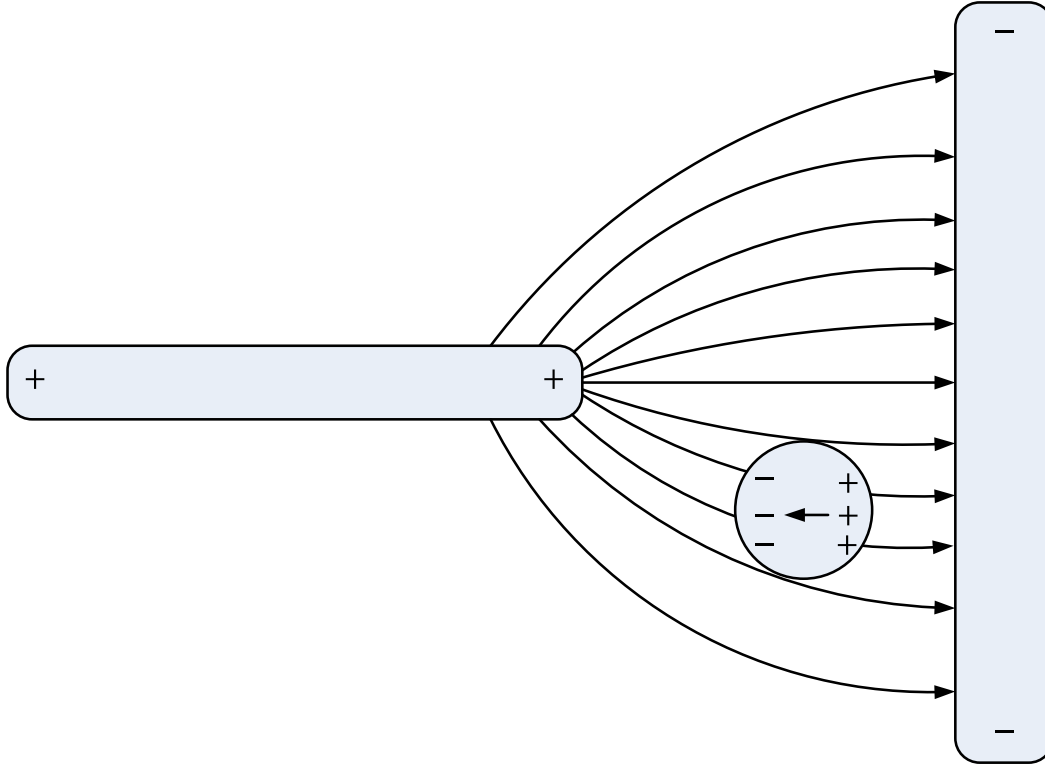


Figure 3. Schematic showing a dielectric particle translates in a non-uniform electric field.

There are three basic methods to characterize DEP force on a particle: Maxwell stress tensor method [62], energy method [29, 63-65], and effective dipole moment method [29-31]. In Maxwell stress tensor method, the DEP force is acquired by integrating the stress tensor over the surface enclosing the body of the particle. Concretely, the DEP force can be expressed by

$$\mathbf{F}_{\text{DEP}} = \oint (\mathbf{T} \cdot \mathbf{n}) dA, \quad (2.3)$$

in which \mathbf{T} is the stress tensor, \mathbf{n} is the unit vector normal to the surface, and A is the surface enclosing the particle. Maxwell stress tensor method is regarded as the most rigorous approach to calculate DEP force. However, because of the mathematical complexity, application of this

approach is limited to the case of spherical particle under a slightly non-uniform electric field [66, 67]. The complicated integration prevents us from efficiently computing the DEP forces on particles with other geometries such as nanowires and graphenes.

The energy method computes the energy of the particle inside the electric field with a volume integration, and determines the DEP force by characterizing the change in energy resulting from a small displacement. Mathematically, the time-averaged electrical energy in a volume V enclosing the particle is given by

$$\langle U \rangle = \frac{1}{4} \int \text{Re}(\mathbf{E} \cdot \tilde{\epsilon}_p^* \mathbf{E}^*) dV, \quad (2.4)$$

where \mathbf{E} is the local electric field, and the asterisk indicates complex conjugation. $\tilde{\epsilon}_p$ is complex permittivity of the nanostructure, which has a definition of $\tilde{\epsilon} = \epsilon - i \frac{\sigma}{\omega}$. ϵ and σ are the permittivity and electric conductivity of the material, and ω is the angular frequency of the electric field. The gradient of the energy tells the DEP force on the particle,

$$\langle \mathbf{F}_{\text{DEP}} \rangle = -\nabla \langle U \rangle. \quad (2.5)$$

This approach provides a good description for loss free dielectrics yet has a problem that energy conservation does not hold when there are dielectric losses associated with the particle or the medium.

The effective dipole moment method treats the polarized particle as an effective dipole and characterizes the interaction between the electric field and the dipole. This method is more preferred since it is natural in physics understanding and convenient in computational analysis. In an inhomogeneous electric field, the DEP force on an effective dipole is expressed as [29-31]

$$\mathbf{F}_{\text{DEP}} = \mathbf{p} \cdot \nabla \mathbf{E}, \quad (2.6)$$

where \mathbf{p} is the moment of the dipole. In an AC electric field, the time-averaged DEP force can be written in the form of complex expression for the dipole moment and the electric field,

$$\langle \mathbf{F}_{\text{DEP}} \rangle = \frac{1}{2} \text{Re}[\tilde{\mathbf{p}} \cdot \nabla \mathbf{E}^*]. \quad (2.7)$$

The dipole moment of the particle in AC electric field has the form

$$\tilde{\mathbf{p}} = V \tilde{\alpha} \mathbf{E} e^{j\omega t}, \quad (2.8)$$

where the effective polarizability $\tilde{\alpha}$ is frequency dependent and relates to the several parameters of the nanostructure and the medium as well as the orientation of the particle with respect to the electric field. Introducing Equation (2.8) to Equation (2.7) implies the common form of time-averaged DEP force,

$$\langle \mathbf{F}_{\text{DEP}} \rangle = \frac{1}{4} V \text{Re}[\tilde{\alpha}] \nabla |\mathbf{E}|^2. \quad (2.9)$$

During calculation, the nanowire is often treated as a prolate ellipsoidal particle. Consider a homogeneous, dielectric, ellipsoidal particle with half lengths of major axes a , b , and c , as shown in Figure 4. The effective polarizability $\tilde{\alpha}_n = 3\varepsilon_m \tilde{K}_n$ is different when the electric field is along each major axis n (where $n = a, b, c$) [30, 31]. ε_m is the permittivity of the surrounding medium, and the frequency dependent factor \tilde{K}_n is given by

$$\tilde{K}_n = \frac{\tilde{\varepsilon}_p - \tilde{\varepsilon}_m}{3[\tilde{\varepsilon}_m + (\tilde{\varepsilon}_p - \tilde{\varepsilon}_m)L_n]}, \quad (2.10)$$

where $\tilde{\varepsilon}_m$ is the complex permittivity of the medium, and L_n is the depolarization factor along the major axis n . For prolate spheroids, $a > b = c$, the depolarization factor L_a has the form

$$L_a = \frac{b^2}{2a^2e^3} \left[\ln \left(\frac{1+e}{1-e} \right) - 2e \right], \quad (2.11)$$

and $L_b = L_c = (1 - L_a)/2$, where $e = \sqrt{1 - b^2/a^2}$ is the eccentricity of the spheroid. Therefore, the DEP force can be calculated when the electric field is along each major axis. For example, the DEP force generated by the x component electric field is expressed by

$$\langle \mathbf{F}_{\text{DEP}x} \rangle = \pi abc \varepsilon_m \text{Re}[\tilde{K}_a] \nabla |\mathbf{E}_x|^2. \quad (2.12)$$

The non-uniform AC electric field also applies a DEP torque to align the dipole with the direction of the electric field,

$$\langle \mathbf{T}_{\text{DEP}} \rangle = \frac{1}{2} \text{Re}[\tilde{\mathbf{p}} \times \mathbf{E}^*], \quad (2.13)$$

which has three torque components along the major axes. Mathematically, the three torque components are

$$\langle T_{\text{DEP}x} \rangle = \frac{2}{3} \pi abc \varepsilon_m (L_c - L_b) E_y E_z \text{Re}[\tilde{K}_b \tilde{K}_c], \quad (2.14)$$

$$\langle T_{\text{DEP}y} \rangle = \frac{2}{3} \pi abc \varepsilon_m (L_a - L_c) E_z E_x \text{Re}[\tilde{K}_c \tilde{K}_a], \quad (2.15)$$

$$\langle T_{\text{DEP}z} \rangle = \frac{2}{3} \pi abc \varepsilon_m (L_b - L_a) E_x E_y \text{Re}[\tilde{K}_a \tilde{K}_b]. \quad (2.16)$$

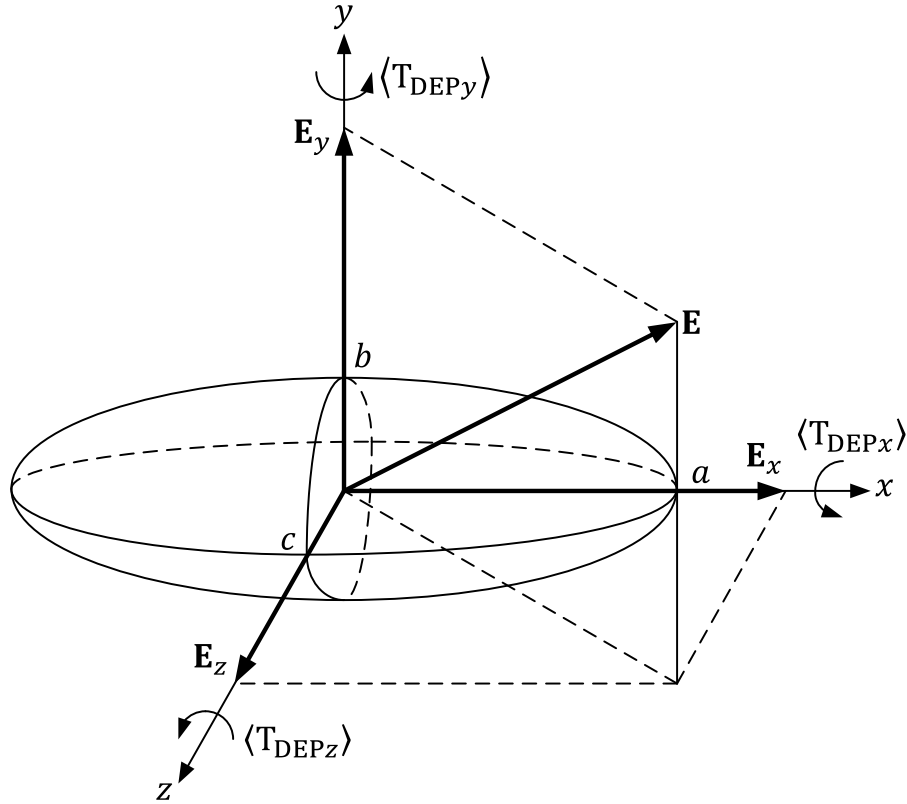


Figure 4. Schematic showing a homogeneous prolate ellipsoidal particle with semi-axes a , b , and c is subjected to an electric field \mathbf{E} .

The nanowire usually has a high aspect ratio ($a \gg b = c$), which can be characterized in the 2-D x - y plane, shown in Figure 5. The electric field could be parallel to or perpendicular to the long major “ a ” axis. The parallel depolarization factor $L_{\parallel} = L_a = 0$, while the perpendicular depolarization factor $L_{\perp} = L_b = \frac{1}{2}$. For a nanowire with length of l ($l = 2a$) and with radius of r ($r = b = c$), the DEP force generated by the parallel component electric field has the form

$$\langle \mathbf{F}_{\text{DEP}\parallel} \rangle = \frac{\pi r^2 l}{2} \varepsilon_m \text{Re}[\tilde{K}_{\parallel}] \nabla |\mathbf{E}_{\parallel}|^2, \quad (2.17)$$

where \tilde{K}_{\parallel} is the parallel frequency dependent factor which has similar definition as Equation (2.10). Similarly, if the nanowire or nanotube is perpendicular to the direction of the electric field, the DEP force is given by

$$\langle \mathbf{F}_{\text{DEP}\perp} \rangle = \frac{\pi r^2 l}{2} \varepsilon_m \text{Re}[\tilde{K}_{\perp}] \nabla |\mathbf{E}_{\perp}|^2. \quad (2.18)$$

Moreover, the non-uniform electric field applies a DEP torque to align the dipole with the direction of the electric field

$$\mathbf{T}_{\text{DEP}} = \frac{1}{3} \pi r^2 l \varepsilon_m (L_{\perp} - L_{\parallel}) \mathbf{E}_{\parallel} \mathbf{E}_{\perp} \text{Re}[\tilde{K}_{\parallel} \tilde{K}_{\perp}]. \quad (2.19)$$

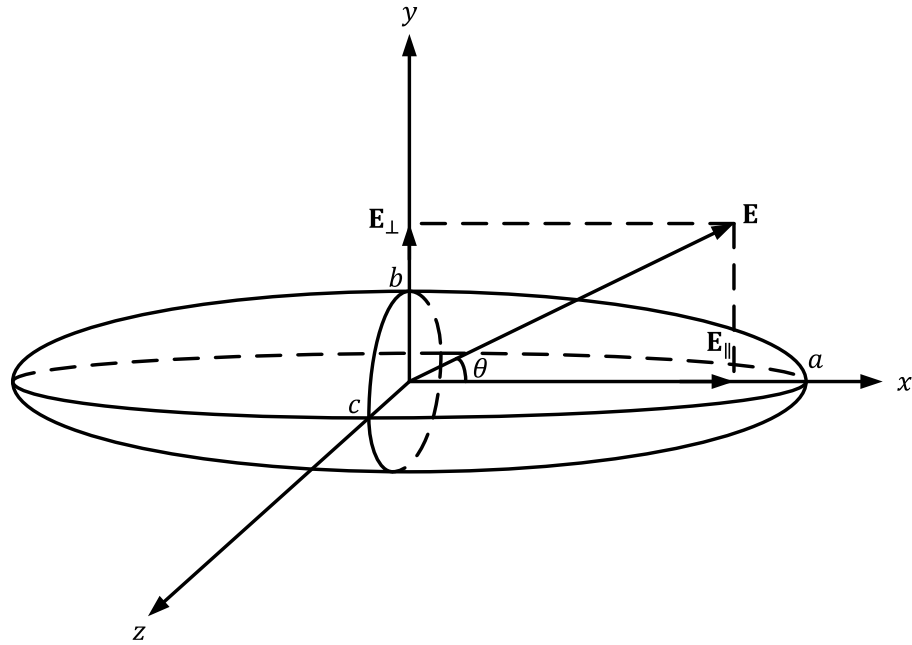


Figure 5. Schematic showing a homogeneous prolate ellipsoidal particle with semi-axes a , b , and c is subjected to an electric field \mathbf{E} in x - y plane.

The classical effective dipole moment method, which is under an assumption that the electric field around the nanowire is uniform, can only describe the DEP force when the electric field has specific orientations with respect to the nanowire. In real situations, the assumption is not appropriate and the general formula of DEP force on the nanowire with arbitrary orientation is indispensable. In this work, the optimization on the classical effective dipole moment method and quantitative description of the underlying physics of DEP assembly are the main contributions.

3.0 DEP ASSEMBLY OF SINGLE NANOWIRE IN 2-D SPACE

3.1 DEP FORCE AND DEP TORQUE ON NANOWIRE IN 2-D SPACE

3.1.1 Optimization on DEP force and DEP torque

Because of its axisymmetric property, single nanowire could be described in 2-D space. The classical formula described in Section 2.2 enables us to estimate the DEP force when the electric field is along or perpendicular to the nanowire. In most cases, however, the electric field could be neither along nor perpendicular to the long axis of the nanowire. Moreover, the classical DEP force and torque expressions are based on an assumption that the electric field in the vicinity of the nanowire is uniform, which is not true in real situations because the size of the nanowire is comparable to the gap of the electrodes and the non-uniformity of the electric field around the nanowire is unavoidable. Consequently, the model to estimate the DEP force and torque is more complicated and deserves further investigation.

For the sake of generality, assuming the nanowire has an angle of θ with the electric field, the electric field then can be orthogonally decomposed to the directions parallel to and perpendicular to the nanowire, shown in Figure 5. The DEP force relates to each component can be calculated using Equations (2.17) and (2.18). Mathematically, the DEP force produced by the parallel component of the electric field \mathbf{E}_{\parallel} can be written as

$$\langle \mathbf{F}_{\text{DEP}\parallel} \rangle = \frac{\pi r^2 l}{2} \varepsilon_m \text{Re}[\tilde{K}_{\parallel}] \nabla |\mathbf{E}_{\parallel}|^2 = \frac{\pi r^2 l}{2} \varepsilon_m \text{Re}[\tilde{K}_{\parallel}] \nabla |\mathbf{E} \cos \theta|^2. \quad (3.1)$$

Since the angle θ does not relate to the position vector, $\cos \theta$ is able to be taken outside the gradient operator, simplifying the above equation to

$$\langle \mathbf{F}_{\text{DEP}\parallel} \rangle = \frac{\pi r^2 l}{2} \varepsilon_m \cos^2 \theta \text{Re}[\tilde{K}_{\parallel}] \nabla |\mathbf{E}|^2. \quad (3.2)$$

Similarly, the DEP force corresponding to the perpendicular component of the electric field \mathbf{E}_{\perp} is given by

$$\langle \mathbf{F}_{\text{DEP}\perp} \rangle = \frac{\pi r^2 l}{2} \varepsilon_m \sin^2 \theta \text{Re}[\tilde{K}_{\perp}] \nabla |\mathbf{E}|^2. \quad (3.3)$$

The directions of $\langle \mathbf{F}_{\text{DEP}\parallel} \rangle$ and $\langle \mathbf{F}_{\text{DEP}\perp} \rangle$ are along the direction of $\nabla |\mathbf{E}|^2$. Thereby, the vector summation of $\langle \mathbf{F}_{\text{DEP}\parallel} \rangle$ and $\langle \mathbf{F}_{\text{DEP}\perp} \rangle$ gives the total DEP force on a nanowire

$$\langle \mathbf{F}_{\text{DEP}} \rangle = \frac{\pi r^2 l}{2} \varepsilon_m \left[\cos^2 \theta \text{Re}[\tilde{K}_{\parallel}] + \sin^2 \theta \text{Re}[\tilde{K}_{\perp}] \right] \nabla |\mathbf{E}|^2. \quad (3.4)$$

The underlying assumption of this calculation is the dimension of the nanowire is smaller than the non-uniformity of the electric field. In reality, the microelectrodes utilized to generate a non-uniform electric field have a very small gap compared to the length of the nanowire. Therefore, in the region close to the electrodes, the electric field across the nanowire is highly non-uniform, causing the above calculation inappropriate. To solve this problem, we use an approach similar to finite element method by dividing the whole nanowire into several small cylinders such that the electric field around each part can be considered as uniform, as shown in Figure 6. The time averaged DEP force and torque on each cylinder can be determined by Equations (3.4) and (2.16), respectively. The vector summations of these DEP forces and torques yield the total DEP force and DEP torque on the nanowire. Moreover, the DEP force on each cylinder generates an additional torque with respect to the center of the nanowire. Therefore, the total DEP force

determines the nanowire's translation, while the total DEP torque together with the additional torque caused by DEP forces account for the rotational motion.

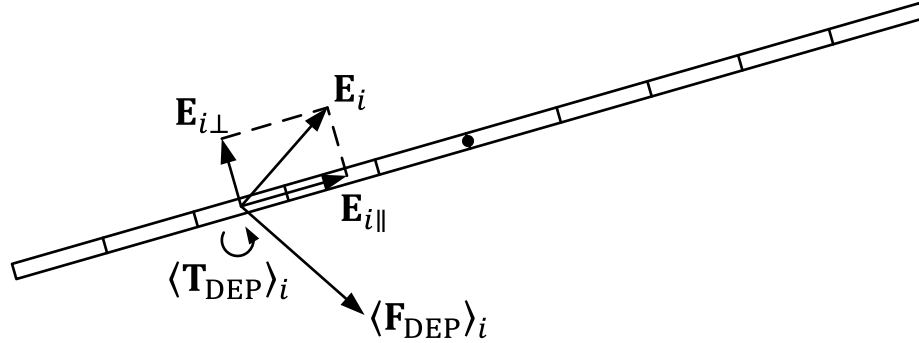


Figure 6. Even discretization of the nanowire to calculate the DEP force and DEP torque.

3.1.2 Frequency and conductivity dependence of DEP force

To study the feasibility of selective assembly of nanostructures by DEP, we calculated the DEP forces on ZnO nanowire (with radius of 30 nm and length of 10 μm). The permittivity of ZnO nanowire is about $2.5\epsilon_0$, where ϵ_0 is the vacuum permittivity. Isopropanol (IPA) is used as the suspending medium, which has a conductivity of 3.5×10^{-4} S/m and a permittivity of $30\epsilon_0$ at room temperature. By applying a 5 V excitation across a pair of sharp microelectrodes with narrow gaps (5 μm), a non-uniform electric field is simulated in Ansoft Maxwell software (Figure 7). In the region near the electrodes, the gradient of electric field square $\nabla|\mathbf{E}|^2$ is at the order of 10^{15} V^2/m^3 . For the specific nanowires we are considering, the DEP forces on nanowires with different conductivities over frequency range from 10 kHz to 10 GHz are calculated and plotted in Figure 8 (a). The inset figure is a zoomed-in view from 10 MHz to 10 GHz, which shows a crossover effect. At low frequencies, DEP force is positive and strong

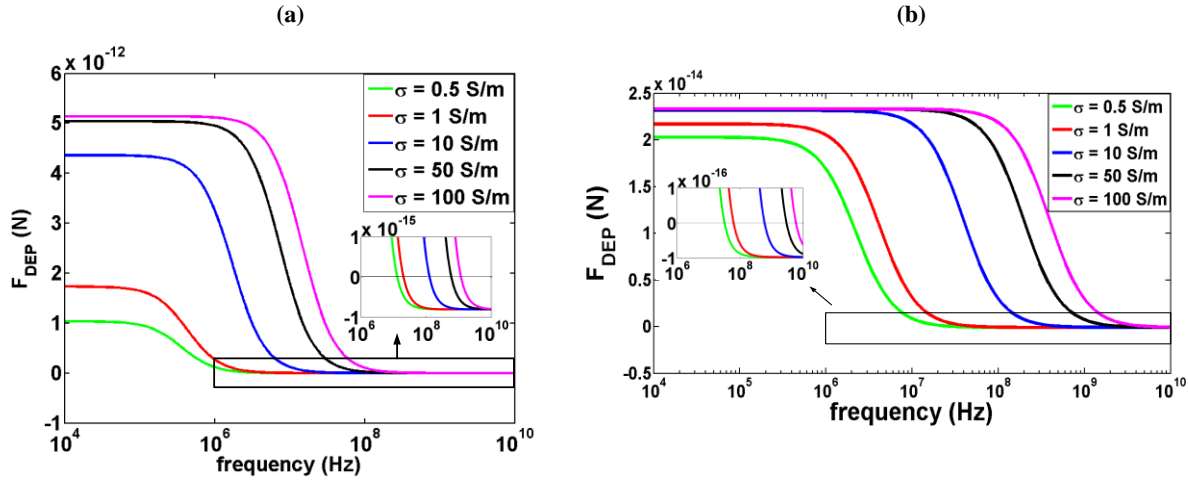


Figure 8. (a) The DEP force that a 10 μm -long, 60 nm in diameter nanowire receives under the electric field generated by rectangular electrodes versus frequency; (b) The DEP force that a 3 μm -long, 200 nm in diameter nanowire receives under the electric field generated by triangular electrodes versus frequency.

Since the DEP forces on nanowires depend on their conductivities and the frequency of the electric field, nanowires can be manipulated selectively. For example, when the frequency is set around 1MHz, nanowires with different conductivities are all attracted to the electrodes. As the frequency of the electric field is increased above 10MHz, nanowires with small conductivities are repelled, left with more conductive nanowires attached to the electrodes. Moreover, by starting from a high frequency, the turning frequency can be obtained by observing the deposition of nanowires onto the electrodes when gradually reducing the frequency. The conductivity of the deposited nanowire then can be estimated from this turning frequency.

3.2 INVESTIGATION ON TRAJECTORY AND ALIGNMENT OF NANOWIRE ASSEMBLED BY DEP

Besides the DEP force, DEP torque, and the torque generated by DEP forces, the motion of the nanowire assembled by DEP is also influenced by other effects including the hydrodynamic drag terms and Brownian motions. In the following part of this chapter, we construct a comprehensive model that takes all aspects into consideration and perform numerical simulations to predict the nanowire's trajectory and alignment. The experimental observations shown in the last subsection verify simulation results, and therefore consolidating the theoretical model.

3.2.1 Hydrodynamic drag force and drag torque

During the DEP assembly, the hydrodynamic drag force and drag torque hamper the motion of a nanowire or nanotube in fluid. For a prolate nanowire with length L moving in the nanofluid, the drag force relates to the velocity of the nanowire [69]. Mathematically, when the nanowire is moving parallel to its long axis, the drag force has the form

$$\mathbf{F}_{\text{DRAG}\parallel} = -\frac{2\pi\eta L}{\ln\left(\frac{L}{r}\right)-0.5}\mathbf{v}_{\parallel}, \quad (3.5)$$

where η is the viscosity of the fluid. When the nanowire is moving perpendicular to its long axis, the drag force is given by

$$\mathbf{F}_{\text{DRAG}\perp} = -\frac{4\pi\eta L}{\ln\left(\frac{L}{r}\right)+0.5}\mathbf{v}_{\perp}. \quad (3.6)$$

In reality, the velocity of the nanowire might be at any orientation with respect to the long axis. The velocity \mathbf{v} , however, could be decomposed orthogonally, shown in Figure 9 (a). Therefore, the drag force on the nanowire is expressed by

$$\mathbf{F}_{\text{DRAG}} = -\frac{2\pi\eta L}{\ln\left(\frac{L}{r}\right)-0.5}\mathbf{v}_{\parallel} - \frac{4\pi\eta L}{\ln\left(\frac{L}{r}\right)+0.5}\mathbf{v}_{\perp}. \quad (3.7)$$

To determine the drag torque on the nanowire, a handy approach is to evenly divide the nanowire to N segments of small cylinders [70], shown in Figure 9 (b). When the nanowire rotates with an angular velocity ω , each segment receives a drag force $\mathbf{F}_{\text{DRAG}i}$ relates to its velocity \mathbf{v}_i . The drag force on each cylinder thereby generates a torque with respect to the center of the nanowire. The total drag torque is estimated by summing up the torque comes from each cylinder,

$$T_{\text{DRAG}} = -2\sum_{i=1}^{\frac{N}{2}} \frac{\frac{4\pi\eta L}{N}}{\ln\left(\frac{L}{Nr}\right)+0.5} \beta \left[\left(i - \frac{1}{2}\right)\frac{L}{N}\right]^2 = -\frac{(N^3-N)\pi\eta L^3\omega}{3N^3\left[\ln\left(\frac{L}{Nr}\right)+0.5\right]}. \quad (3.8)$$

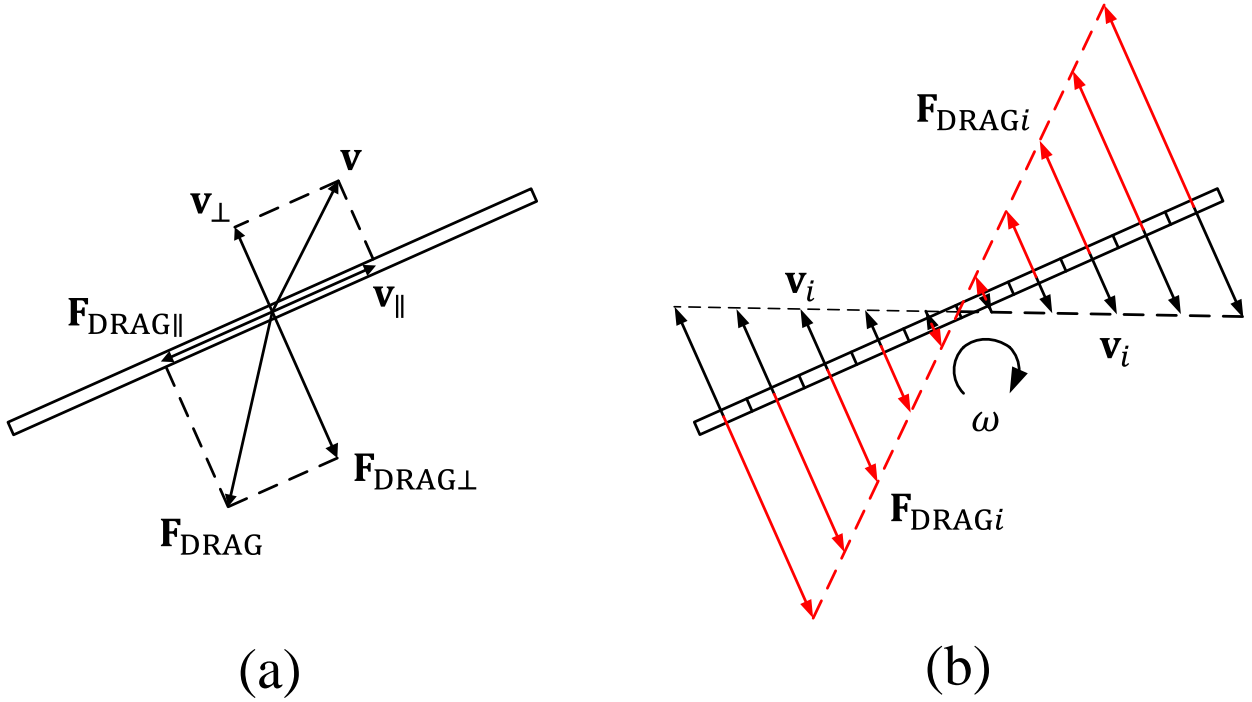


Figure 9. (a) Decomposition of the velocity to calculate the drag force. (b) Discretization of the nanowire to obtain the total drag torque.

3.2.2 Brownian motion

In nanofluids, small particles tend to move vigorously because of the Brownian motion. Due to the thermal energy of the system, particles in the solution experience a random force, causing them to move in a random manner [71]. Assuming the thermal energy kT is converted to the kinetic energy, the random force due to Brownian motion can be represented by a Gaussian random number with zero mean and a standard deviation of $f\sqrt{\frac{2kT}{m}}$, where k is Boltzmann constant, T is the temperature, m is the mass of the nanowire, and f is the friction factor of the nanowire in the fluids [31]. For a typical nanowire of length $10\mu\text{m}$ and diameter 30nm , the Brownian random force could be at the order of femto-newtons. The DEP force on the nanowire is not adequate to overcome the Brownian motion until it is close to the electrodes. In numerical simulation, Brownian motion can be characterized statistically in the form of displacements. According to Langevin equations, the displacements and the angle of the ellipsoid in the global coordinates in presence of external forces are described by a Hamiltonian H [72],

$$\partial_t x_i = -\Gamma_{ij}(\theta) \frac{\partial H}{\partial x_j} + \xi_i(t), \quad (3.9)$$

$$\partial_t \theta = -\Gamma_\theta \frac{\partial H}{\partial \theta} + \xi_\theta(t), \quad (3.10)$$

where $i = x, y$ for 2-D case, and Γ_{ij} and Γ_θ are the translation mobility tensor and angle mobility, respectively. ξ_i and ξ_θ are Gaussian noises with zero means. Since we only consider the displacements caused by Brownian motion, $\frac{\partial H}{\partial x_i} = 0$ and $\frac{\partial H}{\partial \theta} = 0$. The simplified Equation (3.10) implies the angular displacement satisfies Gaussian distribution. Equation (3.9) under $\frac{\partial H}{\partial x_i} = 0$ can be transformed into the local coordinates by introducing a rotational matrix \mathbf{R} ,

$$\partial_t \tilde{x}_i = \tilde{\xi}_i(t) = \mathbf{R}_{ij}[\theta(t)] \xi_j(t). \quad (3.11)$$

Hence, the displacements of the nanowire in the local coordinates also satisfies the Gaussian distribution (For detailed analysis on the statistical property of Brownian motion of an ellipsoidal particle in two-dimensional plane, please refer to Ref. [72]). Therefore as shown in Figure 10, in local coordinate, the translation displacements $\Delta\tilde{x}$, $\Delta\tilde{y}$, and the rotational displacement $\Delta\theta$ satisfy Gaussian distribution [72],

$$\Delta\tilde{x}\sim N(0,2D_{\tilde{x}}t), \quad \Delta\tilde{y}\sim N(0,2D_{\tilde{y}}t), \quad \Delta\theta\sim N(0,2D_{\theta}t), \quad (3.12)$$

where diffusion constants are defined as $D_i = kT/f_i$ (where $i = \tilde{x}, \tilde{y}, \theta$). The friction factors have the forms

$$f_{\tilde{x}} = \frac{2\pi\eta L}{\ln(\frac{L}{r})-0.5}, \quad f_{\tilde{y}} = \frac{4\pi\eta L}{\ln(\frac{L}{r})+0.5}, \quad f_{\theta} = \frac{(N^3-N)\pi\eta L^3}{3N^3[\ln(\frac{L}{Nr})+0.5]}. \quad (3.13)$$

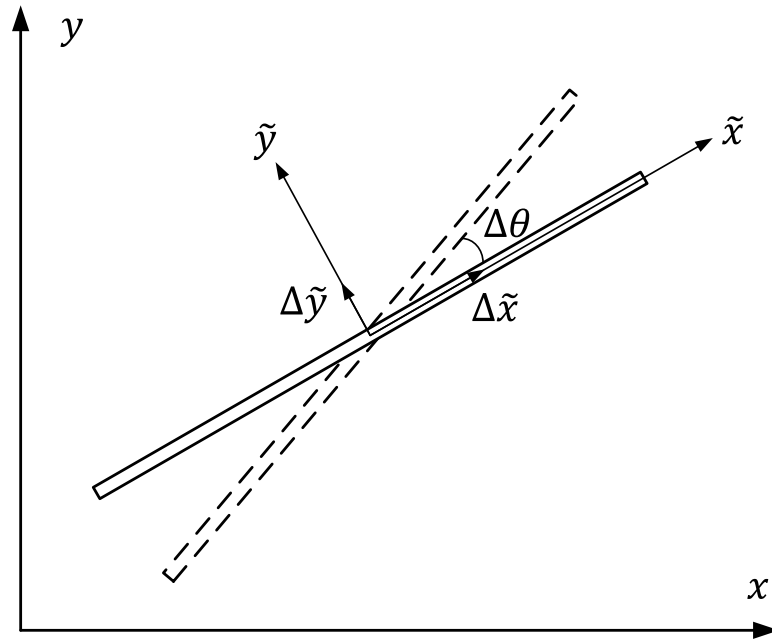


Figure 10. Representation of a nanowire in global $x - y$ coordinate and local $\tilde{x} - \tilde{y}$ coordinate.

3.2.3 Trajectory of DEP controlled nanowire

In 2-D situation, the motion of single nanowire in suspension obeys Newtonian dynamics. The DEP force and DEP torque, the torque generated by DEP force, drag force and drag torque, and Brownian motion account for its trajectory. The DEP force, DEP torque, and the torque generated by DEP force can be calculated based on the position and orientation of the nanowire inside the electric field (Figure 7). The state-space method is introduced to simulate the trajectory of the nanowire. We define system states $X = [x \ y \ \theta \ \dot{x} \ \dot{y} \ \dot{\theta}]'$ and system inputs $u = [F_{DEP_x} \ F_{DEP_y} \ F_{DRAG_x} \ F_{DRAG_y} \ T_{DEP} \ T_{DEP_force}]'$, where x , y and θ represent the coordinates of the center of the nanowire and its orientation, respectively, \dot{x} , \dot{y} and $\dot{\theta}$ are the nanowire's translational and rotational velocity, respectively, and T_{DEP_force} is the torque generated by DEP force. The system in each time step can be described by the state-space equation $\dot{X}(t) = AX(t) + Bu(t)$, which has an exact solution [73]

$$X(t) = e^{At}X(0) + \int_0^t e^{A(t-\tau)}Bu(\tau) d\tau. \quad (3.14)$$

The states at the end of each time step are determined by the states at the beginning of this step and the corresponding inputs. However, since DEP terms depend on the position of the nanowire and hydrodynamic effects are related to the velocity of the nanowire, the whole system is non-linear. Nonetheless, we update the inputs of the system at the beginning of each step and keep them to be constant during that step, such that the system can be linearized. The integral in Equation (3.14) can be numerically computed using Gauss-Legendre algorithm. Moreover, the displacements caused by Brownian motion are introduced according to Equation (3.12) at the end of each step. Additionally, because the inputs are considered to be constant during each step, the system states are not expected to change dramatically during each step. Thereby, a criterion

was set on the changes of the states to adaptively control the time step size, which improved the stability and precision of the numerical simulation.

In the electric field shown in Figure 7, assuming a 10- μm -long nanowire at (50 μm , 50 μm) is parallel to the electrodes with zero initial velocity; its trajectory is plotted in Figure 11 (a) after a numerical simulation. Because the polarizability of the nanowire is greater than that of the solvent at 1 MHz, the nanowire receives positive DEP force and is driven towards the electrodes along the direction of $\nabla|\mathbf{E}|^2$. The DEP torque dominates over the torque generated by DEP force, therefore aligning the nanowire with the direction of the electric field. Moreover, the nanowire will move faster gradually since the DEP force and torque become larger as it is closer to the electrodes. At 12.1 ms, the nanowire hits one electrode and cannot translate freely because of the strong Van der Waals force. Nevertheless, the nanowire is able to rotate around the attaching point. The DEP torque and the torque generated by DEP force drive the nanowire to bridge the electrodes ultimately.

The DEP assembly, however, cannot always perfectly align the nanowires. Figure 11 (b) shows the trajectory of a 5- μm -long nanowire starting from the same initial position. Similarly, the nanowire translates along the direction of $\nabla|\mathbf{E}|^2$, rotates to align with the direction of the electric field, and hits one electrode first. The DEP torque yet balances the torque generated by DEP force at certain orientation, causing the nanowire stay at that position.

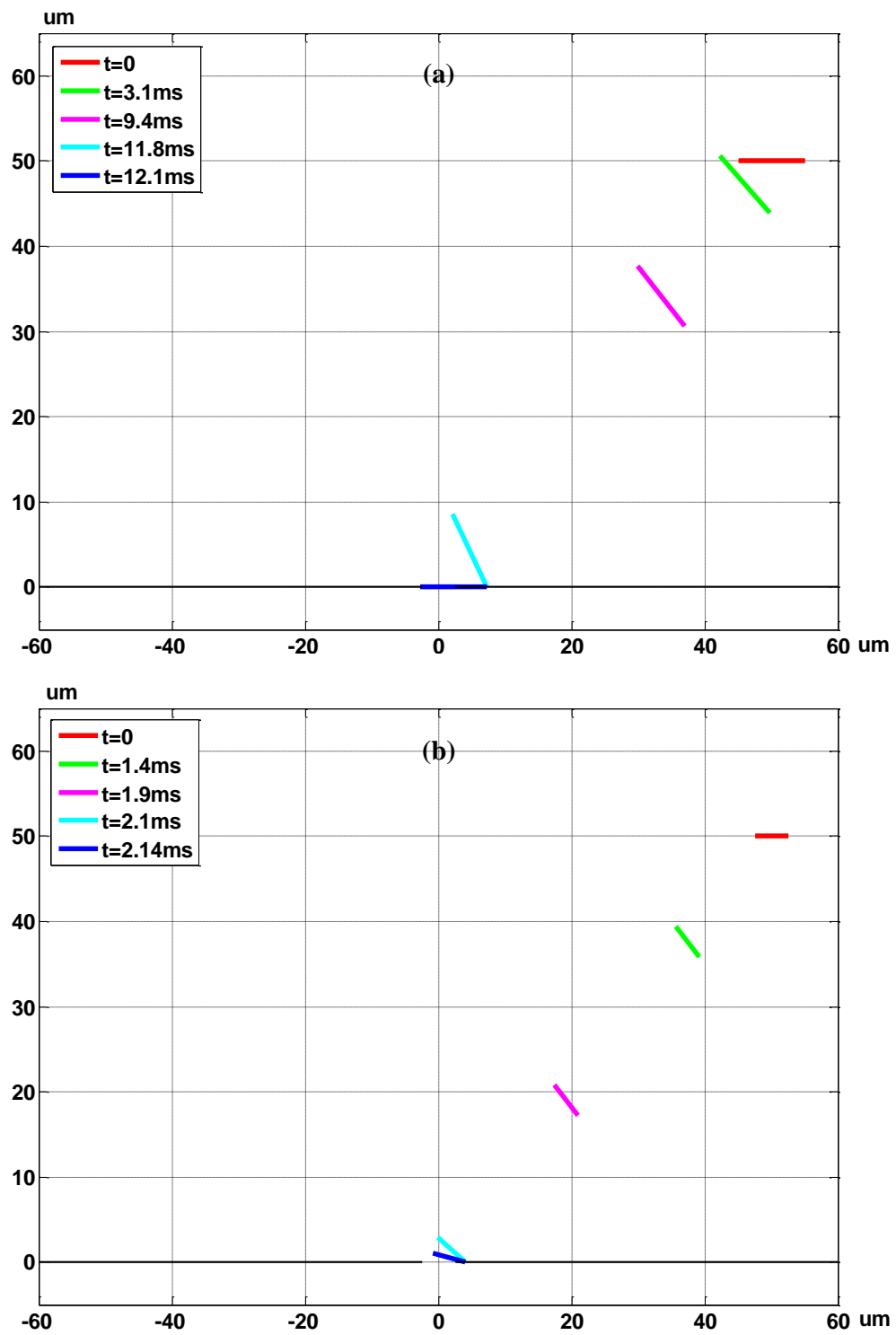


Figure 11. (a) Trajectory of a 10- μm -long nanowire. (b) Trajectory of a 5- μm -long nanowire.

3.2.4 Alignment of DEP controlled nanowire

To ensure the promising performance of nanowire-based devices, it is favorable that single nanowire can be well assembled across the electrodes. The simulation results in subsection 3.2.3, however, observed both well-bridged and misaligned nanowires. A detailed study on the alignment of the nanowires is substantial since those misaligned situations discourage researchers' enthusiasm in the further characterization of the devices.

To study the alignment of DEP assembled nanowire, a pair of microelectrodes with similar geometry to experimental electrodes are utilized. Once a nanowire contacts the electrode, shown in Figure 12, it cannot move freely because of the strong Van der Waals force. However, the nanowire can rotate around the contact point under the effect of the DEP torque, the torque generated by DEP forces, and the hydrodynamic drag torque. The motion of the nanowire in nanofluid is in the realm of very low Reynolds numbers. The hydrodynamic drag term dominates over the inertia term [74]. Hence, once subjected to an external torque, the nanowire reaches the terminal rotational velocity without apparent acceleration since the drag torque balances the external torque instantaneously. Similarly, in the absence of the external torque, the drag torque can stop the nanowire immediately. Therefore, the sum of the DEP torque and the torque generated by DEP forces determines the final orientation of the nanowire.

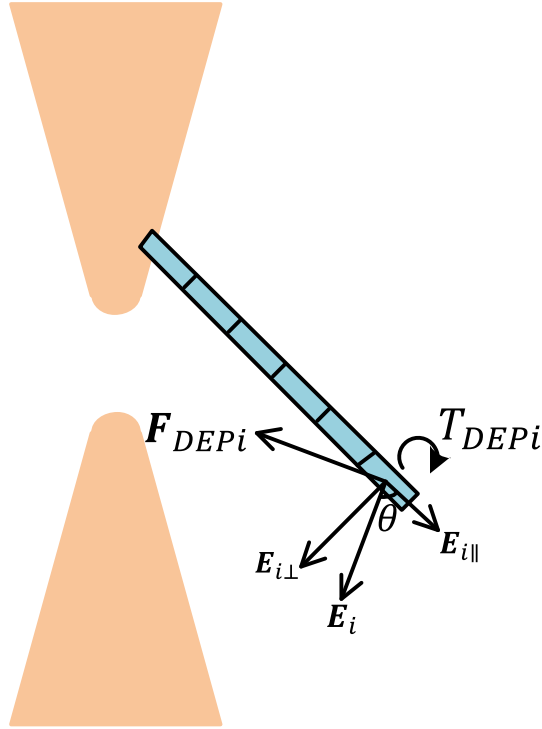


Figure 12. The nanowire contacts one electrode.

Microelectrodes with different gaps and with same geometry as experimental electrodes were constructed in Ansoft Maxwell software to simulate the distribution of the electric field, as a representative example of 4 μm gap electrodes shown in Figure 12. Single nanowire was initially assumed to be attached on an arbitrary position along the edge of one electrode. The DEP torque and the torque generated by DEP forces can be calculated for different orientations of the nanowire. The synthesized 1-D nanostructures like ZnO nanowires usually do not have very high aspect ratios. Therefore Equation (2.11) is utilized to calculate the parallel and perpendicular depolarization factor for each nanowire with given length and radius, which yields more accurate DEP torque and the torque generated by DEP forces. The ultimate orientation of the nanowire is where either the two torques balance or the electrode stop the rotation of the nanowire. Figure 14 and Figure 15 show the alignments of nanowires with different lengths and with a conductivity of 10^4 S/m attach on several locations on 1 μm gap and 4 μm gap electrodes,

respectively. The long nanowires that attach close to the center of electrodes can bridge the electrodes successfully. Once the nanowires attach far from the center, they cannot bridge the electrodes yet align along the edge of the electrode. If the contact positions continue to move away from the center of the electrodes, nanowires tend to stay at orientations with certain angles with respect to the electrodes. The angles increase as the attach points farther from the center of the electrodes. To better illustrate the alignments, electric field direction (black arrows) and the direction of the gradient form $\nabla|\mathbf{E}|^2$ (green arrows) around contact positions were incorporated with the result in Figure 14 (a), shown in Figure 16. The nanowire tends to align with the direction of gradient of electric field when it is close to the center of electrodes, whereas it is more likely to align with the direction of electric field as it attaches farther from the center. This observation implies the DEP torque dominates over the torque generated by DEP forces when the nanowire is far from the center. Oppositely, the torque generated by DEP forces is much stronger for the nanowire attaches close to the center.

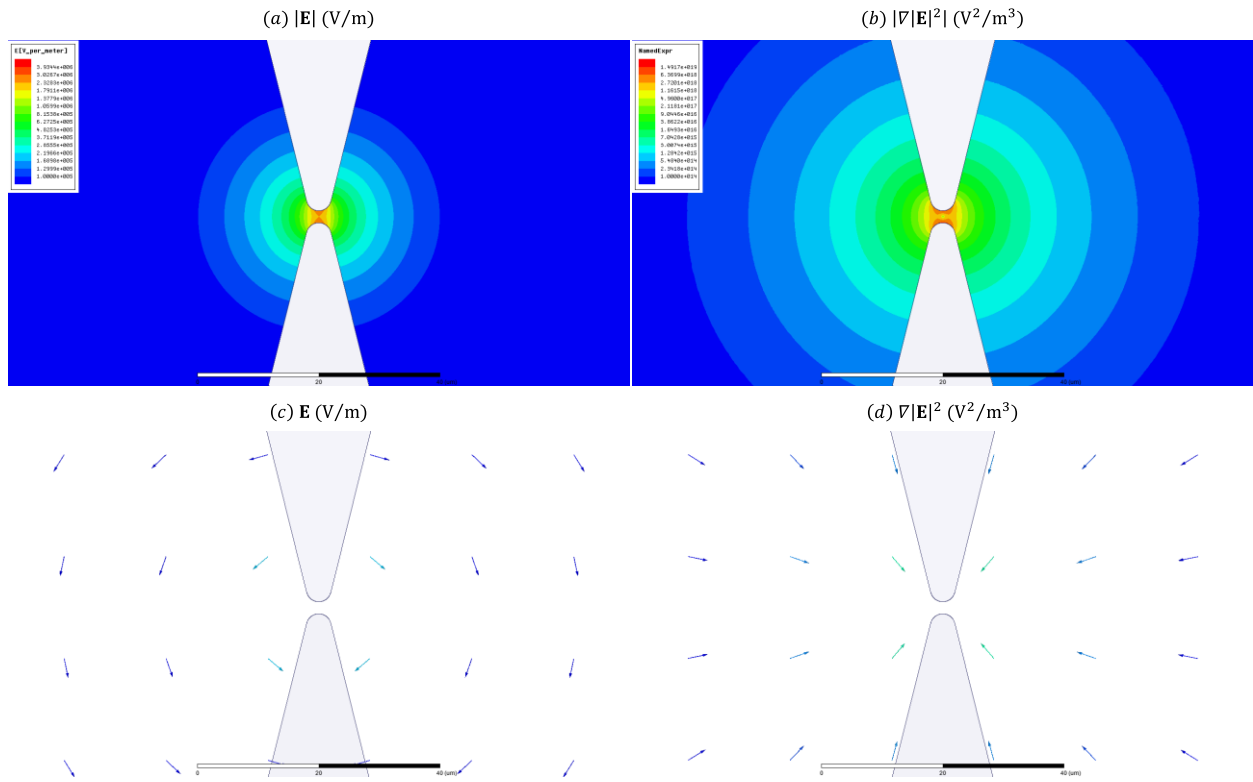


Figure 13. Electric field distribution generated by a pair of triangular electrodes with 4 μm gap. (a) The magnitude of the electric field E . (b) The magnitude of the gradient form $\nabla|E|^2$. (c) The vector plot of the electric field E . (d) The vector plot of the gradient form $\nabla|E|^2$.

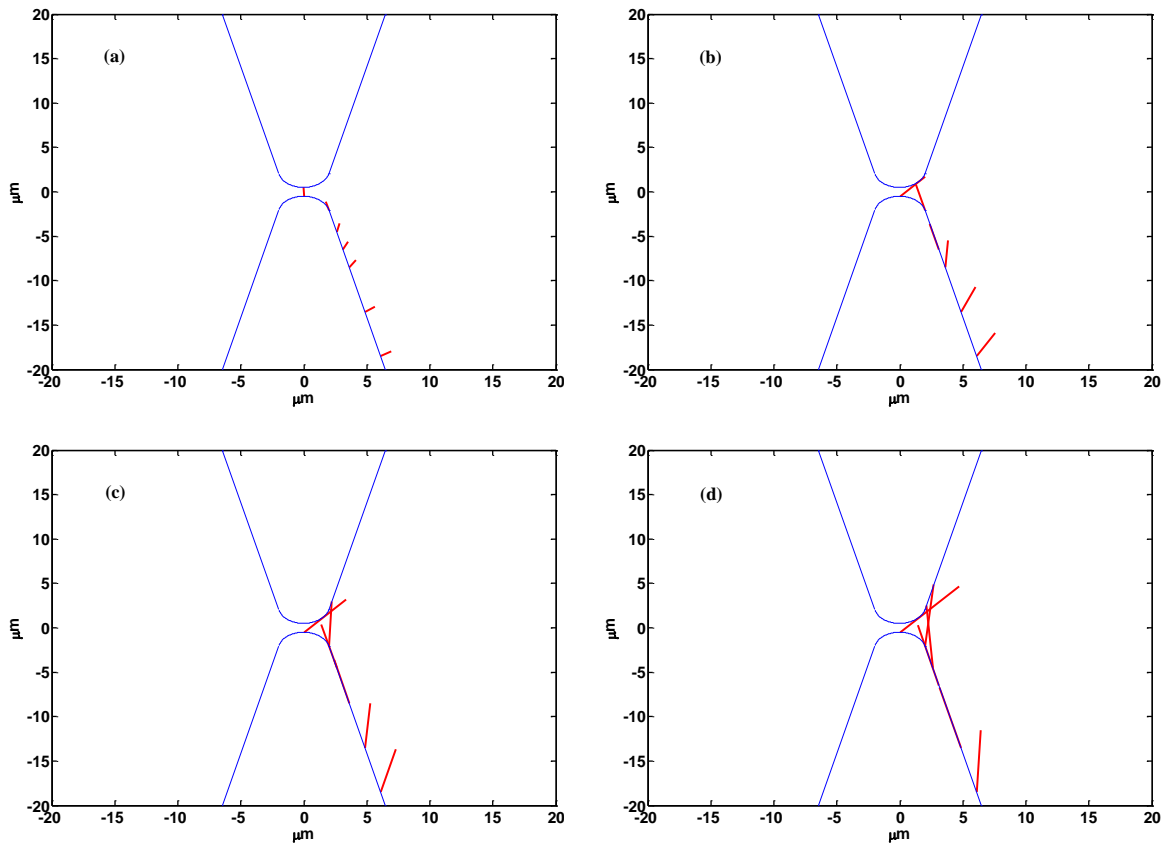


Figure 14. Alignments of nanowires with different lengths onto 1 μm gap electrodes. (a) 1- μm -long nanowire. (b) 3- μm -long nanowire. (c) 5- μm -long nanowire. (d) 7- μm -long nanowire.

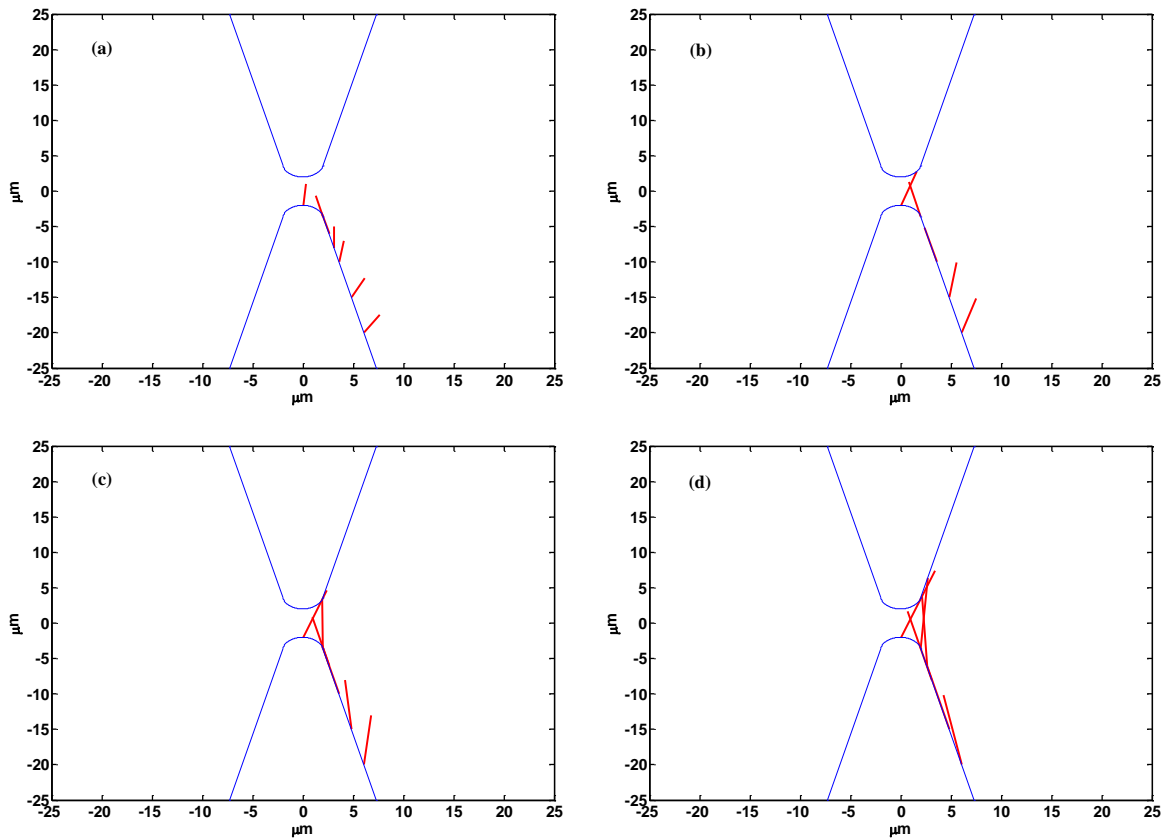


Figure 15. Alignments of nanowires with different lengths onto 4 μm gap electrodes. (a) 3- μm -long nanowire. (b) 5- μm -long nanowire. (c) 7- μm -long nanowire. (d) 10- μm -long nanowire.

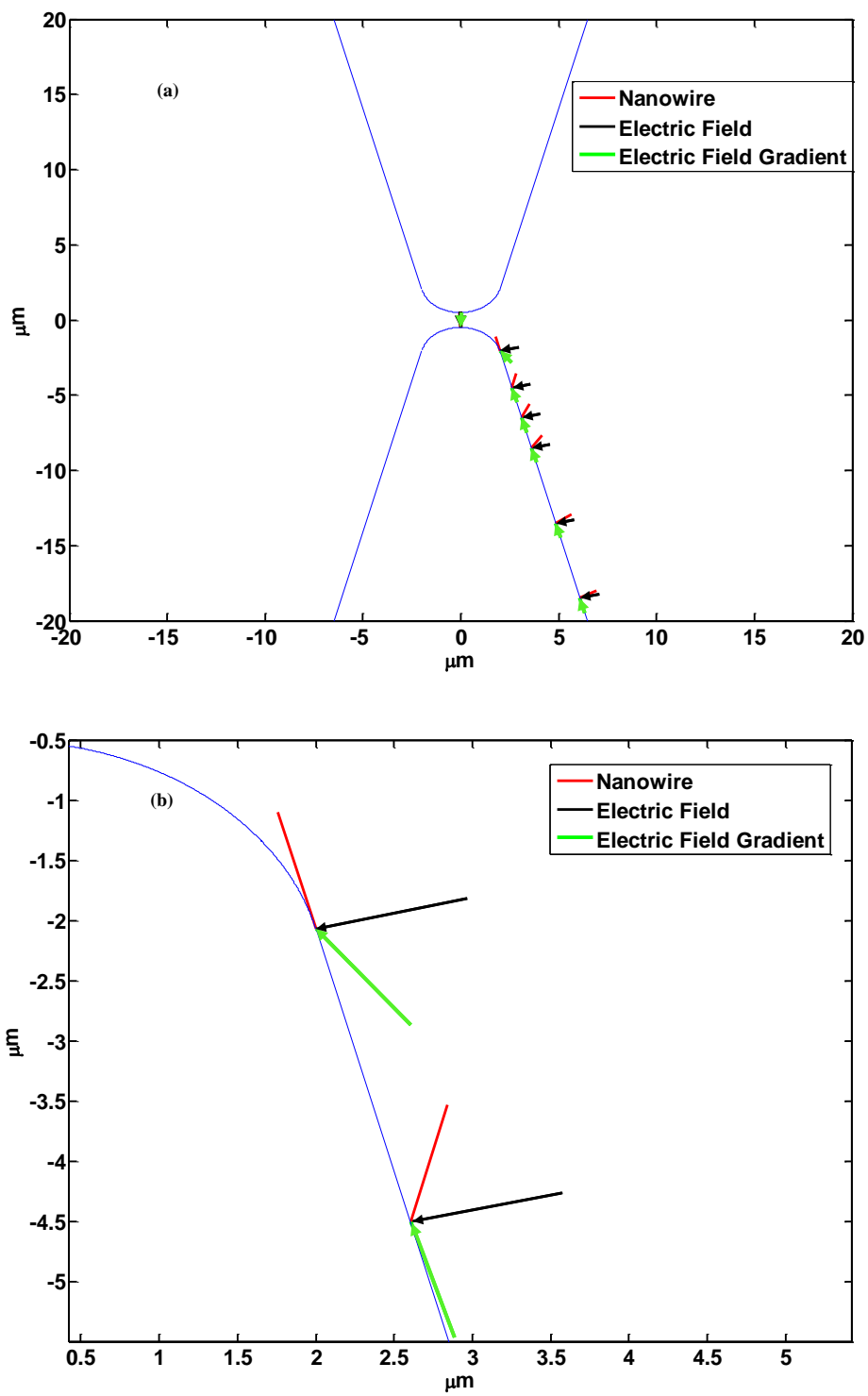


Figure 16. (a) Comparison of nanowires orientation with electric field and gradient of electric field directions at different positions. (b) A zoomed-in view of two nanowires that closet to the end of the electrodes.

The presented simulation results indicate the gap of the electrodes, the length of the nanowire, and the initial contact position on the electrode affect the alignment of single nanowire attaching on the electrode. The gap size of the electrodes affects the electric field distribution for a specified voltage excitation. Since the DEP calculation is based on a finite element like method, the length of the nanowire and its contact position on the electrode determine the electric field values utilized to calculate the DEP torque and the torque generated by DEP forces, which ultimately influences the orientation of the nanowire. Moreover, the gap size, the length of the nanowire, and the contact position determine whether the nanowire has the ability to bridge the electrodes. The nanowire which attaches close to the center of electrodes and whose length is larger than the gap size usually is able to bridge the electrodes. The short nanowire or the nanowire that attaches far from the center of electrodes cannot bridge the electrodes and stays at an orientation that close to either the direction of the electric field or the direction of the gradient of the electric field or in between. In the middle of the gap, the direction of the electric field and the direction of the gradient of the electric field are aligned to the same direction, from one electrode pointing to another one, thus the nanowire turns to bridge the gap and align at the center (Fig. 16a).

The conductivity of nanowire, the frequency and amplitude of excitation voltage are supposed to affect the DEP torque and the torque generated by DEP forces. However, the simulation demonstrated these parameters have no influences on the final alignment of the nanowire. Therefore, the alignment of DEP force assembled nanowire is only related to the length of the nanowire, the gap of the electrodes, and the initial contact position of the nanowire on the electrodes.

3.2.5 Experimental validation

To validate the simulation results on the nanowire's trajectory and alignment, a series of experiments were implemented to assemble ZnO nanowires and CNTs onto microelectrodes using DEP. The fabrication of the microelectrodes involves a series of standard MEMS techniques including optical lithography, e-beam evaporation, and lift off process, as shown in Figure 17. In our photo mask, the electrodes are dark fields while the electrode gaps are clear. The clean substrate was spin-coated with a 1.4 μm thick photoresist (AZ5214) layer and then patterned under a SUSS-MJB3 mask aligner. A subsequent reverse bake process formed crosslinks in exposed areas (electrode gaps), which cannot be dissolved in the developer. A flood exposure without the mask made the electrode regions soluble in the developer. After development, a titanium (5 nm)/gold (30 nm) layer was deposited onto the sample using an e-beam evaporator. The following lift off process in acetone was able to wash off the metal layer over the electrode gap regions, which achieves the electrodes we needed. Figure 18 is an atomic force microscopy (AFM) image of a pair of electrodes with a gap less than 1 μm .

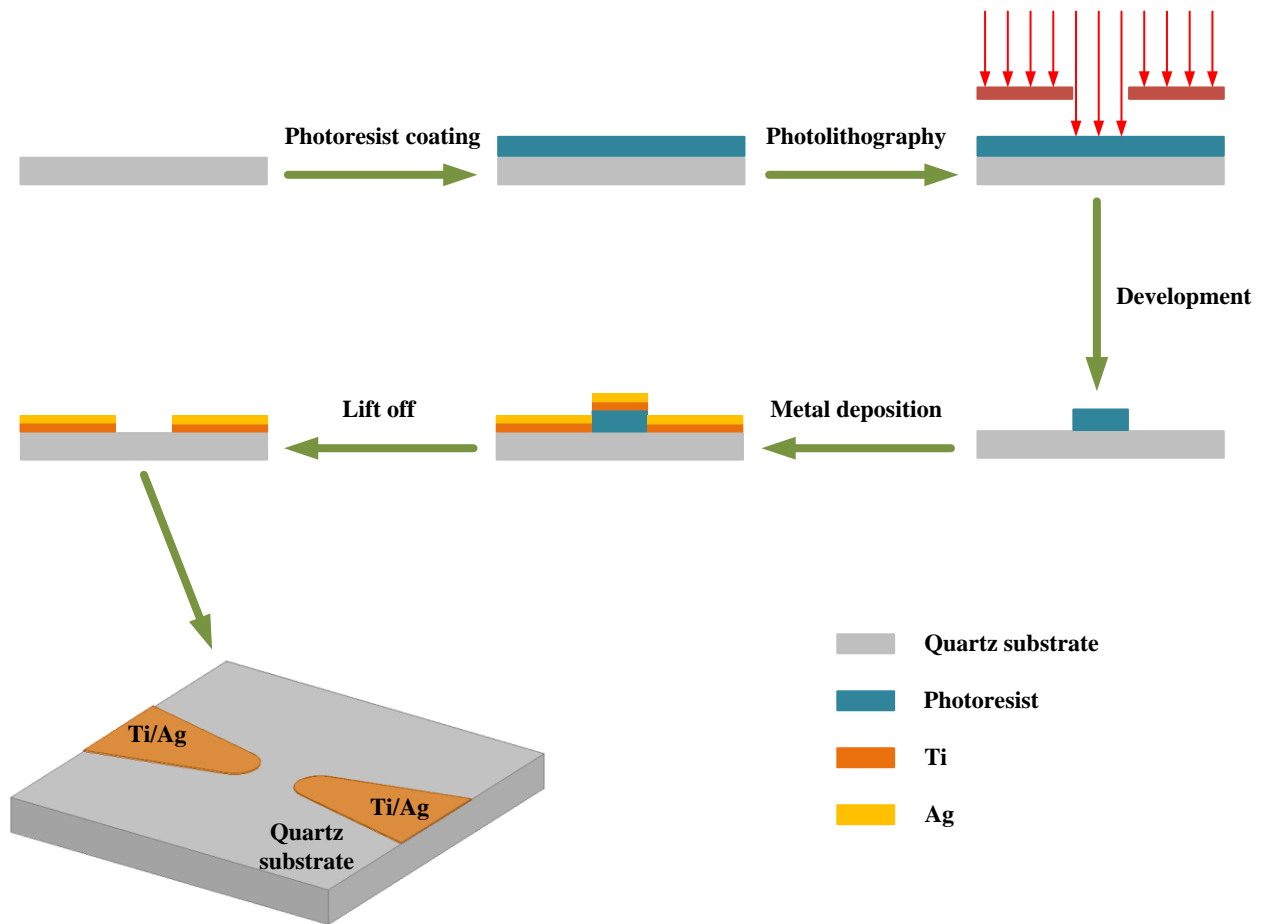


Figure 17. Fabrication process of microelectrodes.

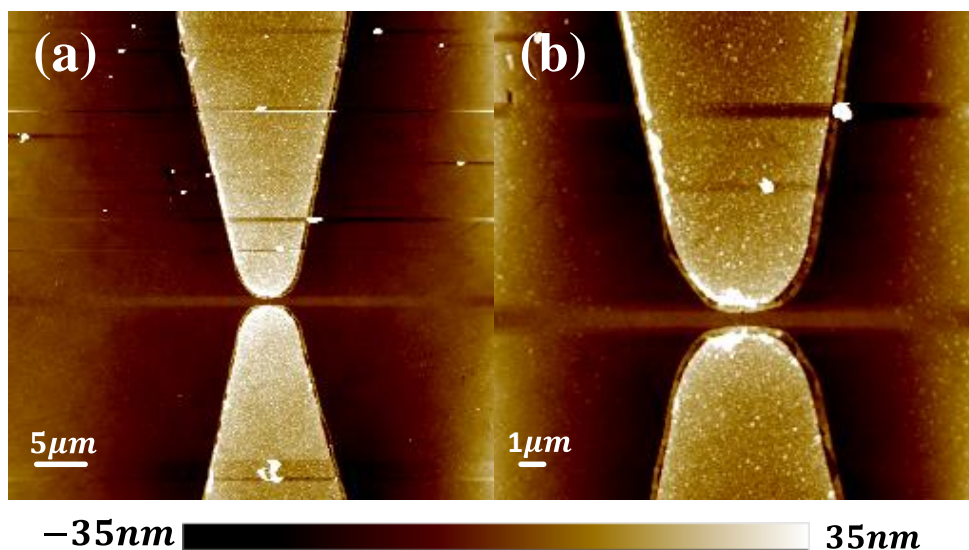


Figure 18. AFM image of a pair of electrodes with a gap smaller than 1 μm . Right figure is a zoomed-in view of left one.

The ZnO nanowires were synthesized by a solution-based approach. Aqueous solution of zinc nitrate hexahydrate and equimolar hexamethylenetetramine reacts in an oven for about 4 hours under a 95 $^{\circ}\text{C}$ atmosphere. The average length and diameter of the nanowires are 3 μm and 200 nm, respectively, as a representative SEM image shown in Figure 19. The nanowires were dispersed in IPA and sonicated for 10 min. During the experiment, a 15 μL droplet of nanowire dispersion was delivered across the electrodes through a pipette. The electrodes were then excited by a 1 MHz, 5 V voltage signal from the function generator. After 1 min, the sample was rinsed by deionized water and dried thoroughly. Then the chip was checked using AFM, shown in Figure 20. Since the gap of the electrodes is a bit large, the nanowires cannot successfully bridge the electrodes. Many nanowires are attached to one electrode and align at certain orientations. Double-walled CNTs purchased from Sigma-Aldrich were dispersed in N,N-Dimethylformamide (DMF) and assembled under same conditions. The AFM scanned images indicated both misaligned and well-bridged CNTs, as shown in Figure 21. Since both the

simulation and experimental results observed well-bridged and misaligned nanowires or nanotubes assembled close to the center of electrodes, it consolidated our model to characterize the trajectory of single nanowire or nanotube.

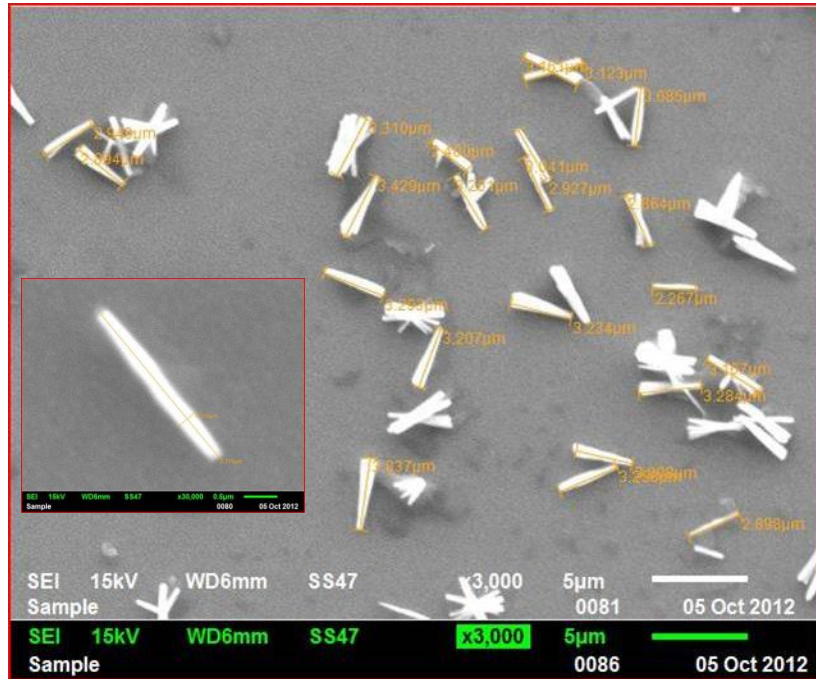


Figure 19. SEM image of synthesized ZnO nanowires before suspension. Scale bar is 5 μm for figure, and 0.5 μm for inset.

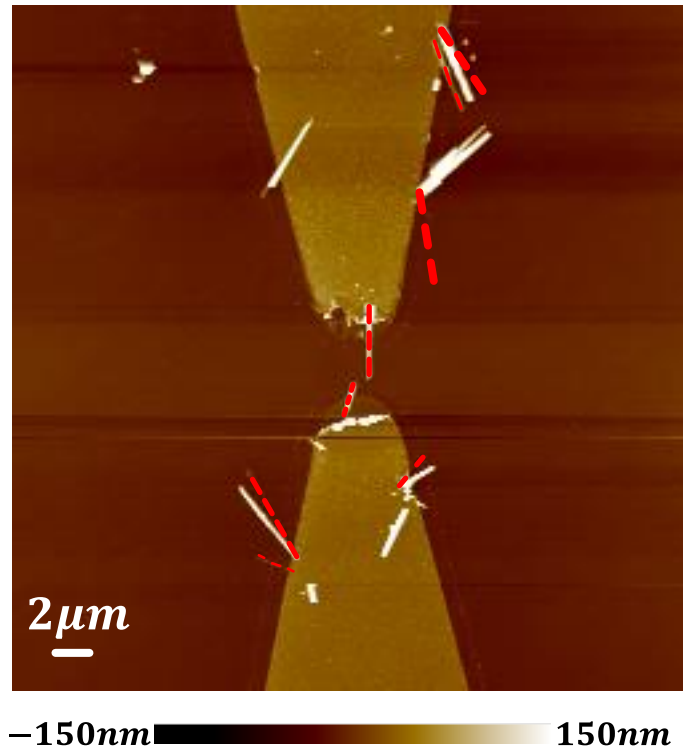


Figure 20. AFM images of electrodes with ZnO nanowires assembled (Dashed red lines indicate predicted alignments of ZnO nanowires at the corresponding positions).

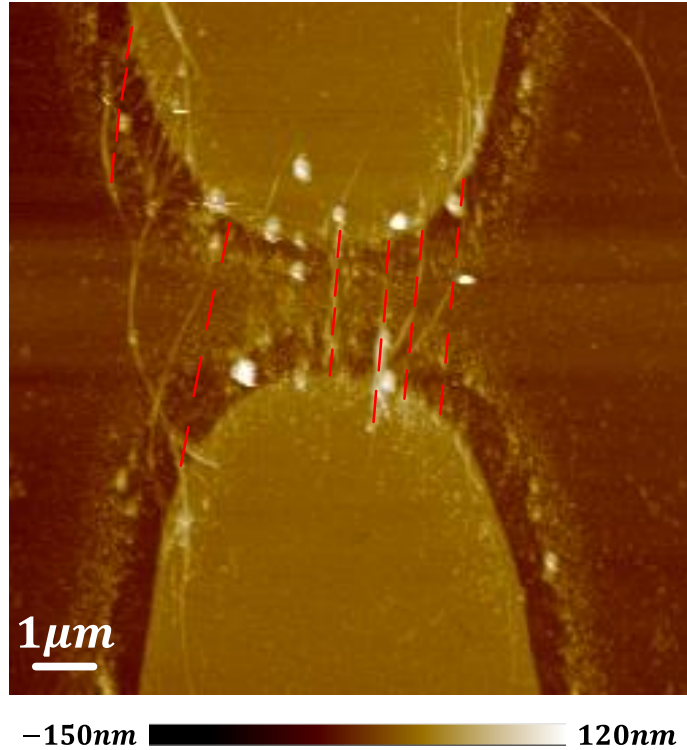


Figure 21. AFM images of electrodes with CNTs assembled (Dashed red lines indicate predicted alignments of CNTs at the corresponding positions).

To further validate the conclusions from the simulation results, the simulation predicted orientations are included in Figure 20 and Figure 21 to compare with the experimental results. The white lines are the AFM scanned ZnO nanowires of CNTs attaching on the electrodes after standard DEP assembly. The red dashed lines are the simulation predicted orientations of nanowires or nanotubes at those corresponding positions. The two sets of lines almost coincide everywhere with slight orientation differences at some positions. The coincidence, therefore, provides evidence that the proposed model to predict the alignment of nanowires or nanotubes is appropriate. The successful prediction attributes to the more accurate calculation of DEP torque and the original contribution on characterization of the additional torque generated by DEP forces. The slight differences, is presumably because of the additional friction force when the

nanowire or nanotube was rotating around the attach point. In addition, some nanowires or nanotubes might come from the top of the electrodes, which is beyond the current 2-D simulation scope. Nevertheless, this comparison essentially consolidated the feasibility of using proposed simulation method to predict the alignment of nanowire. A more complicated modeling in 3-D space is supposed to provide more accurate description on the motion of individual nanowire. There exists one nanowire assembled in an orientation that is significantly different from the prediction. The orientation of this nanowire might have been changed during removing the liquid when a strong surface tension applies to the nanowire while the Van der Waals force is not strong enough to hold it in position. We do not observe this phenomenon during assembling CNTs, which should have relatively strong Van der Waals force because of their small dimension.

4.0 DEP ASSEMBLY OF SINGLE NANOWIRE IN 3-D SPACE

Although the alignments of most nanowires could be well predicted through the 2-D modeling discussed in Chapter 3, there still exists some mismatch between the simulation predictions and experimental observations. The modeling on individual nanowire in 3-D space can describe the real situation during a standard DEP assembly, and therefore is supposed to provide more accurate prediction on the final alignment of the nanowire. In this chapter, a more complicated model including the characterization of DEP effect and hydrodynamic drag terms, and the Euler parameters machinery that used to describe the nanowire's motion in 3-D space is illustrated in details. The simulation study base on this 3-D modeling provides us not only a better understanding on the underlying physics but also practical guidance of nanowire assembly by DEP.

4.1 3-D MODELING ON NANOWIRE

4.1.1 DEP force and DEP torque

Similar to the analysis on 2-D modeling in Section 3.1, the whole nanowire is also divided into several cylinders such that the electric field around each segment can be treated as uniform. Each segment is modeled as an ellipsoid, such that classical formulas can be used to calculate the DEP

force and DEP torque, as shown in Figure 22. Both the DEP force and DEP torque on the i th segment have three base components, respectively,

$$\langle \mathbf{F}_{\text{DEP}x} \rangle_i = \frac{1}{2} \pi r^2 l \varepsilon_m \text{Re}[\tilde{K}_a] \nabla |\mathbf{E}_{ix}|^2, \quad (4.1)$$

$$\langle \mathbf{F}_{\text{DEP}y} \rangle_i = \frac{1}{2} \pi r^2 l \varepsilon_m \text{Re}[\tilde{K}_b] \nabla |\mathbf{E}_{iy}|^2, \quad (4.2)$$

$$\langle \mathbf{F}_{\text{DEP}z} \rangle_i = \frac{1}{2} \pi r^2 l \varepsilon_m \text{Re}[\tilde{K}_c] \nabla |\mathbf{E}_{iz}|^2, \quad (4.3)$$

$$\langle T_{\text{DEP}x} \rangle_i = \frac{1}{3} \pi r^2 l \varepsilon_m (L_c - L_b) E_{iy} E_{iz} \text{Re}[\tilde{K}_b \tilde{K}_c], \quad (4.4)$$

$$\langle T_{\text{DEP}y} \rangle_i = \frac{1}{3} \pi r^2 l \varepsilon_m (L_a - L_c) E_{iz} E_{ix} \text{Re}[\tilde{K}_c \tilde{K}_a], \quad (4.5)$$

$$\langle T_{\text{DEP}z} \rangle_i = \frac{1}{3} \pi r^2 l \varepsilon_m (L_b - L_a) E_{ix} E_{iy} \text{Re}[\tilde{K}_a \tilde{K}_b]. \quad (4.6)$$

Introducing the three angles $\alpha_i, \beta_i, \gamma_i$ that the electric field \mathbf{E}_i with x, y, z axes, the DEP force on the i th segment eventually is converted to the form

$$\langle \mathbf{F}_{\text{DEP}} \rangle_i = \frac{1}{2} \pi r^2 l \varepsilon_m \{ \text{Re}[\tilde{K}_a] \cos^2 \alpha_i + \text{Re}[\tilde{K}_b] \cos^2 \beta_i + \text{Re}[\tilde{K}_c] \cos^2 \gamma_i \} \nabla |\mathbf{E}_i|^2. \quad (4.7)$$

The vector summation of $\langle \mathbf{F}_{\text{DEP}} \rangle_i$ ($i = 1, 2, \dots, N$) yields the total DEP force on the whole nanowire, which accounts for the translational motion of the nanowire. Moreover, $\langle \mathbf{F}_{\text{DEP}} \rangle_i$ generates a torque with respect to the center of the nanowire. This torque does not cause the nanowire to spin around the major a axis. The sum of these torques gives the total torque generated by DEP forces. Since $b = c = r$ indicates $L_b = L_c$, the x component of DEP torque described in Equation (4.4) vanishes, which implies there is no spin rotation during the motion of the nanowire. As we sum up the $\langle T_{\text{DEP}y} \rangle_i$ and $\langle T_{\text{DEP}z} \rangle_i$ respectively and decompose the total torque generated by DEP force onto y and z axes, the separate rotations along y and z axes can be characterized.

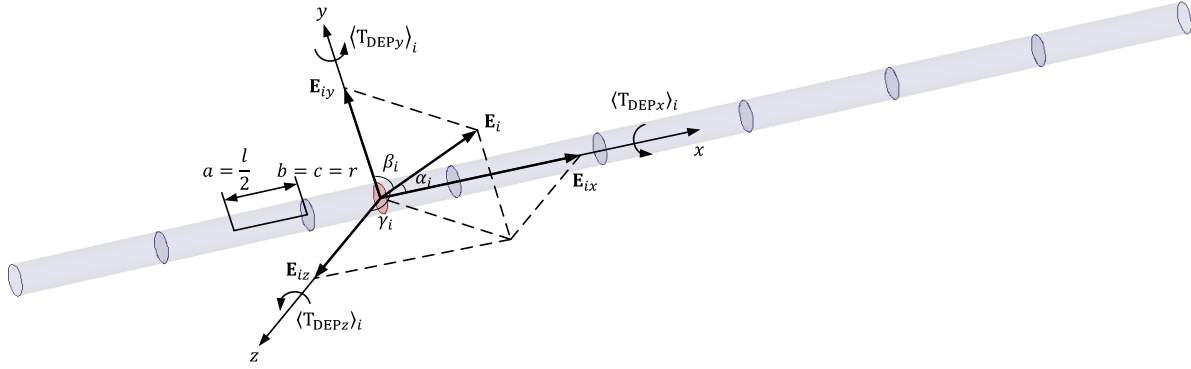


Figure 22. Discretization of the nanowire in 3-D space to characterize the DEP force, DEP torque and the torque generated by DEP forces.

4.1.2 Hydrodynamic drag force and drag torque

The motion of a nanowire in 3-D space is affected by the drag force and drag torque. The analysis on drag force is similar to the 2-D model in subsection 3.2.1 with a difference on the influence coming from additional perpendicular velocity. As shown in Figure 23, the velocity of the whole nanowire \mathbf{v} is decomposed into three components along x , y , and z axes. Each component results in a corresponding drag force.

$$\mathbf{F}_{\text{DRAG}x} = -\frac{2\pi\eta L}{\ln\left(\frac{L}{r}\right)-0.5} \mathbf{v}_x, \quad (4.8)$$

$$\mathbf{F}_{\text{DRAG}y} = -\frac{4\pi\eta L}{\ln\left(\frac{L}{r}\right)+0.5} \mathbf{v}_y, \quad (4.9)$$

$$\mathbf{F}_{\text{DRAG}z} = -\frac{4\pi\eta L}{\ln\left(\frac{L}{r}\right)+0.5} \mathbf{v}_z. \quad (4.10)$$

The composite of the three drag forces is the total drag force on the nanowire,

$$\mathbf{F}_{\text{DRAG}} = -\frac{2\pi\eta L}{\ln(\frac{L}{r})-0.5} \mathbf{v}_x - \frac{4\pi\eta L}{\ln(\frac{L}{r})+0.5} \mathbf{v}_y - \frac{4\pi\eta L}{\ln(\frac{L}{r})+0.5} \mathbf{v}_z. \quad (4.11)$$

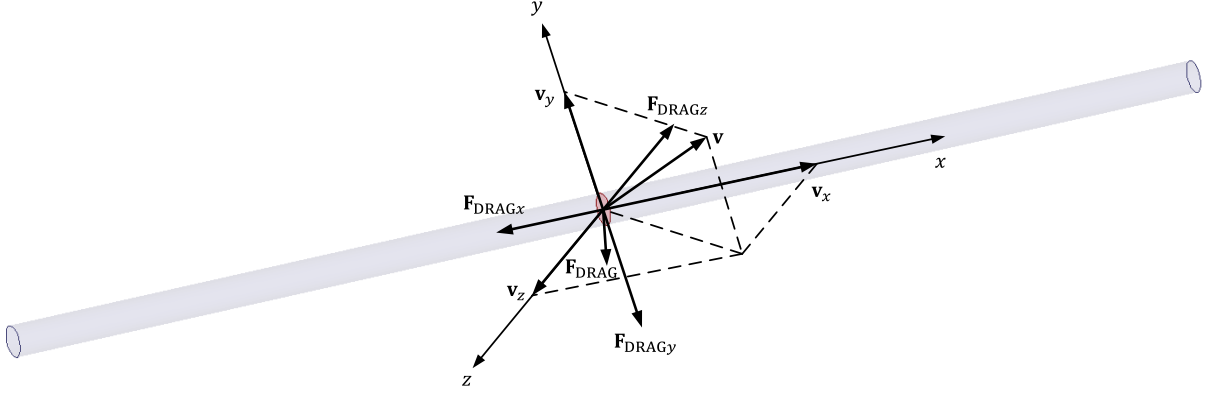


Figure 23. Decomposition of the velocity to calculate the drag force on the nanowire.

Because there is no torque along x axis, the rotational motion of the nanowire can be treated as two separate rotations along y and z axes. The nanowire actually rotates around one “fixed” axis which is determined by ω_y and ω_z , shown in Figure 24. The composite of ω_y and ω_z , named $\boldsymbol{\omega}$, is the angular velocity of the nanowire. Since the direction of $\boldsymbol{\omega}$ is also perpendicular to the nanowire, a method similar to 2-D model in subsection 3.2.1 is used to calculate the drag torque. Therefore, the drag torque on the nanowire in 3-D space is

$$\mathbf{T}_{\text{DRAG}} = -\frac{(N^3-N)\pi\eta L^3 \boldsymbol{\omega}}{3N^3 \left[\ln(\frac{L}{Nr}) + 0.5 \right]}. \quad (4.12)$$

The projections of \mathbf{T}_{DRAG} onto y and z axes are the components of drag torque on two axes.

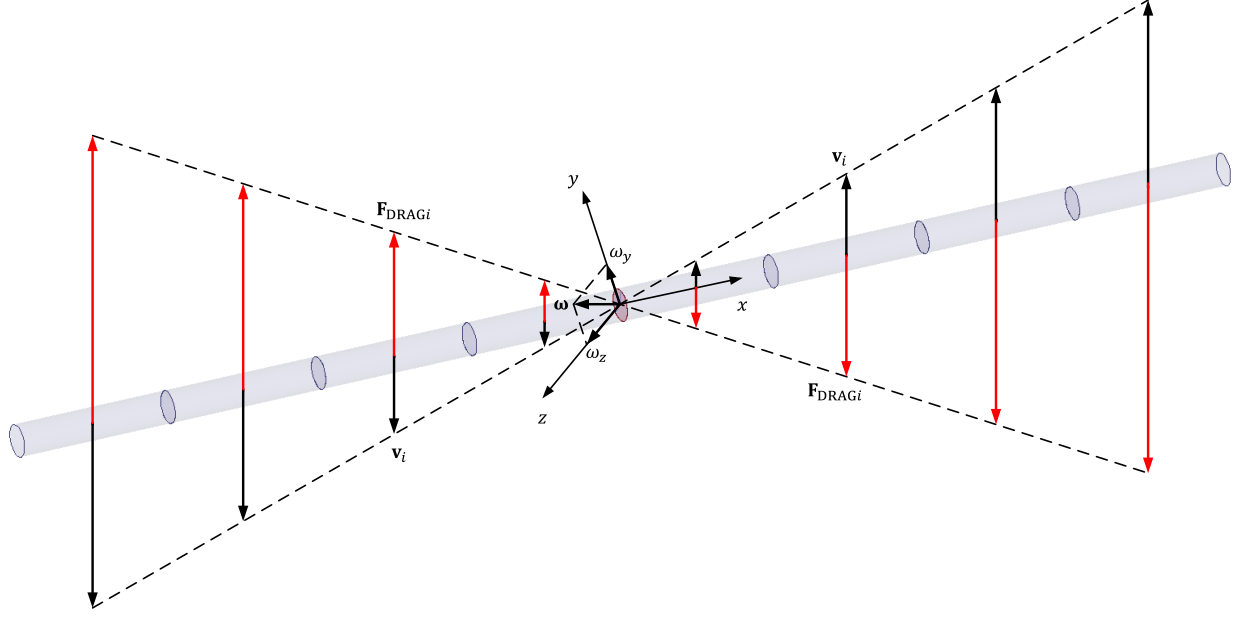


Figure 24. Even discretization of the nanowire to estimate the drag torque in 3-D space.

4.1.3 Rigid body dynamics

The motion of single nanowire can be treated as being composed of the translational motion of the center of nanowire and the rotational motion around the center. In order to describe the motion of the nanowire, we define a global inertial XYZ frame, a local inertial $x'y'z'$ frame and a body-fixed xyz frame with the origin o fixed on the center of the nanowire, as shown in Figure 25. The local inertial $x'y'z'$ frame and the body-fixed xyz frame are initially coincide before each rotational motion in the numerical simulation. Let $(\mathbf{I}, \mathbf{J}, \mathbf{K})$, $(\mathbf{i}', \mathbf{j}', \mathbf{k}')$, and $(\mathbf{i}, \mathbf{j}, \mathbf{k})$ be the unit vectors for the XYZ frame, $x'y'z'$ frame, and xyz frame, respectively. The unit vectors for the xyz frame $(\mathbf{i}, \mathbf{j}, \mathbf{k})$ are set to be coincide with the principal axes a, b, c . Given the coordinates of o , and three body-fixed reference points A, B , and C ($\overline{oA} = \mathbf{i}$, $\overline{oB} = \mathbf{j}$, $\overline{oC} = \mathbf{k}$) in global frame, the transformation from the global inertial XYZ frame to the local inertial $x'y'z'$ frame, $[\mathbf{i}' \ \mathbf{j}' \ \mathbf{k}']' = \mathbf{Q}[\mathbf{I} \ \mathbf{J} \ \mathbf{K}]'$ can be determined,

$$\overline{oA} = (X_A - X_o)\mathbf{I} + (Y_A - Y_o)\mathbf{J} + (Z_A - Z_o)\mathbf{K} = \mathbf{i}', \quad (4.13)$$

$$\overline{oB} = (X_B - X_o)\mathbf{I} + (Y_B - Y_o)\mathbf{J} + (Z_B - Z_o)\mathbf{K} = \mathbf{j}', \quad (4.14)$$

$$\overline{oC} = (X_C - X_o)\mathbf{I} + (Y_C - Y_o)\mathbf{J} + (Z_C - Z_o)\mathbf{K} = \mathbf{k}', \quad (4.15)$$

which can be written in a matrix form,

$$\begin{bmatrix} \mathbf{i}' \\ \mathbf{j}' \\ \mathbf{k}' \end{bmatrix} = \begin{bmatrix} X_A - X_o & Y_A - Y_o & Z_A - Z_o \\ X_B - X_o & Y_B - Y_o & Z_B - Z_o \\ X_C - X_o & Y_C - Y_o & Z_C - Z_o \end{bmatrix} \begin{bmatrix} \mathbf{I} \\ \mathbf{J} \\ \mathbf{K} \end{bmatrix} = \mathbf{Q} \begin{bmatrix} \mathbf{I} \\ \mathbf{J} \\ \mathbf{K} \end{bmatrix}. \quad (4.16)$$

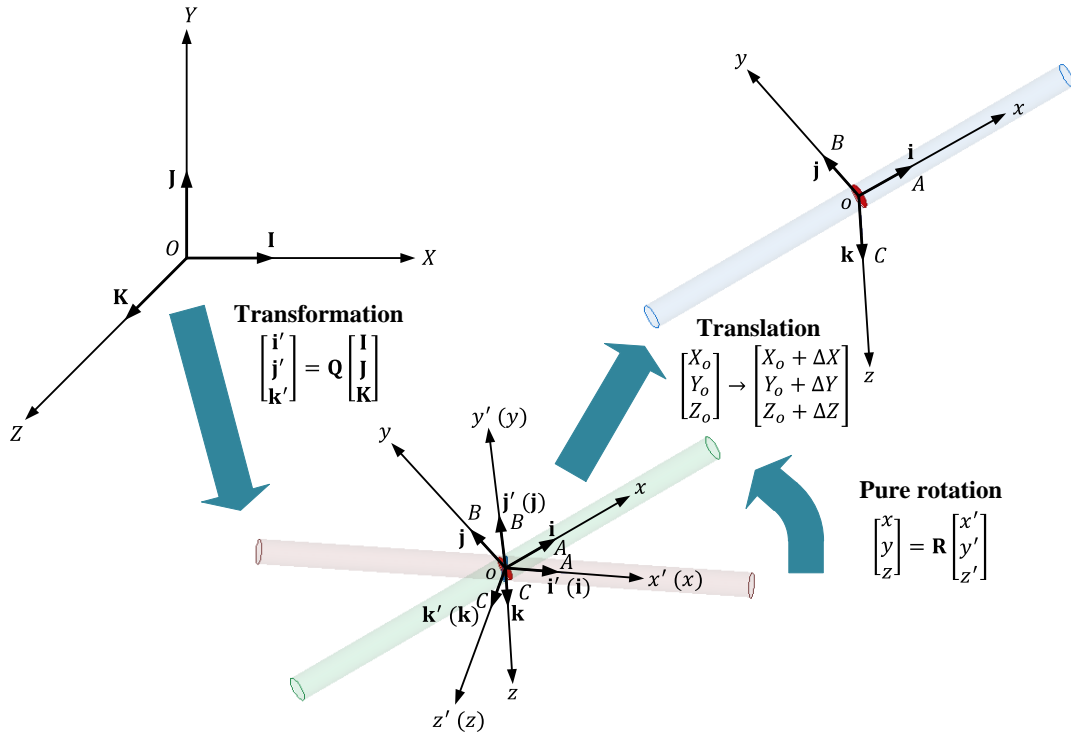


Figure 25. The motion of single nanowire in 3D space.

The translational motion is investigated in the global inertial XYZ frame because we need to judge the exact position of the nanowire in 3-D space. In the global inertial XYZ frame, the translational motion of the nanowire satisfies Newtonian dynamics,

$$m\ddot{X} = F_X, \quad (4.17)$$

$$m\ddot{Y} = F_Y, \quad (4.18)$$

$$m\ddot{Z} = F_Z, \quad (4.19)$$

where F_X , F_Y , and F_Z denote the three orthogonal components of the total force on the nanowire along X , Y , and Z axes, respectively. The position of the center of nanowire (X , Y , Z) and linear velocities (\dot{X} , \dot{Y} , \dot{Z}) at time t_0 are known from the calculation of previous step. The position and velocities provide the information of DEP force and drag force, which eventually imply F_X , F_Y , and F_Z at time t_0 . The differential equations (4.17)-(4.19) thereby can be solved to determine (X , Y , Z) and linear velocities (\dot{X} , \dot{Y} , \dot{Z}) at time $t_0 + \Delta t$.

The translational motion and rotational motion are independent and take place simultaneously. The general motion of the nanowire is therefore equivalent to a rotation about an axis through the center of mass at time t_0 , followed by a translation of the nanowire resulting in the correct final position of the center of mass at time $t_0 + \Delta t$. It is more convenient to characterize the rotational motion in the body-fixed xyz frame since it is straightforward to define the moment of inertia. The orientation of the body-fixed xyz frame relative to the local inertial $x'y'z'$ frame is given a rotation matrix \mathbf{R} [75],

$$\begin{bmatrix} x \\ y \\ z \end{bmatrix} = \mathbf{R} \begin{bmatrix} x' \\ y' \\ z' \end{bmatrix} = \begin{bmatrix} R_{xx} & R_{xy} & R_{xz} \\ R_{yx} & R_{yy} & R_{yz} \\ R_{zx} & R_{zy} & R_{zz} \end{bmatrix} \begin{bmatrix} x' \\ y' \\ z' \end{bmatrix} = \begin{bmatrix} \mathbf{i} \cdot \mathbf{i}' & \mathbf{i} \cdot \mathbf{j}' & \mathbf{i} \cdot \mathbf{k}' \\ \mathbf{j} \cdot \mathbf{i}' & \mathbf{j} \cdot \mathbf{j}' & \mathbf{j} \cdot \mathbf{k}' \\ \mathbf{k} \cdot \mathbf{i}' & \mathbf{k} \cdot \mathbf{j}' & \mathbf{k} \cdot \mathbf{k}' \end{bmatrix} \begin{bmatrix} x' \\ y' \\ z' \end{bmatrix}. \quad (4.20)$$

In the body-fixed xyz frame, the rotational motion of the nanowire is governed by the familiar Euler equations [75, 76],

$$I_{xx}\dot{\omega}_x + (I_{zz} - I_{yy})\omega_y\omega_z = T_x, \quad (4.21)$$

$$I_{yy}\dot{\omega}_y + (I_{xx} - I_{zz})\omega_z\omega_x = T_y, \quad (4.22)$$

$$I_{zz}\dot{\omega}_z + (I_{yy} - I_{xx})\omega_x\omega_y = T_z, \quad (4.23)$$

where I_{xx} , I_{yy} , and I_{zz} are the self-moment of inertia around x , y , and z axes, respectively, T_x , T_y , and T_z are the three components of total torques along x , y , and z axes, respectively. Since there is no spin rotation around x axis and no x component external torque, and $I_{yy} = I_{zz}$, Euler equations can be simplified to

$$I_{yy}\dot{\omega}_y = T_y, \quad (4.24)$$

$$I_{zz}\dot{\omega}_z = T_z \quad (4.25)$$

Given ω_y , ω_z , T_y , and T_z at time t_0 , the two differential equations (4.24) and (4.25) can be integrated numerically to give ω_y and ω_z as functions of time during the interval from t_0 to $t_0 + \Delta t$,

$$\omega_y(t) = \omega_y(t_0) + \frac{T_y}{I_{yy}}(t - t_0) \quad t_0 \leq t \leq t_0 + \Delta t, \quad (4.26)$$

$$\omega_z(t) = \omega_z(t_0) + \frac{T_z}{I_{zz}}(t - t_0) \quad t_0 \leq t \leq t_0 + \Delta t. \quad (4.27)$$

Unlike linear velocities in translational motion, the orientation of the nanowire cannot be obtained by simple integration of angular velocities ω s. Getting the orientation of the nanowire from the angular velocities requires more mathematical machinery like Euler angles or Euler parameters. Compared with Euler angles, Euler parameters, or quaternions, have the advantages of having no singularity problems and only one equation of constraint. Thus, they exhibit a good balance between overall accuracy and computational efficiency [75].

Although the rotational motion can be described by three simultaneous rotations around principal axes of the nanowire, the most general rotational motion of the nanowire is equivalent to a single rotation around some axis through the center of mass. Suppose the direction of the axis of rotation is given by

$$\mathbf{a} = a_x \mathbf{i} + a_y \mathbf{j} + a_z \mathbf{k}, \quad (4.28)$$

where the scalar a_s are constrained by the relation

$$a_x^2 + a_y^2 + a_z^2 = 1. \quad (4.29)$$

Let ϕ ($0 \leq \phi \leq \pi$) be the angle of rotation of the body-fixed frame relative to the local inertial frame, where positive ϕ is measured in a right-hand sense about the unit vector \mathbf{a} . The Euler parameters, or quaternions, are then defined in terms of a_s and ϕ [75, 76],

$$\epsilon_x = a_x \sin \frac{\phi}{2}, \quad (4.30)$$

$$\epsilon_y = a_y \sin \frac{\phi}{2}, \quad (4.31)$$

$$\epsilon_z = a_z \sin \frac{\phi}{2}, \quad (4.32)$$

$$\eta = \cos \frac{\phi}{2}. \quad (4.33)$$

The quaternions are constrained by a single equation,

$$\epsilon_x^2 + \epsilon_y^2 + \epsilon_z^2 + \eta^2 = 1. \quad (4.34)$$

The kinematic equations described by quaternions are

$$\dot{\epsilon}_x = \frac{1}{2}(\omega_z \epsilon_y - \omega_y \epsilon_z + \omega_x \eta), \quad (4.35)$$

$$\dot{\epsilon}_y = \frac{1}{2}(\omega_x \epsilon_z - \omega_z \epsilon_x + \omega_y \eta), \quad (4.36)$$

$$\dot{\epsilon}_z = \frac{1}{2}(\omega_y \epsilon_x - \omega_x \epsilon_y + \omega_z \eta), \quad (4.37)$$

$$\dot{\eta} = -\frac{1}{2}(\omega_x \epsilon_x + \omega_y \epsilon_y + \omega_z \epsilon_z). \quad (4.38)$$

Upon numerical integration, the quaternions can be expressed as functions of time during the rotation takes place from t_0 to $t_0 + \Delta t$. The rotation matrix is able to be converted from quaternions,

$$\mathbf{R} = \begin{bmatrix} R_{xx} & R_{xy} & R_{xz} \\ R_{yx} & R_{yy} & R_{yz} \\ R_{zx} & R_{zy} & R_{zz} \end{bmatrix} = \begin{bmatrix} 1 - 2(\epsilon_y^2 + \epsilon_z^2) & 2(\epsilon_x \epsilon_y + \epsilon_z \eta) & 2(\epsilon_x \epsilon_z - \epsilon_y \eta) \\ 2(\epsilon_y \epsilon_x - \epsilon_z \eta) & 1 - 2(\epsilon_z^2 + \epsilon_x^2) & 2(\epsilon_y \epsilon_z + \epsilon_x \eta) \\ 2(\epsilon_z \epsilon_x + \epsilon_y \eta) & 2(\epsilon_z \epsilon_y - \epsilon_x \eta) & 1 - 2(\epsilon_x^2 + \epsilon_y^2) \end{bmatrix}, \quad (4.39)$$

which helps to obtain the new orientation of the body-fixed frame relative to the local inertial frame.

Because the nanowire has no spin rotation ($\omega_x = 0$), the machinery that using quaternions to characterize the rotational motion of the nanowire can be simplified significantly.

The direction of the rotation axis \mathbf{a} is determined by the angular velocities ω s, i.e. $a_x = 0$ and

$\frac{a_y}{a_z} = \frac{\omega_y}{\omega_z}$. Therefore, the quaternions defined in Equations (4.30)-(4.33) imply $\epsilon_x = 0$ and $\frac{\epsilon_y}{\epsilon_z} =$

$\frac{\omega_y}{\omega_z}$. The kinematic differential equations on quaternions described in (4.35)-(4.38) are simplified

for nanowire,

$$\dot{\epsilon}_x = 0, \quad (4.40)$$

$$\dot{\epsilon}_y = \frac{1}{2}\omega_y\eta, \quad (4.41)$$

$$\dot{\epsilon}_z = \frac{1}{2}\omega_z\eta, \quad (4.42)$$

$$\dot{\eta} = -\frac{1}{2}(\omega_y\epsilon_y + \omega_z\epsilon_z). \quad (4.43)$$

Since ϵ_x remains zero, we can disregard Equation (4.40) and express the other three in the matrix form,

$$[\dot{\epsilon}_y \quad \dot{\epsilon}_z \quad \dot{\eta}]^T = \begin{bmatrix} 0 & 0 & \frac{1}{2}\omega_y \\ 0 & 0 & \frac{1}{2}\omega_z \\ -\frac{1}{2}\omega_y & -\frac{1}{2}\omega_z & 0 \end{bmatrix} [\epsilon_y \quad \epsilon_z \quad \eta]^T. \quad (4.44)$$

At time t_0 , $\phi = 0$, which implies the initial value of vector $[\epsilon_y \quad \epsilon_z \quad \eta]^T$ is $[0 \quad 0 \quad 1]^T$. Hence,

Equation (4.44) can be addressed numerically using common Runge-Kutta method to compute

the value of $[\epsilon_y \quad \epsilon_z \quad \eta]^T$ at time $t_0 + \Delta t$ [77, 78]. Substituting the value of $[\epsilon_y \quad \epsilon_z \quad \eta]^T$ at

time $t_0 + \Delta t$ into Equation (4.39) yields the rotation matrix \mathbf{R} after the nanowire completed the

rotational motion during the time interval from time t_0 to $t_0 + \Delta t$.

The translational motion is needed to be incorporated with the rotational motion during the time interval from time t_0 to $t_0 + \Delta t$ to find the exact position and orientation of the nanowire in the global inertial frame. Suppose the center of mass is translated from coordinates (X_o, Y_o, Z_o) to $(X_o + \Delta X, Y_o + \Delta Y, Z_o + \Delta Z)$ in the global inertial frame. In body-fixed xyz frame, the coordinates of the three body-fixed reference points keep constant, i.e. $(x_A, y_A, z_A) = (1, 0, 0)$, $(x_B, y_B, z_B) = (0, 1, 0)$, and $(x_C, y_C, z_C) = (0, 0, 1)$. Therefore, the coordinates of these reference points in the local inertial $x'y'z'$ frame at time $t_0 + \Delta t$ can be obtained through the calculated rotation matrix \mathbf{R} . For example,

$$[x'_A \quad y'_A \quad z'_A]^T = \mathbf{R}^{-1}[x_A \quad y_A \quad z_A]^T = \mathbf{R}^T[x_A \quad y_A \quad z_A]^T. \quad (4.45)$$

The calculated coordinates of reference point A is obtained through the pure rotation relative to the local inertial frame. The transformation matrix \mathbf{Q} described in Equation (4.16) is then introduced to calculate the coordinates of point A in the global inertial frame, (X_A, Y_A, Z_A) . However, the exact coordinates of reference point A in global inertial frame are supposed to take the translation into consideration,

$$[X_A \quad Y_A \quad Z_A]^T_{exact} = [X_A \quad Y_A \quad Z_A]^T + [\Delta X \quad \Delta Y \quad \Delta Z]^T. \quad (4.46)$$

Similarly, the exact coordinates of reference points B and C in global inertial frame can be acquired. The positions of the three reference points and the center of mass can uniquely determine the new position and orientation of the nanowire at time $t_0 + \Delta t$. The local inertial $x'y'z'$ frame is updated to coincide the current body-fixed xyz frame, and the numerical simulation is then performed iteratively to estimate the trajectory of the nanowire in 3-D space.

4.2 SIMULATION STUDIES BASED ON 3-D MODELING

4.2.1 Numerical simulation of nanowire's trajectory

A pair of electrodes with a gap of 3 μm is constructed in COMSOL software. By applying a 1 MHz (to ensure positive DEP forces on nanowires), 10 V excitation across the electrodes, a non-uniform electric field is simulated. Figure 26 shows the electric field \mathbf{E} and the gradient of electric field square $\nabla|\mathbf{E}|^2$ in the vertical plane along the electrodes. Both the electric field \mathbf{E} and the gradient $\nabla|\mathbf{E}|^2$ have larger magnitudes at the region near the electrodes, which implies the positive DEP has the ability to drive the nanowire towards the electrodes.

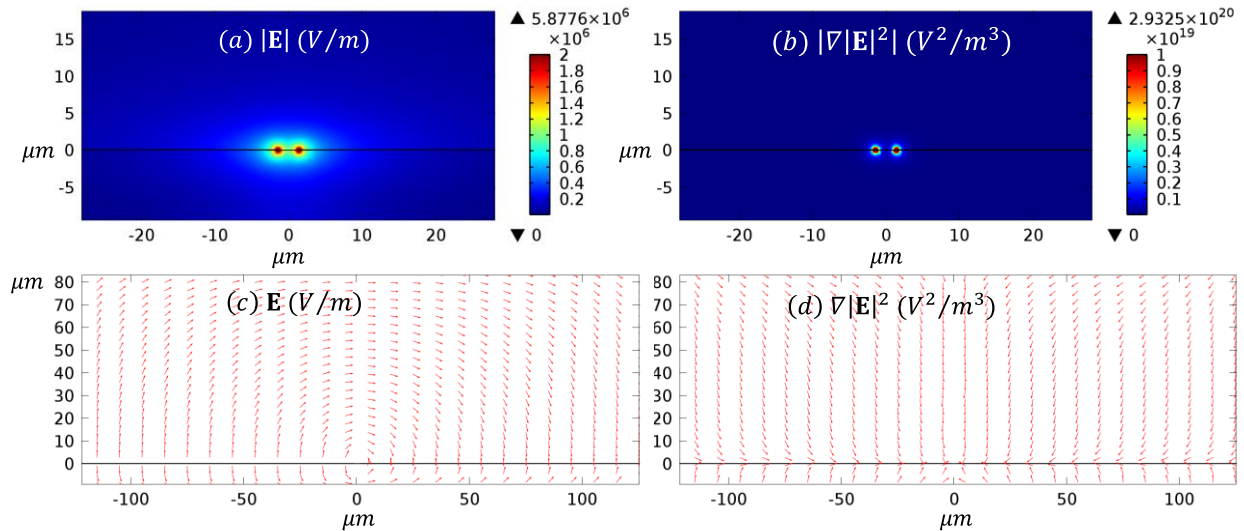


Figure 26. The electric field distribution generated by triangular electrodes in the vertical XOZ plane. (a) The magnitude of the electric field \mathbf{E} . (b) The magnitude of the gradient form $\nabla|\mathbf{E}|^2$. (c) The vector plot of the electric field \mathbf{E} . (d) The vector plot of the gradient form $\nabla|\mathbf{E}|^2$.

In order to accurately predict a nanowire's trajectory through numerical simulation, it is essential to select a sufficiently small time duration for each step. A threshold (5 nm) was set on

the displacement of the nanowire to adaptively control the time step, such that the DEP force and torque could only have very tiny changes during that step. Moreover, another criterion was created to monitor the velocity and rotational velocity to ensure that the magnitudes of drag force and torque would not exceed those of DEP force and torque. Assuming a 10- μm -long nanowire with a conductivity of 10^4 S/m is initially along the electrodes in the upper space (the initial coordinates of the nanowire's center is $(0, 0, 30)$ μm), its trajectory can be predicted through numerical simulation, as shown in Figure 27. Because of the effect of positive DEP, the nanowire is driven towards the electrodes along the direction of the gradient $\nabla|\mathbf{E}|^2$. Moreover, the nanowire tends to align with the electric field \mathbf{E} during the assembly, which implies the DEP torque dominates over the torque generated by DEP forces. The nanowire receives larger DEP force and torque when it is closer to the electrodes, thereby increasing its translational and rotational velocities gradually. At time 1.5 ms, one end of the nanowire hits one electrode and cannot move freely because of strong Van der Waals force. Nevertheless, the nanowire can rotate around the attaching point under the effect of DEP torque and the torque generated by DEP forces. Moreover, the Van der Waals force and the gravitational force are supposed to affect the nanowire's rotation. However, the magnitudes of the two forces are approximately 10^{-12} N and 10^{-15} N, which are much smaller than that of DEP force (10^{-9} N). Therefore, it is the DEP torque and the torque generated by DEP forces that mainly contribute to drive the nanowire to bridge the electrodes ultimately.

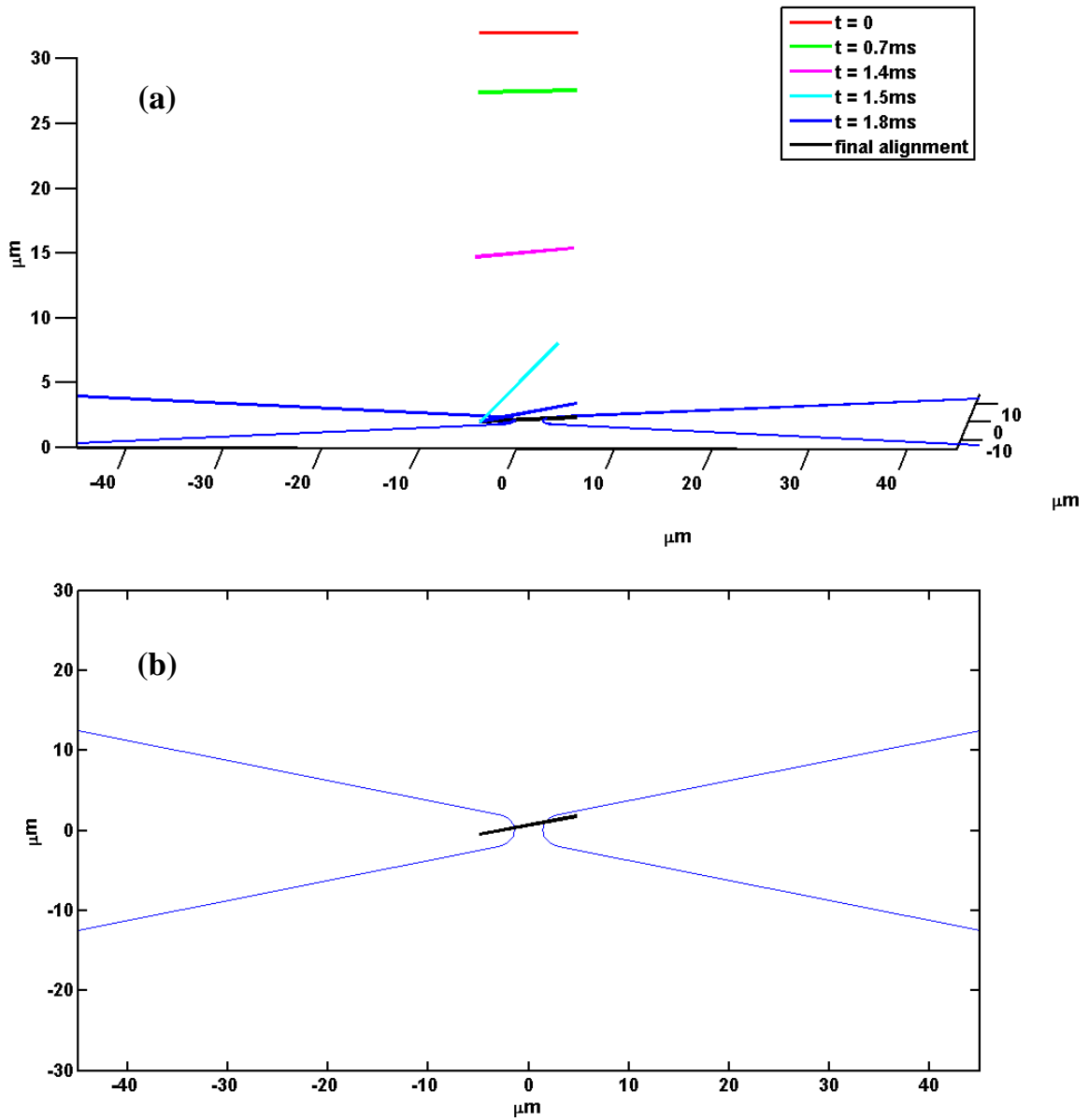


Figure 27. (a) The trajectory of nanowire starting from $(0, 0, 30)$ μm . (b) The final alignment of the nanowire.

The nanowire, however, cannot always bridge the electrodes. As shown in Figure 28, a nanowire along the electrodes begins its motion from $(30, 0, 30)$ μm . Similar to previous situation, the nanowire is aligned with the direction of the electric field \mathbf{E} and translates towards the electrodes along the gradient $\nabla|\mathbf{E}|^2$. After hitting one electrode, the DEP torque, the torque

generated by DEP forces, Van der Waals force, and gravitational force drive the nanowire to attach on the surface of the electrode. Instead of bridging the electrodes, the nanowire comes from the side of the electrodes can only attach on the surface of one electrode.

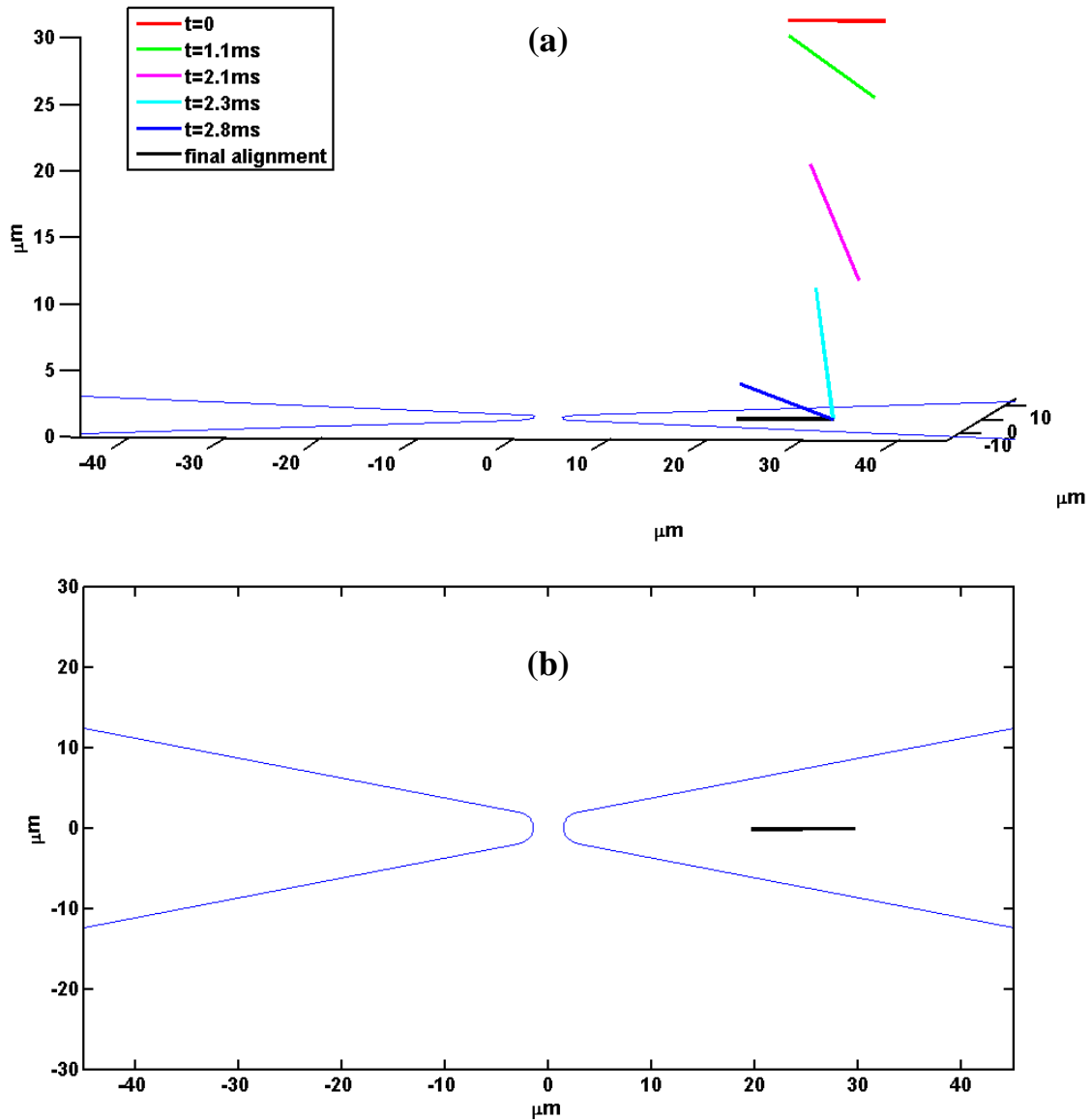


Figure 28. (a) The trajectory of nanowire starting from $(30, 0, 30) \mu\text{m}$. (b) The final alignment of the nanowire.

4.2.2 Determining the boundary for successful alignment by simulation

Depends on its initial position and orientation, the nanowire either bridges the electrodes or attaches on the surface of one electrode after a standard DEP assembly as shown in last section. In order to find the neighborhood in which nanowires are more likely to bridge the electrodes, we performed a large number of numerical simulations on the trajectory of nanowires with different initial conditions. Figure 29 shows the initial positions of nanowires for the simulation. We considered six vertical planes that along the electrodes and with different distances from the electrodes: 0, 6 μm , 12 μm , 18 μm , 24 μm , and 30 μm . The nanowires were assumed at four possible heights above the electrodes: 10 μm , 20 μm , 30 μm , and 40 μm . At each initial position, we considered three different orientations: along the electrodes, 30° orientation with the direction of electrodes and 60° orientation with the electrode surface, and perpendicular to the electrode surface. In each vertical plane, as we gradually move the initial position of the nanowire from the center to the side of electrodes, the boundary for successful alignment in this plane can be obtained. After performing numerical simulation for nanowires started from the six vertical planes, the estimated boundary is summarized in different vertical planes and at different heights, as shown in Table 1. Because of symmetry, the whole boundary of the neighborhood in which nanowires are more likely to bridge electrodes can be plotted accordingly, as shown in Figure 30. The boundary becomes narrower at larger height and larger distance away from the electrodes. Considering the vertical plane along the electrodes ($y = 0 \mu\text{m}$), at a higher distance above the electrodes (for example, $x = 10 \mu\text{m}$, $z = 40 \mu\text{m}$), the gradient $\nabla|\mathbf{E}|^2$ has a more dominant magnitude along z direction ($-1.1981 \times 10^{14} \text{ V}^2/\text{m}^3$) than that along x direction ($-5.4976 \times 10^{12} \text{ V}^2/\text{m}^3$), which causes the nanowire to have a much larger velocity downward than the

velocity toward the center of electrodes. Therefore the nanowire is more likely to attach on the surface of one electrode. At a lower distance above the electrodes (for example, $x = 10 \mu\text{m}$, $z = 20 \mu\text{m}$), the subcomponents of the gradient $\nabla|\mathbf{E}|^2$ along both x direction ($-1.2508 \times 10^{14} \text{ V}^2/\text{m}^3$) and z direction ($-8.6579 \times 10^{14} \text{ V}^2/\text{m}^3$) are comparable, which drives the nanowire to move toward the center of electrodes while translating downward. Hence the nanowire has the ability to bridge the electrodes. The narrower boundary at larger distance away from the electrodes can also be explained through similar method.

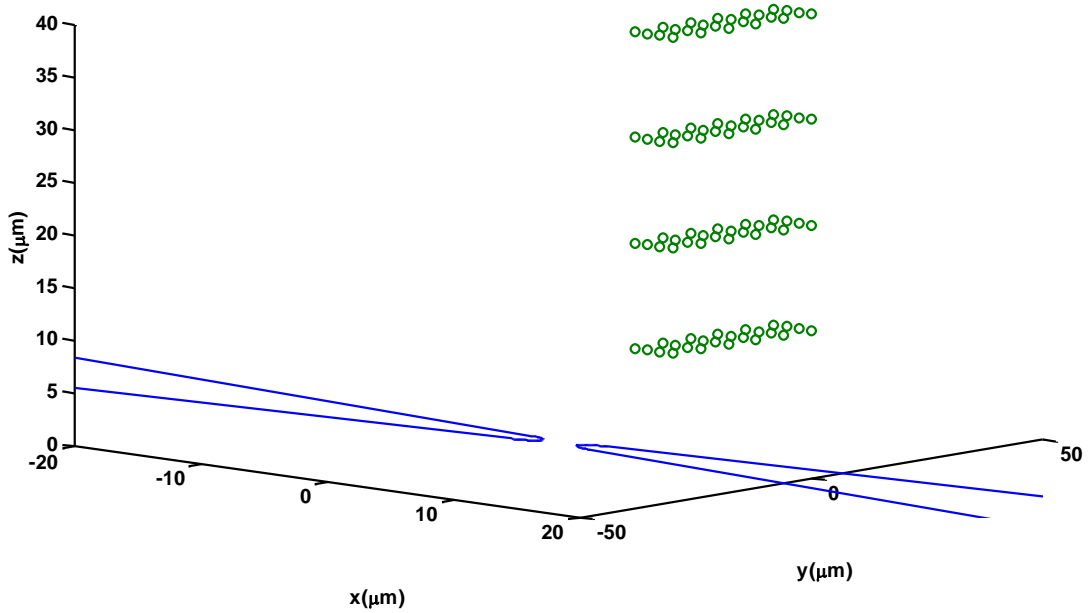


Figure 29. Initial positions of nanowire considered in the simulation.

Table 1 Estimated boundary in x axis for each vertical plane (in unit of μm)

$y \backslash z$	10	20	30	40
0	12	10	8	7
6	7	7	7	6
12	7	7	7	6
18	6	6	5	5
24	6	6	4	4
30	4	4	3	3

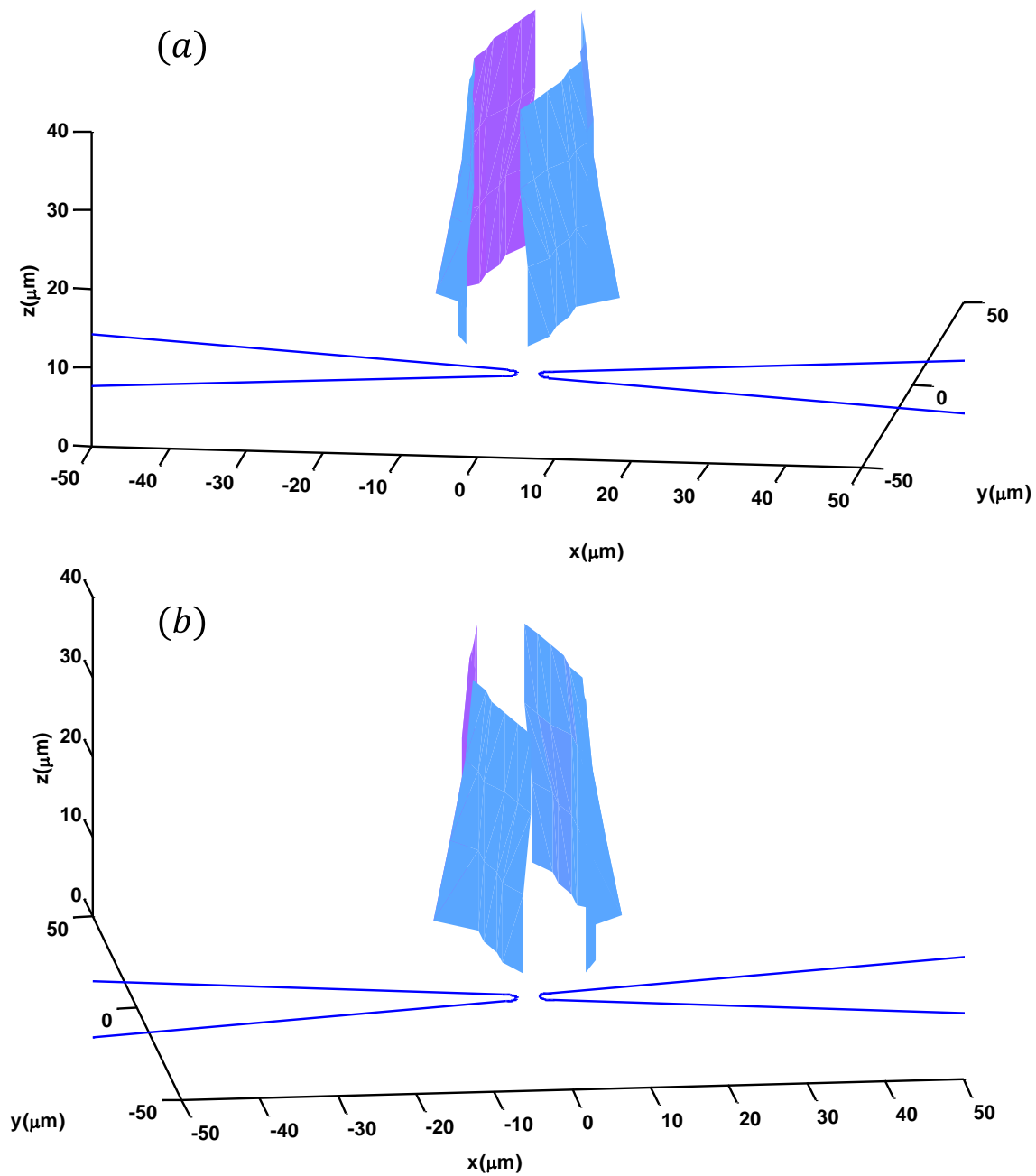


Figure 30. Different views of the whole boundary.

The numerical simulation was then performed for different situations by considering the gap size and the length of the nanowire. The boundaries for success alignment in the vertical plane along the electrodes for three different situations are compared in Table 2 and plotted out

in Figure. 31. The boundary for each situation becomes narrower at larger height above the electrodes. Since the long nanowire can bridge the electrodes even if it attaches on a position that far from the gap, the boundary for a 10- μm -long nanowire is wider than that for a 5- μm -long nanowire. In addition, it is more likely for a nanowire to bridge electrodes with smaller gap. Therefore, for a 5- μm -long nanowire, the boundary for 1 μm gap is wider than that for 3 μm gap. Those findings on the neighborhood are expected to provide practical guidance on DEP assembly. Knowing the gap size and the length of the nanowire, the neighborhood for successful alignment can be figured out through numerical simulations. A very small volume of nanowire suspension is then can be delivered across the electrode gap region through micro-pipette to confine the suspended nanowires within the computed neighborhood. Instead of randomly attaching on the surface of the electrodes, the nanowires are more likely to successfully bridge the electrodes after the DEP assembly.

Table 2 Estimated boundaries for three different situations in the vertical plane along the electrodes

z (μm)	3 μm gap, 10- μm -long nanowire	3 μm gap, 5- μm -long nanowire	1 μm gap, 5- μm -long nanowire
10	12	5	6
20	10	3	4
30	8	2	3
40	7	2	3

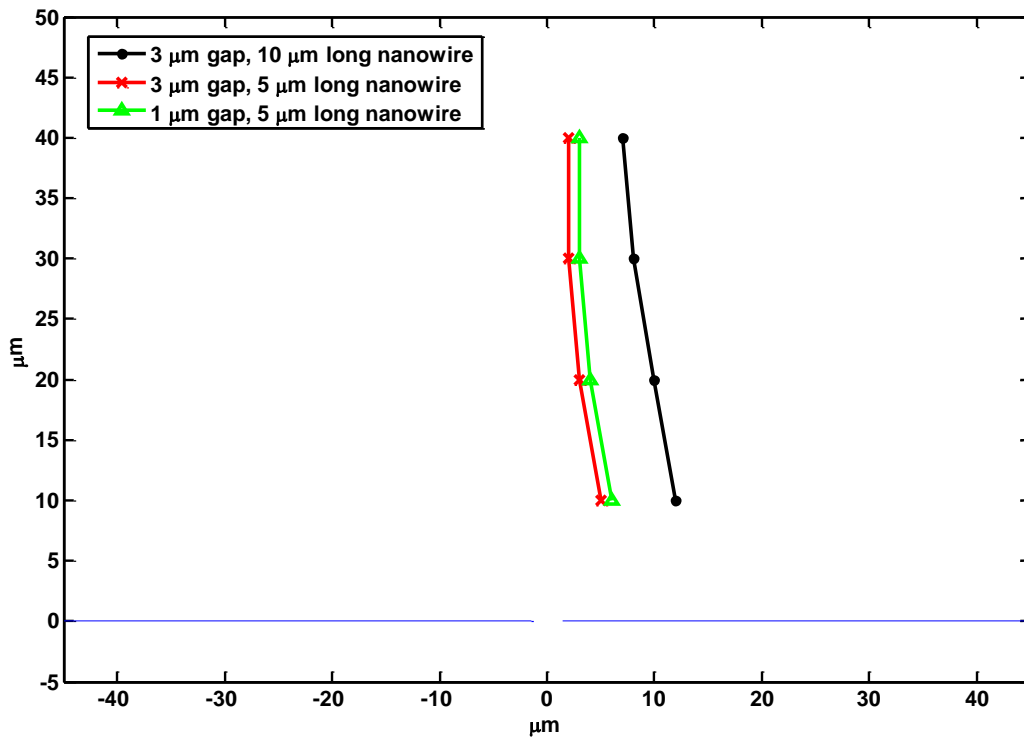


Figure 31. Comparison of the boundaries for three different situations.

5.0 NANOWIRE BASED GAS SENSOR ARRAY

We have deeply investigated the DEP assembly process for aligning the nanowire between two electrodes in Chapters 3 and 4. The predicted trajectory and alignment of the nanowire unveils the mechanism of DEP and provides practical guidance on experimental manipulation of nanowires. In this chapter, we present the application of nanowire based gas sensor array through DEP. The gas sensor array is then tested in a well-controlled environment. The collected outputs of the gas sensor array assists to interpret the gas concentration through machine learning algorithms.

5.1 FABRICATION OF NANOWIRE BASED GAS SENSOR ARRAY

The fabrication of nanowire based gas sensor array includes two steps: fabrication of electrode array and assembly of nanowires onto electrodes through DEP. The electrode fabrication involves photolithography, metal deposition, and lift off process, which has been described in details in Section 3.2. Figure 31 shows a picture of one fabricated electrode array on a 1 inch \times 1 inch quartz substrate. The device chip contains 4 pairs of electrodes, on which different nanowires can be assembled separately. Each electrode has a large pad, through which a conducting wire can be connected using silver glue, therefore enabling the feed through of an electrical signal. The left side electrodes are connected together to act as ground electrodes, and

each right side electrode is excited by an AC voltage signal to create a non-uniform electric field between the electrode pair, therefore assembling the nanowires. During each assembly, a 15 μL droplet of nanowire suspension is delivered over the corresponding electrode gap region. By setting the assembly time, the frequency and amplitude of the applied voltage signal, and the concentration of the nanowire suspension, the number of assembled nanowires can be controlled. Since the electrode pairs have very tiny gaps, it is of vital importance to prevent them from being destroyed by static charges. Thereby, we introduced an antistatic mat and an antistatic wrist strap to provide electrostatic discharge (ESD) protection. In addition, each electrode pair is always shorted through external circuits until being utilized during the DEP assembly or the gas sensing measurement. After accumulating much experience in DEP assembly, we can routinely assemble ZnO nanowires and CNTs onto electrodes.

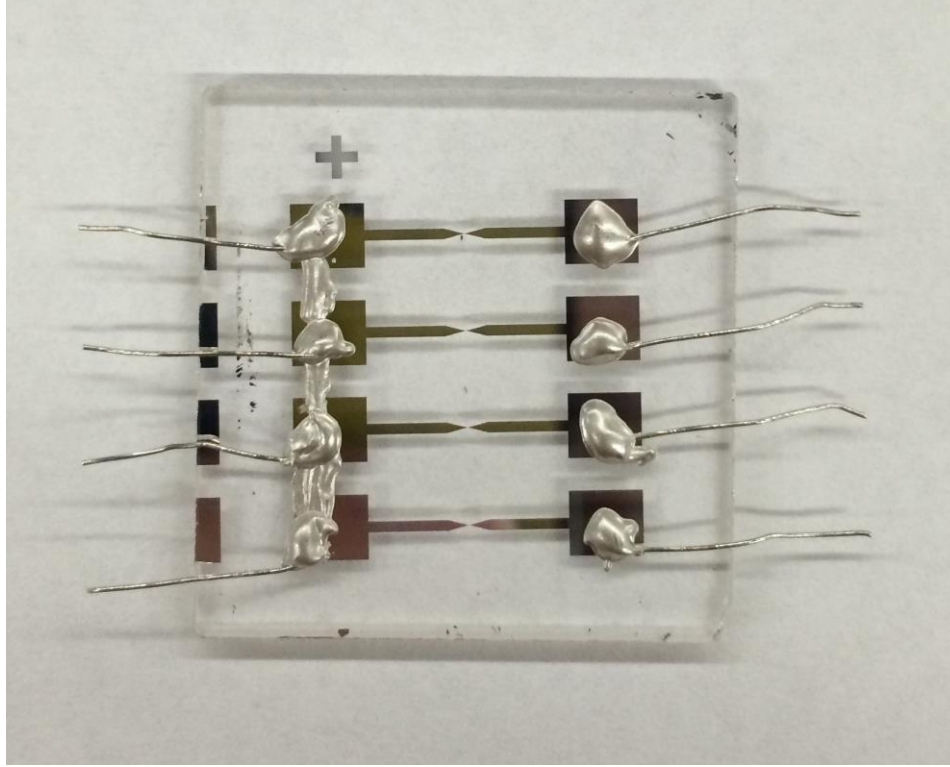


Figure 32. Electrode array fabricated on a 1 inch \times 1 inch quartz substrate.

5.2 GAS SENSING SYSTEM SETUP

To detect target gases with certain concentrations, the gas sensing system should be able to turn on/off the gas flow from different gas sources and control the concentration of target gases [79]. To test the gas sensor array's capability of estimating gas concentration, we used NH_3 as the target gas. N_2 was used as the dilution and carrier gas. The concentration of NH_3 in N_2 environment, which usually measures in mole fraction, was controlled by setting appropriate flow rates of NH_3 and N_2 ,

$$C = \frac{F_{\text{NH}_3} \rho_{\text{NH}_3} / M_{\text{NH}_3}}{F_{\text{NH}_3} \rho_{\text{NH}_3} / M_{\text{NH}_3} + F_{\text{N}_2} \rho_{\text{N}_2} / M_{\text{N}_2}}, \quad (5.1)$$

where F , ρ , and M are the flow rate, density, and molar mass of the corresponding gas, respectively. The detailed setup of the gas sensing system is illustrated in Figure 32. The flow rates of NH_3 and N_2 are well controlled through mass flow controllers (MKS Type 167A). The maximum flow rate of N_2 is 500 sccm (standard cubic centimeters per minute), while the minimum achievable flow rate of NH_3 is 1 sccm. Therefore, the minimum concentration of NH_3 for our system is around 0.2%. The gas mixture is then sent to a quartz tube chamber, inside which the gas sensor array chip is mounted on a ceramic plate and connected to the outside through electrical feed through. The I-V behaviors of the gas sensor array under different environments can be measured by the external switch circuit and a Keithley 2600 source meter. The measurement of each sensor is implemented independently. It is important to ensure other sensors are shorted by the switch circuit. A computer with high-speed GPIB controller and program (Test Script Builder, Keithely) is used for I-V curve measurements and data acquisitions.

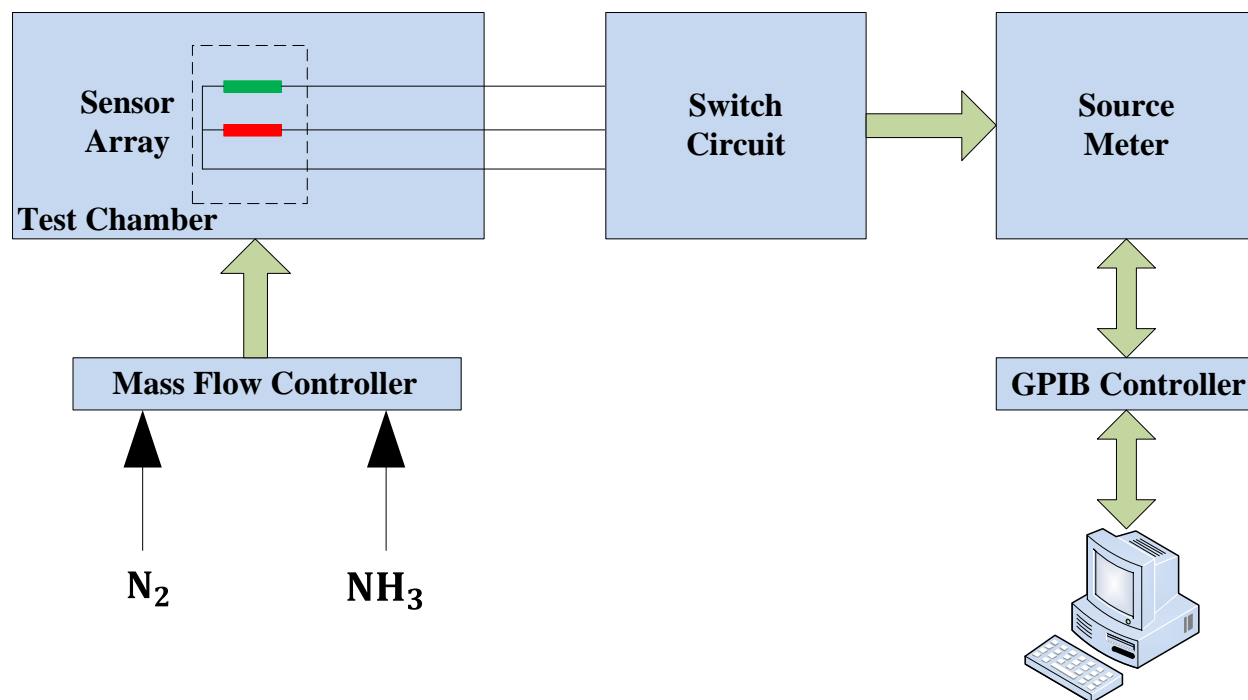


Figure 33. Gas sensing system setup.

5.3 ZNO NANOWIRE AND CNT BASED NH_3 SENSOR

NH_3 is a natural waste product of both livestock and industrial manufacturing, which adversely affects human and environmental health. Both ZnO nanowires and CNTs have been demonstrated to be promising transducers for NH_3 at elevated temperatures [42, 54]. However, since high temperature condition is not common when there is a need to monitor the presence of NH_3 , we want to measure the performance of the device at room temperature. We assembled ZnO nanowires and CNTs on two electrode pairs respectively on the same chip, as shown in Figure 34. Integrating two different materials on the same device provides more information than using single sensing element, thereby predicting the concentration of NH_3 better. Before measuring the response of the device in the gas sensing system, we annealed the chip in a

vacuum oven at 100 °C for 20 min to strengthen the contact between the sensing materials and the electrodes. Both sensors were then tested under different conditions.

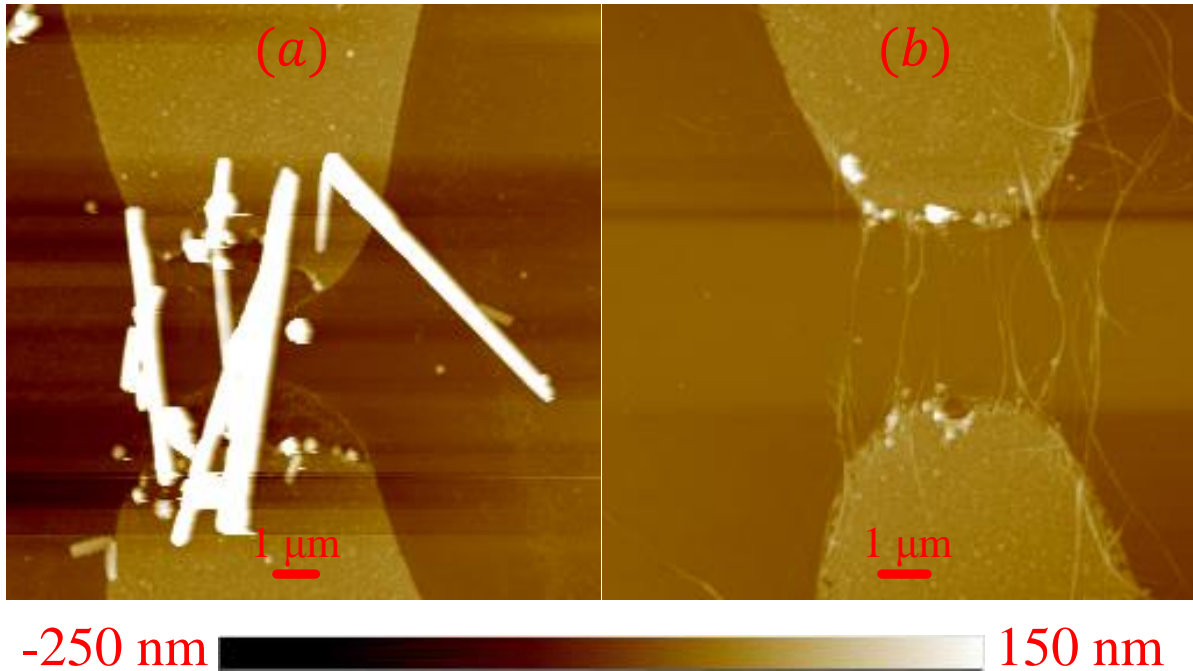


Figure 34. AFM images of assembled (a) ZnO nanowires and (b) CNTs on two electrode pairs of the same chip.

5.3.1 ZnO nanowire based NH₃ sensor

In Figure 35, the black line shows the original I-V curve of ZnO nanowire based device (Figure 33 (a)) under 200 sccm flow of N₂ at room temperature, which behaves as two reversely connected Schottky barriers. The blue line is the I-V curve of the device saturated under 5 sccm of NH₃ and 200 sccm of N₂ at room temperature. The conductance of ZnO nanowire is significantly improved, and the barrier height decreases dramatically. The observed change verifies the mechanism of sensing NH₃ using ZnO nanowire, as we discussed in Section 2.1.1.

Moreover, it demonstrates that ZnO nanowire based device can well detect NH₃ at room temperature.

A qualified electronic nose is also supposed to be able to recover to the initial state, such that it can be re-used under various conditions. The nanowire based sensors, however, can hardly recover at room temperature after being exposed to chemical vapors. For instance, single-walled carbon nanotube (SWNT) exposed to NO₂ is reported to fully recovered in Ar environment after 12 hours [54]. Researchers have proposed different methods to accelerate the recovery process. Kong et al [54] found that the SWNT based sensors can recover at 200 °C within 1 hour. ZnO nanowires exposed to NH₃ can be recovered within 10 s under the flow of dry air at 300 °C [80]. Li et al [81] demonstrated that ultraviolet (UV) light illumination accelerates the recovery process of SWNT based NO₂ sensors to about 10 min. However, since high temperature is not practical in real situations and integrating a UV source with the gas sensor is not convenient, an alternative approach is needed to recover ZnO nanowire based sensors.

We proposed to accelerate the recovery process by applying a DC voltage across ZnO nanowires while refreshing the chamber with N₂. Other lines in Figure 35 show the I-V curves of the device after applying a 5 V DC voltage under 200 sccm of N₂ at different time. After 5 min, the I-V curve (the red dashed line) coincides with the original curve (the black line), which indicates the device can be fully recovered by a DC bias during the refreshment with N₂ within a very short time. The applied DC bias creates a very high current intensity within the nanowire because of the extremely small size of nanowire. The high current intensity generates a high temperature within the body of nanowire, which accelerates desorption of NH₃ molecules from ZnO nanowire. Therefore, the ZnO nanowire based sensor can be recovered conveniently and tested under different concentrations of NH₃.

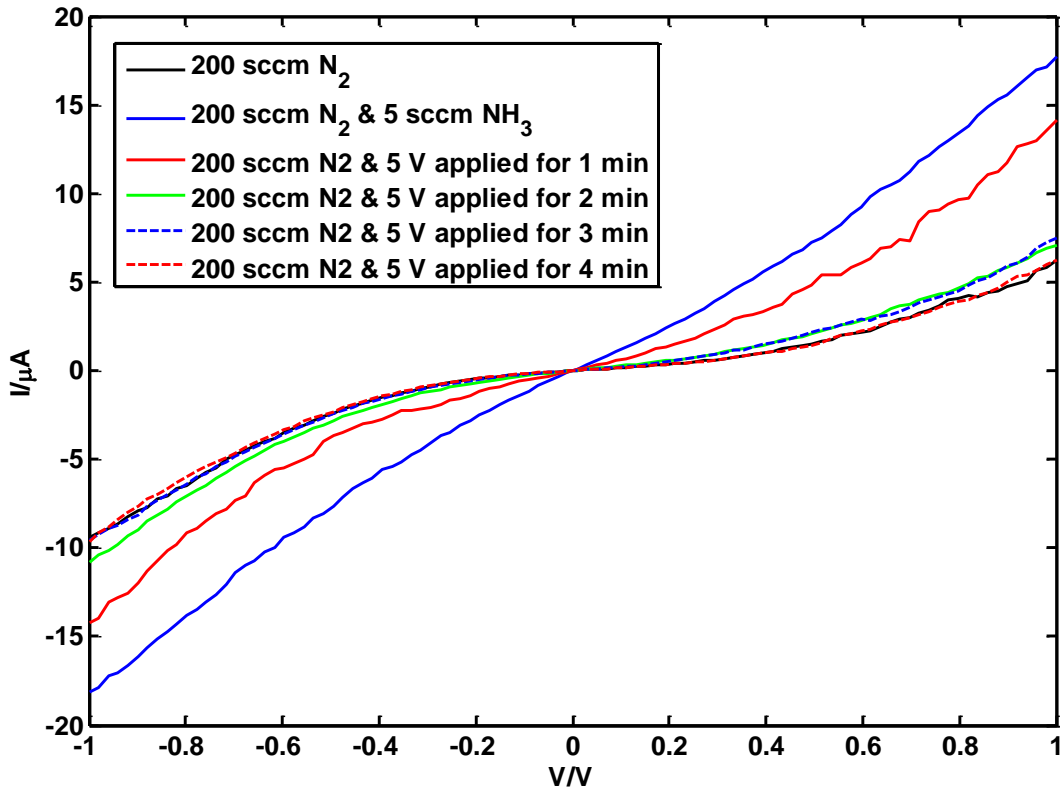


Figure 35. Sensing and recovery of ZnO nanowire based NH₃ sensor.

5.3.2 CNT based NH₃ sensor

Similar to the characterization on ZnO nanowire based NH₃ sensor, we tested the sensing capability of CNT based device (Figure 34 (b)) and realized fast recovery with DC bias, as shown in Figure 36. Unlike ZnO nanowire, CNT behaves an Ohmic contact. The decreased conductance of CNT in NH₃ environment indicates a decrease of electron concentration. The DC bias also helps the recovery process of CNT based sensor.

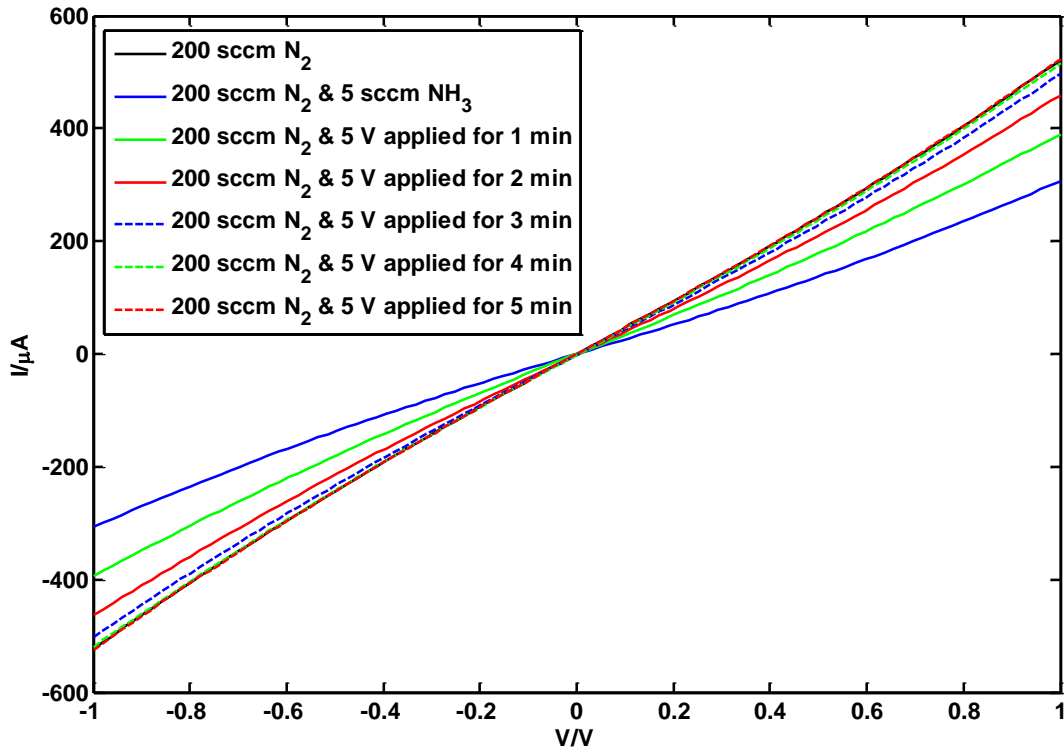


Figure 36. Sensing and recovery of CNT based NH_3 sensor.

5.4 NANOWIRE BASED GAS SENSOR ARRAY

In Section 5.3, it has been demonstrated that both ZnO nanowire and CNT can well sense NH_3 at room temperature. Applying DC biases across the sensing elements under the N_2 flow realizes fast recovery of the devices. The sensor array was then tested under different concentrations of NH_3 . Figure 37 shows the I-V curves of ZnO nanowire and CNT under different conditions. The conductance of ZnO nanowire increases as the concentration of NH_3 is enhanced. Oppositely, the increase of the concentration of NH_3 results in the reduction of the conductance of CNT. The change on both conductance of ZnO nanowire and CNT, therefore, can be used to indicate the

presence of NH_3 or even to estimate the concentration of NH_3 . To estimate the concentration of NH_3 from the collected data, it is important to extract useful features from the I-V curves in Figure 37. Conductance should be a good feature to represent an I-V curve. However, because of the existence of Schottky barriers, the conductance of ZnO nanowire or CNT varies depending on the applied voltage, as shown in the Conductance-Voltage curves in Figure 38. In the following study, we use the conductance of ZnO nanowire or CNT at zero voltage as the feature to represent the corresponding I-V curve. Moreover, it is essential to characterize the response of each sensor based on the conductance change when the device is exposed to a certain concentration of NH_3 . The fractional change in conductance, $\frac{\Delta G}{G_0} = \frac{G_{\text{target}} - G_0}{G_0}$ (G_{target} , G_0 are the conductance of the sensor in the presence of target gas and the initial conductance of the sensor in N_2), is an appropriate choice to represent the response. Figure 39 shows the response of both ZnO nanowire and CNT sensors in the presence of NH_3 of different concentrations.

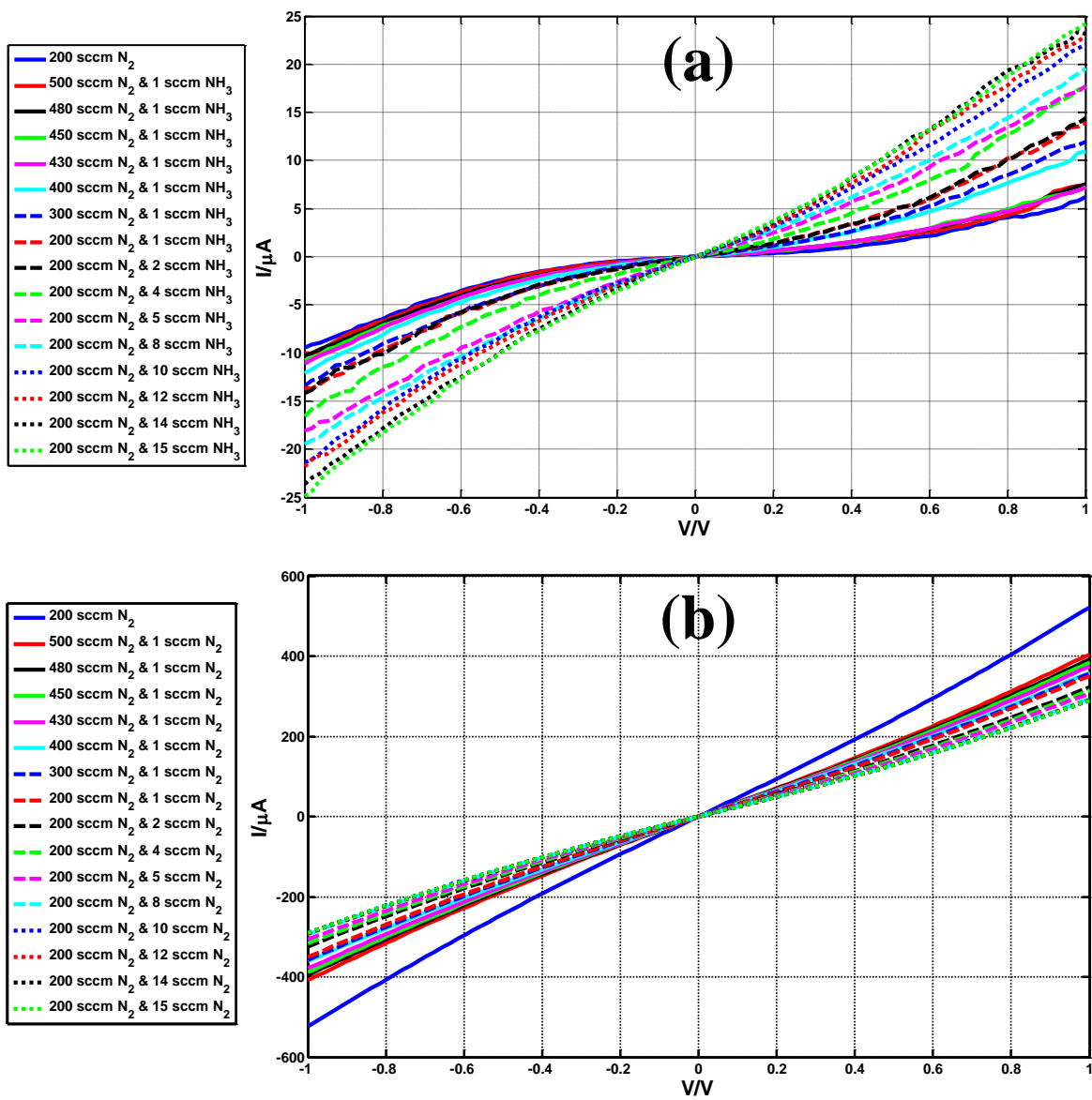


Figure 37. I-V curves of sensing elements of the sensor array under different conditions (a) ZnO nanowire

(b) CNT.

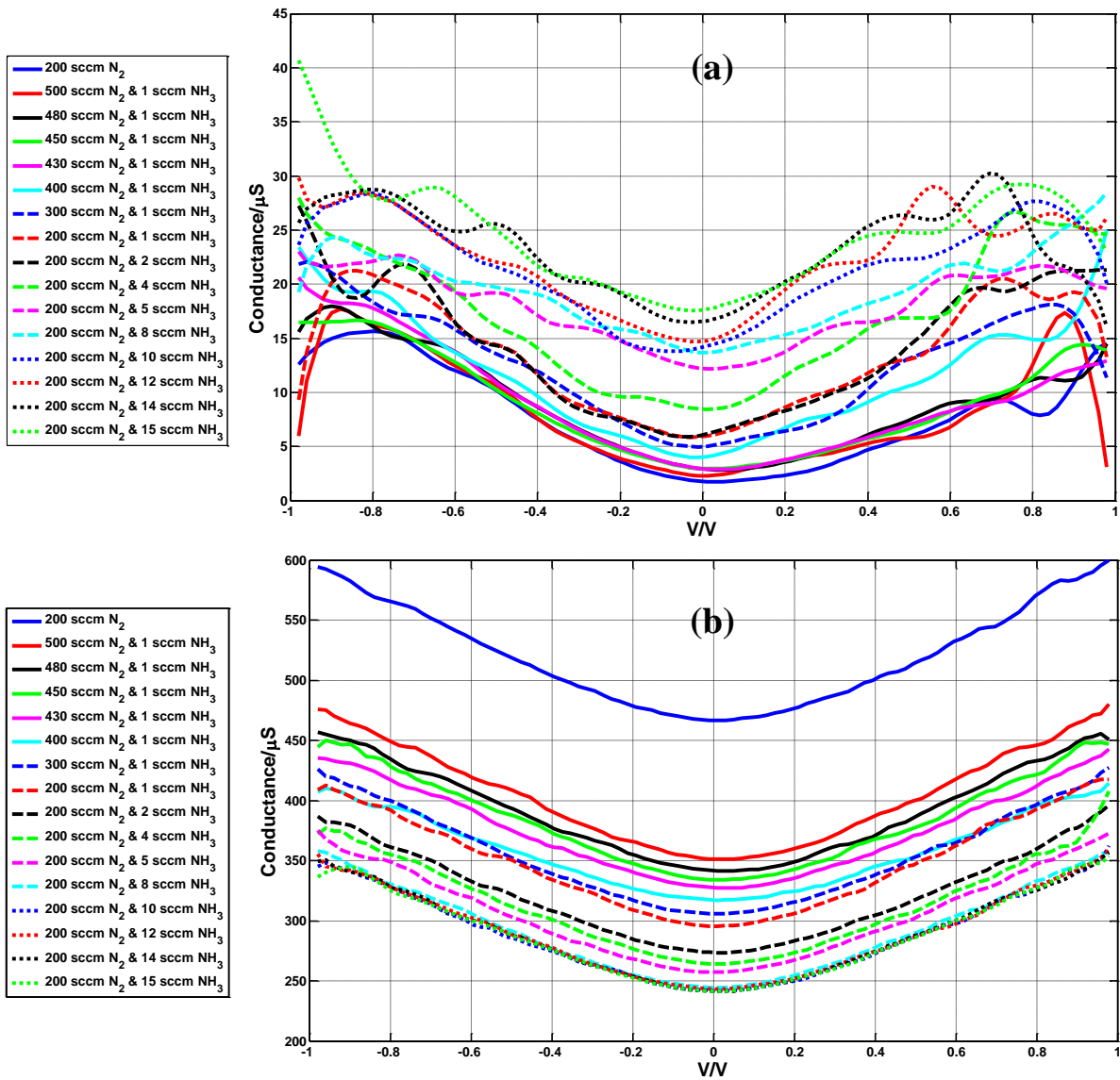


Figure 38. Conductance-Voltage curves of sensing elements of the sensor array under different conditions

(a) ZnO nanowire (b) CNT.

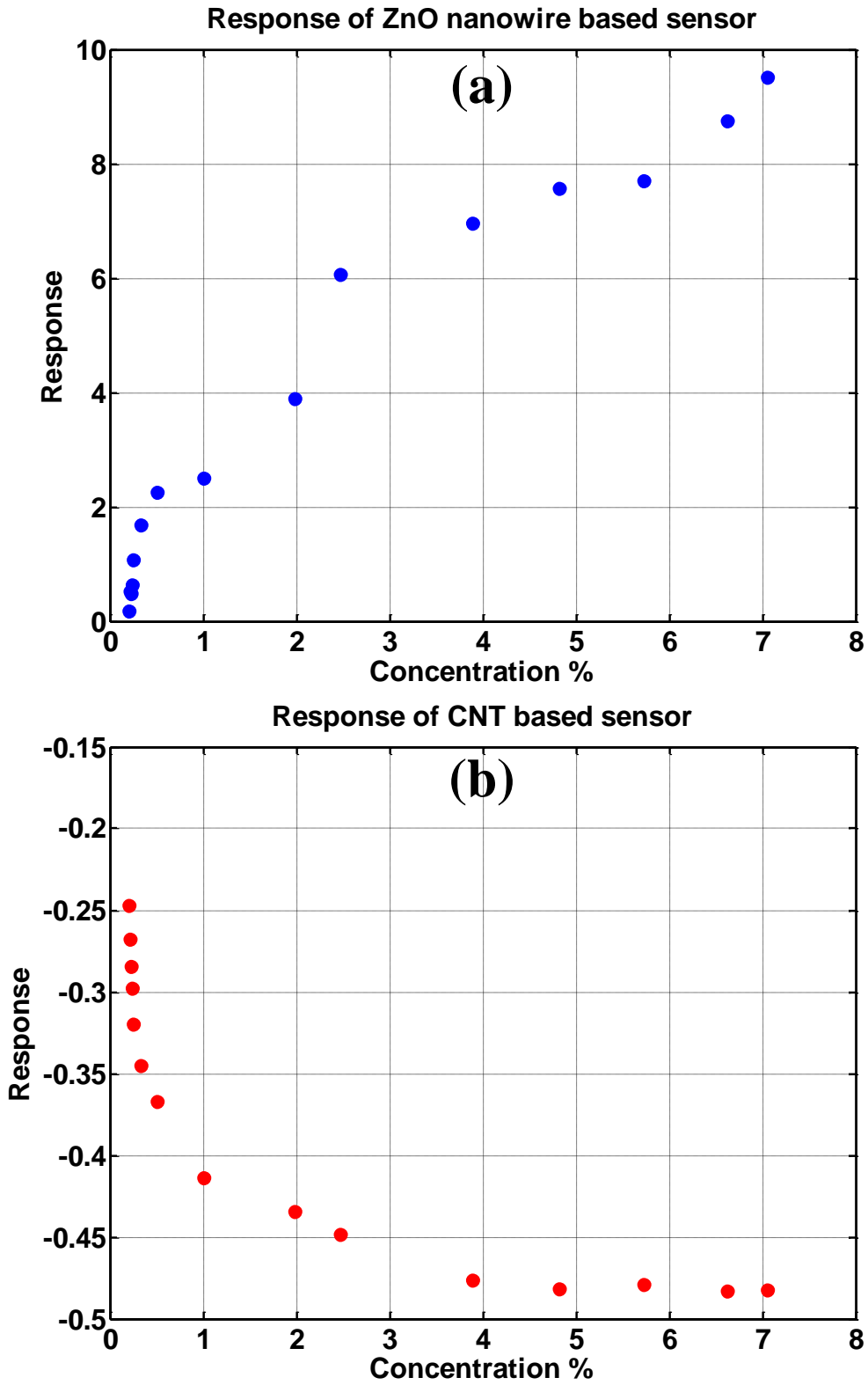


Figure 39. Response of the sensor array in the presence of NH₃ of different concentrations (a) ZnO nanowire based sensor (b) CNT based sensor.

5.5 ESTIMATION OF NH₃ CONCENTRATION

The collected data shown in Figure 39 is summarized in Table 3, with an addition of data at the concentration is 0. Through calibration on the collected data, we want to fit a model that can predict NH₃ concentration given the response of two sensors. Let y denotes real NH₃ concentration, and x_1 and x_2 , the inputs or predictors of the model, represent the response of two sensors, respectively. Through regression methods, a hypothesis model $h(x)$ can be found to predict NH₃ concentrations based on the collected data.

Table 3 Response of two sensors at different concentrations of NH₃

Response of ZnO nanowire based sensor (x_1)	Response of CNT based sensor (x_2)	NH ₃ concentration (%) (y)
0	0	0
0.1850	-0.2473	0.2
0.4892	-0.2675	0.21
0.	-0.2840	0.22
0.6427	-0.2980	0.23
1.0717	-0.3198	0.25
1.6917	-0.3448	0.34
2.2638	-0.3669	0.5
2.4955	-0.4140	1
3.8969	-0.4341	1.98
6.0670	-0.4484	2.47
6.9865	-0.4762	3.89
7.5734	-0.4819	4.82
7.7090	-0.4787	5.73
8.7472	-0.4821	6.62
9.5175	-0.4829	7.06

5.5.1 Model selection

The simplest regression method with two features is linear regression. The hypothesis on NH_3 concentrations is a linear combination of sensor responses x_1 and x_2 ,

$$h_1(x) = \beta_0 + \beta_1 x_1 + \beta_2 x_2, \quad (5.2)$$

where coefficients β_0 , β_1 , and β_2 control how the linear model fit the available observations, and need to be determined separately. Let $h_1(x^{(i)})$ be the prediction for y based on the i th value of x . Then $y^{(i)} - h_1(x^{(i)})$ represents the i th residual – the difference between the i th observed response and the i th predicted response using the linear model. The residual sum of squares (RSS) value for the model is then defined as

$$\text{RSS} = \sum_{i=1}^m \left(y^{(i)} - h_1(x^{(i)}) \right)^2, \quad (5.3)$$

where m is the number of training examples. The least squares rule chooses the coefficients β_j 's to minimize RSS value. In numerical simulation, it is more common to minimize the cost function

$$J(\beta) = \frac{1}{2m} \sum_{i=1}^m \left(y^{(i)} - h_1(x^{(i)}) \right)^2, \quad (5.4)$$

which is usually implemented through gradient descent algorithm.

Algorithm 1. (Gradient descent)

Repeat {

$$\beta_j := \beta_j - \alpha \frac{\partial}{\partial \beta_j} J(\beta) = \begin{cases} \beta_j - \alpha \frac{1}{m} \sum_{i=1}^m (h_1(x^{(i)}) - y^{(i)}) & j = 0 \\ \beta_j - \alpha \frac{1}{m} \sum_{i=1}^m (h_1(x^{(i)}) - y^{(i)}) x_j^{(i)} & j > 0 \end{cases}$$

(simultaneously update β_j for $j = 0, 1, 2$)

}

To ensure fast convergence, every feature needs to be normalized before implementing gradient descent algorithm. The learning rate, α , controls how much the cost function decrease in each step along the derivative direction. Too small α results in slow convergence, while too large α might cause $J(\beta)$ does not converge. After selecting an appropriate α value, the coefficients β_j 's can be determined for the linear model.

Polynomial regression is also a common regression method. We considered quadratic model and cubic model to fit our data. Mathematically, the hypothesis using quadratic model and cubic model are

$$h_2(x) = \beta_0 + \beta_1x_1 + \beta_2x_2 + \beta_3x_1x_2 + \beta_4x_1^2 + \beta_5x_2^2, \quad (5.5)$$

$$h_3(x) = \beta_0 + \beta_1x_1 + \beta_2x_2 + \beta_3x_1x_2 + \beta_4x_1^2 + \beta_5x_2^2 + \beta_6x_1^2x_2 + \beta_7x_1x_2^2 + \beta_8x_1^3 + \beta_9x_2^3. \quad (5.6)$$

Polynomial regressions with higher orders were not considered since they would cause high variance problem. The coefficients in polynomial models, which also minimize RSS values, can be determined similar to linear model regression. Taking quadratic model as an example, besides the original features x_1 and x_2 , the nonlinear features x_1x_2 , x_1^2 , and x_2^2 can be treated as new features. The nonlinear model described in Equation (5.5) is then converted to a general linear regression with multiple features. Therefore, the gradient descent algorithm discussed above can be applied to find the coefficients β_j 's. Similarly, we can fit the data using cubic model shown in Equation (5.6). Notice, it is very important to perform feature scaling before using gradient descent algorithm for nonlinear models, since the newly introduced nonlinear features usually have very different scales compared to the original features x_1 and x_2 .

Before applying regression methods, the total 16 observations shown in Table 3 was randomly split into two sets, a training set containing 13 data, and a test set containing the

remaining 3 observations, as shown in Figure 40. For any supervised learning, the model is trained based on the training data and tested on the test set.

Model selection was implemented by performing k -fold cross-validation method ($k = 5$) on the training set. This approach starts from dividing a set of observations into k folds of approximately equal size. The first fold is held out as a validation set, while the model is fit on the remaining $k - 1$ folds. The mean squared error, MSE_1 , is then computed on the held-out fold. As a different group is held out each time, the procedure is repeat k times and generates k test errors, $MSE_1, MSE_2, \dots, MSE_k$. The average of these errors tells the model's performance using k -fold cross-validation method [82]. Figure 40 illustrates 5-fold cross-validation on one permutation of the training set. We then performed 5-fold cross-validation 10 times on each hypothesis model, as shown in Figure 41. As a result of the variability in how the training examples were divided into 5 folds, there is some variability in the cross-validation errors. The linear model is not suitable for the sensor data since it generates relatively high cross-validation errors. There is not too much difference between quadratic model and cubic model from the view of cross-validation errors. Therefore, quadratic model was selected since cubic model might cause high variance problem.

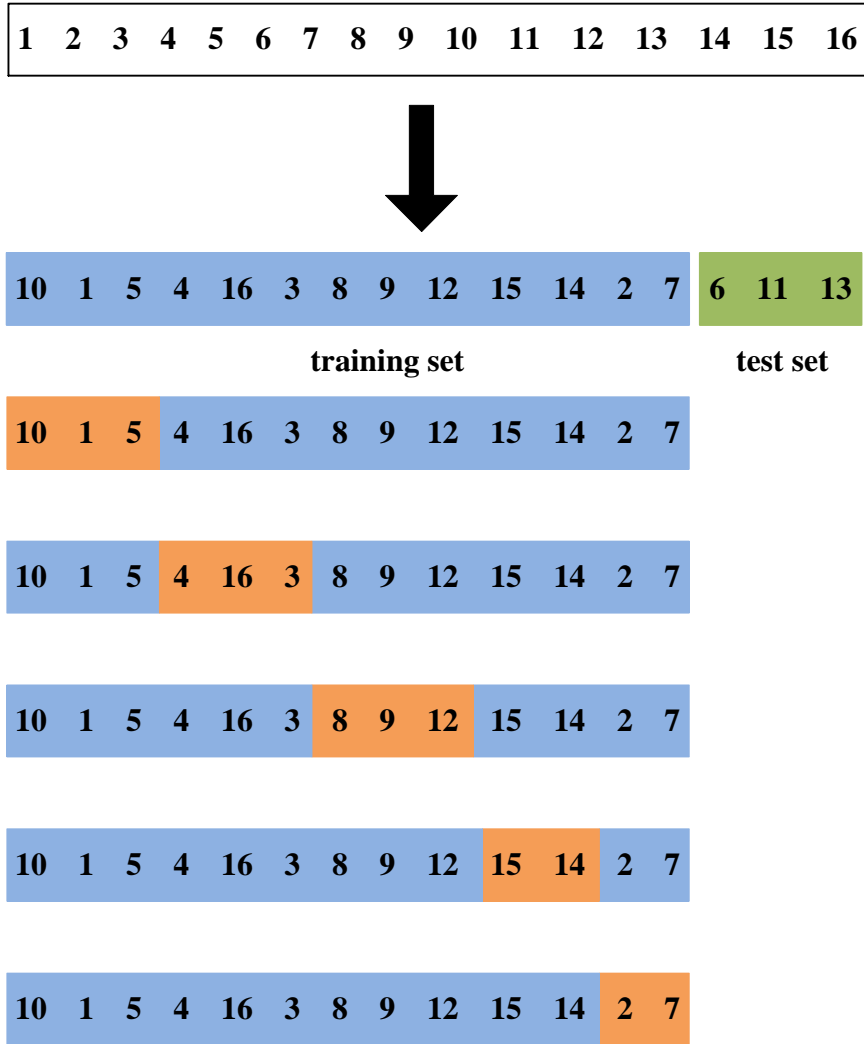


Figure 40. A schematic display of splitting 16 observations into training set and test set, and 5-fold cross-validation. Numbers are indices of data in Table 3. The observations in orange are held out as validation sets.

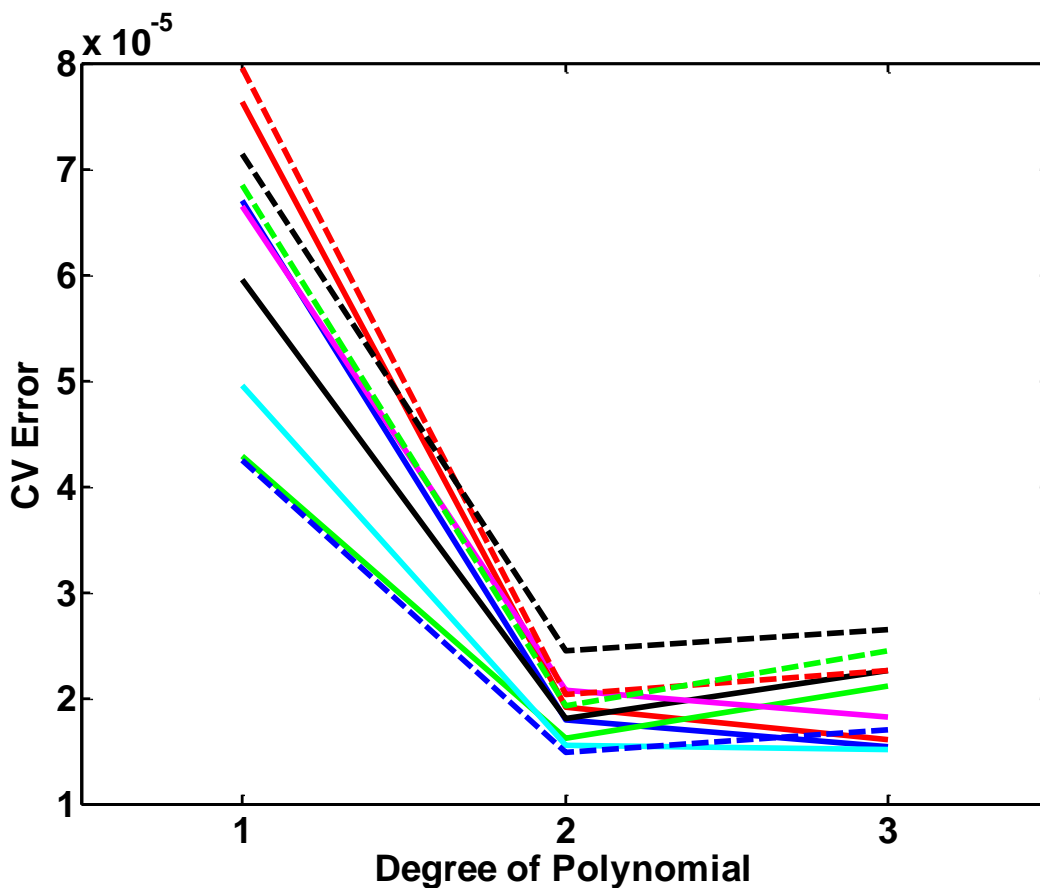


Figure 41. 5-fold cross-validation was implemented 10 times, each with a different random split of the training data.

5.5.2 Quadratic model and regularization

Quadratic model was then fitted on the whole training set and tested on the test set. Figure 42 compares the real concentrations of NH_3 and predicted concentrations using quadratic model on both training set and test set. The mean squared errors on the training set and the test set are 7.23×10^{-6} and 4.79×10^{-5} , respectively. To better visualize the prediction accuracy, the relative prediction error in percentage for each observation in both training set and test set is summarized in Tables 4. Because of the small values of real NH_3 concentrations, it is inevitable

to yield large relative prediction errors on some observations. Nevertheless, more than 6 examples in the training set have relative error less than 20%. And the mean relative prediction error on the training set is 32.83%. However, the performance of the quadratic model on the test set is not satisfactory. Two of the three test examples have more than 20% prediction error, especially the 2nd observation in the test set.

A common technique to improve the prediction accuracy of regression method is called regularization, which shrinks the estimated coefficients β_j 's. This usually can decrease the variance dramatically at the cost of a slight increase in bias. As a powerful tool, ridge regression was applied to regularize the coefficients in quadratic model. Instead of fitting through least squares, ridge regression estimates the coefficients by minimizing

$$\frac{1}{2m} \left[\sum_{i=1}^m (h(x^{(i)}) - y^{(i)})^2 + \lambda \sum_{j=1}^p \beta_j^2 \right] \quad (5.7)$$

where $\lambda \geq 0$ is a tuning parameter that needs to be determined separately. The penalty term $\lambda \sum_{j=1}^p \beta_j^2$ is small when the coefficients β_j 's are close to zero, and therefore it has the effect of shrinking the coefficients β_j 's towards zero. The tuning parameter λ controls the relative impacts of the two terms in Equation (5.7) on the coefficients β_j 's. When $\lambda = 0$, the penalty term has no effect, and ridge regression turns to produce least square estimates, which might results in a high variance problem. When λ approaches to infinity, the impact from the penalty term grows and the coefficient estimates will approach to zero, which usually causes a high bias problem. Therefore, the bias-variance tradeoff requires to select an appropriate λ , which usually is implemented through cross-validation methods. Similar to model selection in Section 5.5.1, 5-fold cross-validation approach was performed in a large range of λ . Fig. 43 shows the cross-validation error for ridge regression predictions, as a function of λ . The cross-validation error drops as λ increases from 0 to 0.658, which indicates that the shrinkage on estimates of β_j 's

leads to a reduction in the variance of the predictions, at the expense of a slightly increased bias. Beyond 0.658, the cross-validation error increases dramatically, which implies the decrease in variance slows while the bias begins to increase substantially. Therefore, 0.658 was picked to serve as the best value of the tuning parameter λ for ridge regression.

Figure 42 compares the real concentrations of NH_3 and predicted concentrations using quadratic model with ridge regularization on both training set and test set. The mean squared errors on the training set and the test set are 8.58×10^{-6} and 4.39×10^{-5} , respectively. The relative prediction error in percentage for each observation in both training set and test set is also summarized in Tables 4. Because of the effect of the penalty term, quadratic model with ridge regression introduces larger bias, therefore increasing both mean squared error and averaged relative prediction error in the training set. On the other hand, it reduces the variance, thereby decreasing both mean squared error and averaged relative prediction error in the test set. With ridge regression, two of the three test examples have relative prediction error less than 20%. However, there is still a relatively large prediction error for the 2nd example in the test set. The large prediction error on this specific data, presumably, is due to the measurement error during the characterization on that point. Nevertheless, ridge regression improved prediction accuracy on the test set, and is supposed to perform better on new unknown observations.

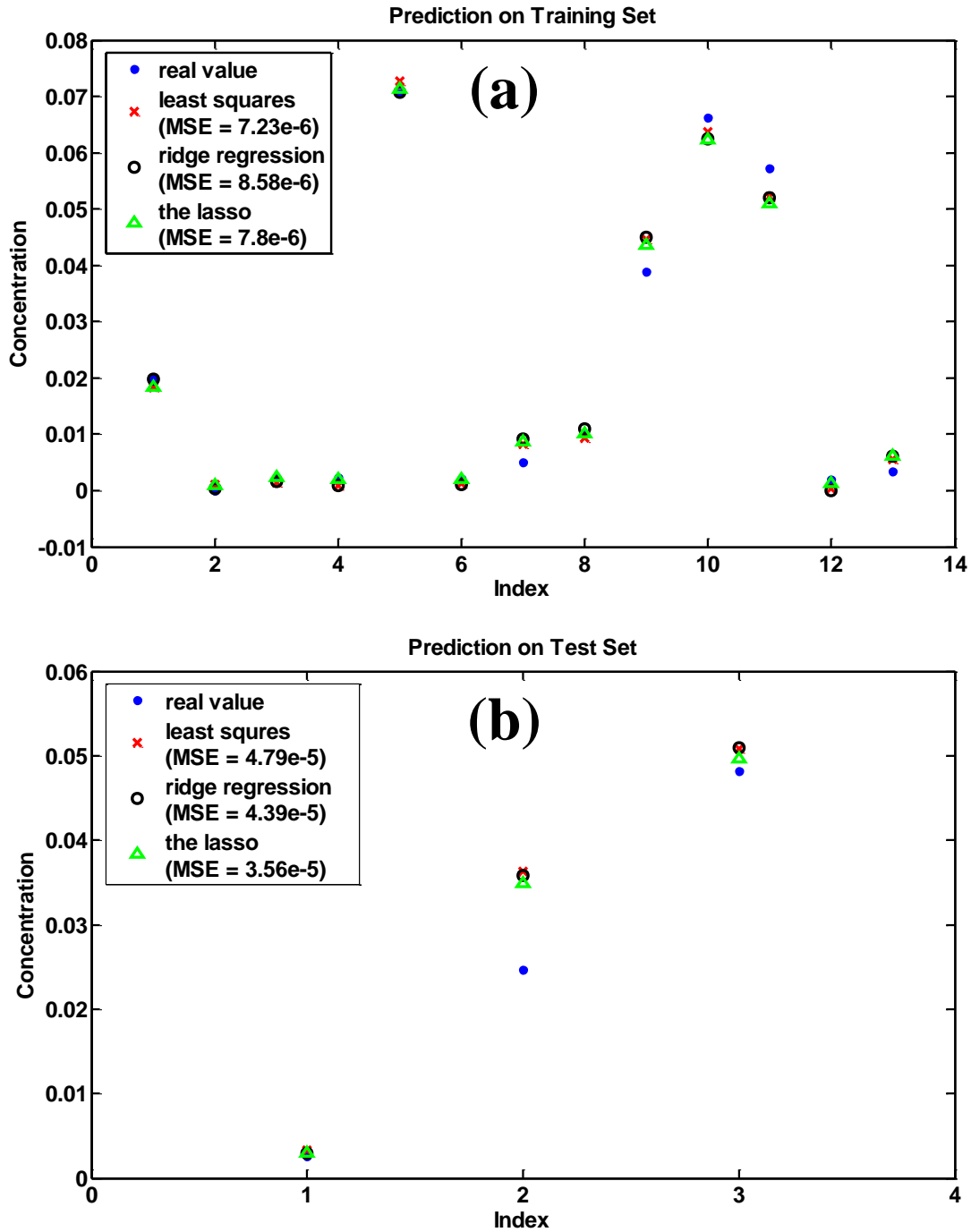


Figure 42. Comparison between real concentrations of NH₃ and predicted concentrations using quadratic model on (a) training set (b) test set.

Table 4 Prediction and relative error of quadratic model and quadratic model with ridge regression on both training set and test set

Training set						
Real NH ₃ concentration	Quadratic model prediction	Relative error of quadratic model (%)	Quadratic model with ridge regression prediction	Relative error of quadratic model with ridge regression (%)	Quadratic model with lasso regression prediction	Relative error of quadratic model with lasso regression (%)
0.0198	0.0184	7.34	0.01978	3.3	0.0183	7.61
0	0.0010	NA	2.6e-4	NA	8.0e-4	NA
0.0023	0.0014	40.05	0.0015	35.07	0.0024	2.13
0.0022	9.8e-4	56.41	9.5e-4	57.60	0.0020	12.70
0.0706	0.0727	3	0.0707	0.13	0.0713	1.07
0.0021	0.0013	40.44	0.0011	47.98	0.0020	2.93
0.0050	0.0083	69.94	0.0092	81.85	0.0087	72.91
0.01	0.0094	5.83	0.0109	8.63	0.0102	1.34
0.0389	0.0447	14.80	0.0450	15.64	0.0436	11.96
0.0662	0.0637	3.76	0.0625	5.54	0.0623	5.82
0.0573	0.0523	8.76	0.0520	9.20	0.0510	10.97
0.0020	3.1e-4	84.95	5.8e-5	97.12	0.0012	41.10
0.0034	0.0055	63.75	0.0061	82.66	0.0061	81.99
Mean relative error (%)		32.84		36.81		21.05
Test set						
Real NH ₃ concentration	Quadratic model prediction	Relative error of quadratic model (%)	Quadratic model with ridge regression prediction	Relative error of quadratic model with ridge regression (%)	Quadratic model with lasso regression prediction	Relative error of quadratic model with lasso regression (%)
0.0025	0.0033	29.59	0.0029	15.16	0.0030	18.82
0.0247	0.0364	47.28	0.0358	45.18	0.0348	41.14
0.0482	0.0508	5.46	0.0509	5.62	0.0497	3.09
Mean relative error (%)		27.44		21.99		21.02

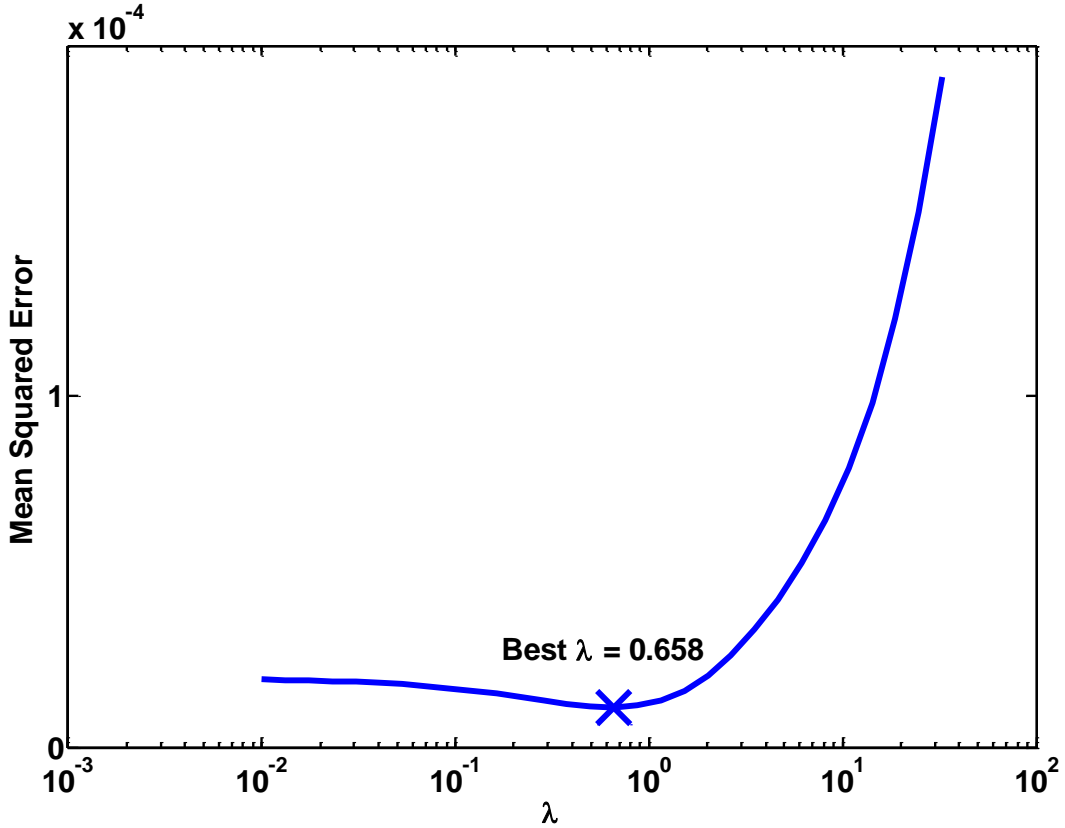


Figure 43. The cross-validation mean squared error for ridge regression predictions, as a function of λ .

Another popular shrinkage method, the lasso, takes a different penalty term. For a given non-negative tuning parameter λ , the lasso solves the problem

$$\min \frac{1}{2m} \left[\sum_{i=1}^m (h(x^{(i)}) - y^{(i)})^2 + \lambda \sum_{j=1}^p |\beta_j| \right]. \quad (5.8)$$

The ℓ_2 penalty $\lambda \sum_{j=1}^p \beta_j^2$ in ridge regression shrinks all the coefficients towards zero, but it will not set any coefficient exactly to zero unless $\lambda = \infty$. In contrast, the ℓ_1 penalty $\lambda \sum_{j=1}^p |\beta_j|$ in the lasso will force some coefficients exactly to zero when λ is large [82]. Therefore, the lasso yields sparse model, or performs variable selection. Similar to ridge regression, the lasso has the effect of reducing variance, therefore improving the accuracy of prediction on the test set. Undoubtedly, the lasso has an advantage over ridge regression in that it produces simpler and

more interpretable model. The prediction accuracy of the two shrinkage methods, however, is specified by the problem involved. Generally, the lasso might perform better when only a small number of predictors have substantial influences, while ridge regression is supposed to predict more accurately when each feature has roughly comparable effect. Therefore, it is essential to implement the lasso to investigate its performance on the sensor data.

Similar to the implementation in ridge regression, 5-fold cross validation approach was performed on the training data to find the appropriate λ value. Fig. 44 shows the cross-validation mean squared error for the lasso predictions, as a function of λ . The minimum cross-validation error was achieved when $\lambda = 9 \times 10^{-4}$. This value was then picked to train the whole training set using the lasso. Figure 42 also compares the real concentrations of NH_3 and predicted concentrations using quadratic model with ridge regularization on both training set and test set. The mean squared errors on the training set and the test set are 7.8×10^{-6} and 3.56×10^{-5} , respectively. The relative prediction error in percentage for each observation in both training set and test set is also summarized in Tables 4. Similar to ridge regression, the penalty term introduced larger bias, therefore increasing mean squared error in the training set. Actually, the lasso performed well in the training set: only three examples have relative prediction error larger than 20%, and the average of the relative prediction error is 21.05%, which is much smaller than quadratic model with least squares and ridge regression. On the other hand, the lasso reduced the variance, thereby decreasing both mean squared error and averaged relative prediction error in the test set. Two of the three test examples have relative prediction error less than 20%, and the average of the relative prediction error is 21.02%. The prediction accuracy on the test set was improved slightly compared to ridge regression, but much better than least squares. The better performance of the lasso is attributed to its ability to generate a sparse model, which could

reduce the variance significantly. Two coefficients, β_2 and β_5 which associate with x_2 and x_2^2 , were shrunk to zero. This implies that the response of CNT based sensor has less substantial contribution than that of ZnO nanowire based sensor, which is reasonable since the response of ZnO nanowire based sensor dominates of the response of CNT based sensor under the same concentration of NH₃, as shown in Figure 39. Therefore, quadratic model with the lasso is supposed to provide best prediction accuracy on the data collected by our sensor array. However, there is still a relatively large prediction error for the 2nd example in the test set. The large prediction error on this specific data, presumably, is due to the measurement error during the characterization on that point.

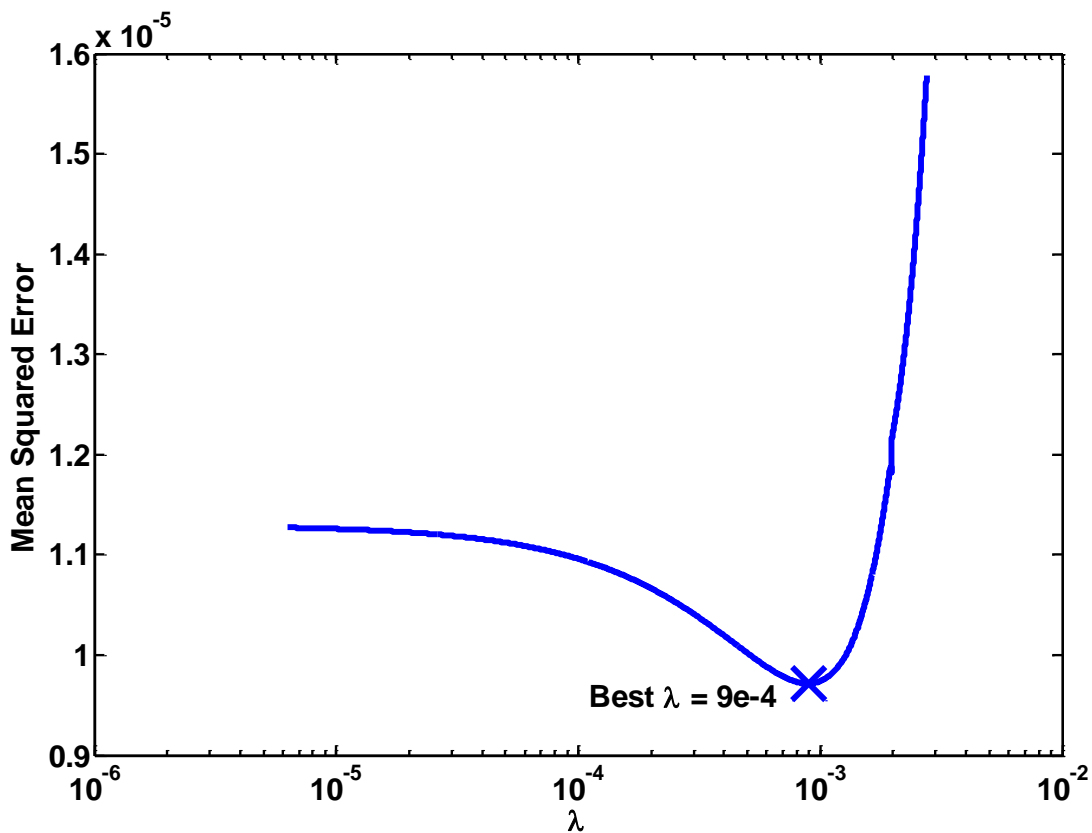


Figure 44. The cross-validation mean squared error for the lasso predictions, as a function of λ .

6.0 DISCUSSION

We have investigated the trajectory of DEP assembled nanowires through simulation and successfully assembled both ZnO nanowires and CNTs across electrodes to form a nano electronic nose. Moreover, we realized NH₃ sensing and fast recovery at room temperature, and proposed regression methods to predict the concentration of NH₃. Overall, the work is comprehensive and solid, yet still deserves further efforts in the following three aspects:

a) Although ZnO nanowires and CNTs can be routinely assembled across electrodes using DEP, the fabricated device usually end up with unpredictable number of nanowires or nanotubes assembled at certain directions, as shown in Figures 20, 21, and 34. The investigation on nanowire's alignment in Section 3.2 unveils the underlying physics. For the uniformity issue, a device with single nanowire or nanotube assembled is highly desirable. The study in Chapter 4 figures out a neighborhood inside which single nanowire is more likely bridge the electrodes, which provides guidance on future study on implementation of single nanowire or nanotube based device. A proposed method is delivering a very small volume of nanowire suspension over the electrode gap region for DEP assembly through micro-pipette. By controlling the volume of nanowire suspension, all the dispersed nanowires are supposed to be inside the figured out neighborhood. By tuning the concentration of the nanowire suspension, the amplitude and frequency of the excitation, and the assembly time, only a small number of nanowires or even single nanowire are supposed to perfectly bridge the electrodes. Moreover, an automation system

can be designed to control the DEP assembly by monitoring the loop through a feedback circuit. Once single nanowire or nanotube has bridge the electrodes, the feedback circuit can detect the change and the automation system can stop the DEP assembly immediately. In addition, a nanorobotic system, which controls the AFM probe to manipulate nanoparticles in nanoscale accuracy, can be introduced to further improve the assembly results [83, 84]. The AFM probe can either bridge unaligned nanowires or move away unintentionally assembled nanowires.

b) We have realized NH_3 sensing and fast recovery at room temperature. The current experimental method exists some limitations and can be significantly improved in the future. First, the current gas sensing chamber is a quartz tube with an approximate size of $80 \text{ cm} \times 6 \text{ cm}$ (length \times diameter). Because of the large size of the quartz tube, it takes several minutes to introduce desired concentration of NH_3 and to refresh the whole chamber with N_2 . And the sensors require dozens of minutes to fully saturate inside the NH_3 environment. A gas sensing chamber with a much smaller size will reduce the time of these process tremendously. Second, the I-V curve of each sensor was collected manually through a source meter. It often required several measurements to determine whether the device is fully saturated or recovered. A more advanced data acquisition system with LABVIEW can monitor the real time conductance change of the transducers. Third, although DC bias has the ability to accelerate the recovery process, it might also burn the device if the generated current density within the nanowire or nanotube is too high. An insightful investigation on the relation between the threshold voltage and the material property will provide protection on the device during the recovery process. Fourth, besides sensing individual gas and predicting the concentration, it is more interesting and challenging to predict the membership and concentration of different gases simultaneously. Because of the low selectivity of nanowire based sensors, additional type of nanowires such as indium oxide (In_2O_3)

nanowire and copper(II) oxide (CuO) nanowire can be integrated to the gas sensor array. More types of chemical vapors such as nitrogen dioxide (NO₂), carbon dioxide (CO₂), and organic vapors like acetone can be utilized as targets gases. Last, an electrical feed through for the chamber and a secure ESD protection should be well designed and implemented for the new gas sensing system.

c) Different regression methods have been implemented on the collected 16 data. Quadratic model with the lasso shows most convincing performance. Strictly, it also cannot provide very satisfactory predictions due to the limited size of observations. Once the gas sensing experiment is substantially improved, it is hopefully to collect large number of examples. Polynomial regressions with higher orders and other powerful regression methods such as splines and neural networks can be executed to yield hopefully more accurate predictions on NH₃ concentrations. Moreover, when we introduce more types of sensors and more kinds of target gases in the future, predicting the membership and concentration of the target gas or even mixed gases will be a very challenging problem. A more complicated model combines regression methods and pattern recognition techniques to produce both quantitative and qualitative responses deserves further investigations. Proposed pattern recognition techniques include principal component analysis, neural networks, and support vector machines.

7.0 CONCLUSION

This work presents a solid study of DEP assembly of nanostructures and its application on NH_3 sensors. The whole work and its accomplishments are summarized as follows:

First, our original contribution to DEP assembly of nanostructures is that we proposed a comprehensive model to investigate the trajectory and ultimate alignment of single nanowire. Besides using a finite element like method to take the non-uniformity of the electric field into consideration, our methodology also applies to the case that the nanowire has an arbitrary orientation with respect to the electric field. The optimized DEP model therefore assists to provide more accurate DEP force and DEP torque. A byproduct of the proposed method is the additional torque caused by DEP forces, which accounts for the rotational motion of the nanowire and eventually affects the final alignment of the nanowire. Other influences like hydrodynamic drag force and drag torque, and Brownian motion are also quantized. The whole model is then constructed to predict the motion of the nanowire. The simulation results on nanowire's 2-D motion demonstrated that the model we proposed is fundamentally and technically feasible to predict the nanostructure's trajectory and alignment.

Second, since there exists some mismatch between the 2-D simulation results and the experimental observations, a more complicated 3-D simulation is imperative to better characterize the motion of nanostructure assembled by DEP. We successfully built the 3-D model based on rigid body dynamics and numerically simulated the motion of single nanowire in

3-D space. A neighborhood inside which the nanowire is more likely bridge the electrodes was then determined, which will help us to better fabricate nanowire based devices in the future. As proposed in Chapter 6, a micro-pipette, an automation system, or even a nanorobotic system can be applied to achieve single nanowire based devices.

Third, we separately assembled ZnO nanowires and CNTs onto the electrode array and tested their performance in NH₃ environment. We demonstrated that both ZnO nanowires and CNTs can well sense NH₃ at room temperature, which circumvented high temperature that usually required in gas sensor application. Moreover, we proposed and successfully implemented fast recovery using DC biases. Therefore, we could repeatedly measure the I-V characteristics of both materials under different NH₃ concentrations. The whole experiment, however, can be tremendously modified to achieve even faster sensing and recovery, real time monitoring, and ability to predict both membership and concentration of target gas, as discussed in Chapter 6.

Finally, we achieved sensor calibration to predict NH₃ concentrations using regression methods. The performance of different regression models were compared using *k*-fold cross validation approach. Quadratic model was selected since it generated small bias and might avoid high variance problem. To improve the prediction accuracy, ridge regression and the lasso were incorporated to further reduce the variance. Once we modify the experiment and collect abundant data in the future, more advanced methods can be implemented to provide better accuracy. Moreover, as we introduce more types of materials and target gases, pattern recognition techniques can also be introduced to predict the membership and concentration of target gas simultaneously.

BIBLIOGRAPHY

- [1] P. T. Moseley, "Solid state gas sensors," *Measurement Science & Technology*, vol. 8, no. 3, pp. 223-237, Mar, 1997.
- [2] G. Martinelli, and M. C. Carotta, "Thick-Film Gas Sensors," *Sensors and Actuators B-Chemical*, vol. 23, no. 2-3, pp. 157-161, Feb, 1995.
- [3] D. S. Lee, S. D. Han, J. S. Huh, and D. D. Lee, "Nitrogen oxides-sensing characteristics of WO₃-based nanocrystalline thick film gas sensor," *Sensors and Actuators B-Chemical*, vol. 60, no. 1, pp. 57-63, Nov 2, 1999.
- [4] N. J. Dayan, S. R. Sainkar, R. N. Karekar, and R. C. Aiyer, "Formulation and characterization of ZnO : Sb thick-film gas sensors," *Thin Solid Films*, vol. 325, no. 1-2, pp. 254-258, Jul 18, 1998.
- [5] H. Gong, J. Q. Hu, J. H. Wang, C. H. Ong, and F. R. Zhu, "Nano-crystalline Cu-doped ZnO thin film gas sensor for CO," *Sensors and Actuators B-Chemical*, vol. 115, no. 1, pp. 247-251, May 23, 2006.
- [6] Z. L. Wang, "Zinc oxide nanostructures: growth, properties and applications," *Journal of Physics-Condensed Matter*, vol. 16, no. 25, pp. R829-R858, Jun 30, 2004.
- [7] Z. L. Wang, "ZnO nanowire and nanobelt platform for nanotechnology," *Materials Science & Engineering R-Reports*, vol. 64, no. 3-4, pp. 33-71, Apr 3, 2009.
- [8] T. J. Hsueh, C. L. Hsu, S. J. Chang, and I. C. Chen, "Laterally grown ZnO nanowire ethanol gas sensors," *Sensors and Actuators B-Chemical*, vol. 126, no. 2, pp. 473-477, Oct 1, 2007.
- [9] L. Liao, H. B. Lu, M. Shuai, J. C. Li, Y. L. Liu, C. Liu, Z. X. Shen, and T. Yu, "A novel gas sensor based on field ionization from ZnO nanowires: moderate working voltage and high stability," *Nanotechnology*, vol. 19, no. 17, Apr 30, 2008.
- [10] Q. Wan, Q. H. Li, Y. J. Chen, T. H. Wang, X. L. He, J. P. Li, and C. L. Lin, "Fabrication and ethanol sensing characteristics of ZnO nanowire gas sensors," *Applied Physics Letters*, vol. 84, no. 18, pp. 3654-3656, May 3, 2004.

- [11] H. T. Wang, B. S. Kang, F. Ren, L. C. Tien, P. W. Sadik, D. P. Norton, S. J. Pearton, and J. Lin, "Hydrogen-selective sensing at room temperature with ZnO nanorods," *Applied Physics Letters*, vol. 86, no. 24, Jun 13, 2005.
- [12] C. Li, D. H. Zhang, X. L. Liu, S. Han, T. Tang, J. Han, and C. W. Zhou, "In₂O₃ nanowires as chemical sensors," *Applied Physics Letters*, vol. 82, no. 10, pp. 1613-1615, Mar, 2003.
- [13] E. L. Hines, E. Llobet, and J. W. Gardner, "Electronic noses: a review of signal processing techniques," *Iee Proceedings-Circuits Devices and Systems*, vol. 146, no. 6, pp. 297-310, Dec, 1999.
- [14] Y. N. Xia, P. D. Yang, Y. G. Sun, Y. Y. Wu, B. Mayers, B. Gates, Y. D. Yin, F. Kim, and Y. Q. Yan, "One-dimensional nanostructures: Synthesis, characterization, and applications," *Advanced Materials*, vol. 15, no. 5, pp. 353-389, Mar 4, 2003.
- [15] A. I. Hochbaum, R. Fan, R. R. He, and P. D. Yang, "Controlled growth of Si nanowire arrays for device integration," *Nano Letters*, vol. 5, no. 3, pp. 457-460, Mar, 2005.
- [16] J. X. Wang, X. W. Sun, Y. Yang, H. Huang, Y. C. Lee, O. K. Tan, and L. Vayssieres, "Hydrothermally grown oriented ZnO nanorod arrays for gas sensing applications," *Nanotechnology*, vol. 17, no. 19, pp. 4995-4998, Oct 14, 2006.
- [17] X. C. Jiang, T. Herricks, and Y. N. Xia, "CuO nanowires can be synthesized by heating copper substrates in air," *Nano Letters*, vol. 2, no. 12, pp. 1333-1338, Dec, 2002.
- [18] Z. Q. Gao, A. Agarwal, A. D. Trigg, N. Singh, C. Fang, C. H. Tung, Y. Fan, K. D. Buddharaju, and J. M. Kong, "Silicon nanowire arrays for label-free detection of DNA," *Analytical Chemistry*, vol. 79, no. 9, pp. 3291-3297, May 1, 2007.
- [19] E. Stern, J. F. Klemic, D. A. Routenberg, P. N. Wyrembak, D. B. Turner-Evans, A. D. Hamilton, D. A. LaVan, T. M. Fahmy, and M. A. Reed, "Label-free immunodetection with CMOS-compatible semiconducting nanowires," *Nature*, vol. 445, no. 7127, pp. 519-522, Feb 1, 2007.
- [20] O. Englander, D. Christensen, J. Kim, L. Lin, and S. J. Morris, "Electric-field assisted growth and self-assembly of intrinsic silicon nanowires," *Nano Lett*, vol. 5, no. 4, pp. 705-8, Apr, 2005.
- [21] S. Raychaudhuri, S. A. Dayeh, D. L. Wang, and E. T. Yu, "Precise Semiconductor Nanowire Placement Through Dielectrophoresis," *Nano Letters*, vol. 9, no. 6, pp. 2260-2266, Jun, 2009.
- [22] J. Q. Li, Q. Zhang, D. J. Yang, and J. Z. Tian, "Fabrication of carbon nanotube field effect transistors by AC dielectrophoresis method," *Carbon*, vol. 42, no. 11, pp. 2263-2267, 2004.

- [23] B. Messer, J. H. Song, and P. D. Yang, "Microchannel networks for nanowire patterning," *Journal of the American Chemical Society*, vol. 122, no. 41, pp. 10232-10233, Oct 18, 2000.
- [24] Y. Huang, X. F. Duan, Q. Q. Wei, and C. M. Lieber, "Directed assembly of one-dimensional nanostructures into functional networks," *Science*, vol. 291, no. 5504, pp. 630-633, Jan 26, 2001.
- [25] F. Kim, S. Kwan, J. Akana, and P. D. Yang, "Langmuir-Blodgett nanorod assembly," *Journal of the American Chemical Society*, vol. 123, no. 18, pp. 4360-4361, May 9, 2001.
- [26] A. Tao, F. Kim, C. Hess, J. Goldberger, R. R. He, Y. G. Sun, Y. N. Xia, and P. D. Yang, "Langmuir-Blodgett silver nanowire monolayers for molecular sensing using surface-enhanced Raman spectroscopy," *Nano Letters*, vol. 3, no. 9, pp. 1229-1233, Sep, 2003.
- [27] P. D. Yang, and F. Kim, "Langmuir-Blodgett assembly of one-dimensional nanostructures," *Chemphyschem*, vol. 3, no. 6, pp. 503-+, Jun 17, 2002.
- [28] B. He, T. J. Morrow, and C. D. Keating, "Nanowire sensors for multiplexed detection of biomolecules," *Current Opinion in Chemical Biology*, vol. 12, no. 5, pp. 522-528, Oct, 2008.
- [29] H. A. Pohl, *Dielectrophoresis*, London: Cambridge University Press, 1978.
- [30] T. B. Jones, *Electromechanics of Particles*: Cambridge University Press, 1995.
- [31] H. G. Morgan, N. G., *AC Electrokinetics: colloids and nanoparticles*: Research Studies Press Ltd., 2003.
- [32] A. Kolmakov, Y. X. Zhang, G. S. Cheng, and M. Moskovits, "Detection of CO and O₂ using tin oxide nanowire sensors," *Advanced Materials*, vol. 15, no. 12, pp. 997-+, Jun 17, 2003.
- [33] D. H. Zhang, Z. Q. Liu, C. Li, T. Tang, X. L. Liu, S. Han, B. Lei, and C. W. Zhou, "Detection of NO₂ down to ppb levels using individual and multiple In₂O₃ nanowire devices," *Nano Letters*, vol. 4, no. 10, pp. 1919-1924, Oct, 2004.
- [34] R. Konenkamp, R. C. Word, and C. Schlegel, "Vertical nanowire light-emitting diode," *Applied Physics Letters*, vol. 85, no. 24, pp. 6004-6006, Dec 13, 2004.
- [35] S. D. Hersee, M. Fairchild, A. K. Rishinaramangalam, M. S. Ferdous, L. Zhang, P. M. Varangis, B. S. Swartzentruber, and A. A. Talin, "GaN nanowire light emitting diodes based on templated and scalable nanowire growth process," *Electronics Letters*, vol. 45, no. 1, pp. 75-U24, Jan 1, 2009.
- [36] C. T. Black, "Self-aligned self assembly of multi-nanowire silicon field effect transistors," *Applied Physics Letters*, vol. 87, no. 16, Oct 17, 2005.

- [37] S. N. Cha, J. E. Jang, Y. Choi, G. A. J. Amaratunga, G. W. Ho, M. E. Welland, D. G. Hasko, D. J. Kang, and J. M. Kim, "High performance ZnO nanowire field effect transistor using self-aligned nanogap gate electrodes," *Applied Physics Letters*, vol. 89, no. 26, Dec 25, 2006.
- [38] T. Zhang, S. Mubeen, N. V. Myung, and M. A. Deshusses, "Recent progress in carbon nanotube-based gas sensors," *Nanotechnology*, vol. 19, no. 33, Aug 20, 2008.
- [39] P. G. Collins, K. Bradley, M. Ishigami, and A. Zettl, "Extreme oxygen sensitivity of electronic properties of carbon nanotubes," *Science*, vol. 287, no. 5459, pp. 1801-1804, Mar 10, 2000.
- [40] L. Valentini, C. Cantalini, I. Armentano, J. M. Kenny, L. Lozzi, and S. Santucci, "Investigation of the NO₂ sensitivity properties of multiwalled carbon nanotubes prepared by plasma enhanced chemical vapor deposition," *Journal of Vacuum Science & Technology B*, vol. 21, no. 5, pp. 1996-2000, Sep-Oct, 2003.
- [41] Z. Y. Fan, and J. G. Lu, "Gate-refreshable nanowire chemical sensors," *Applied Physics Letters*, vol. 86, no. 12, Mar 21, 2005.
- [42] Z. Y. Fan, and J. G. Lu, "Chemical sensing with ZnO nanowire field-effect transistor," *Ieee Transactions on Nanotechnology*, vol. 5, no. 4, pp. 393-396, Jul, 2006.
- [43] J. J. Wu, and S. C. Liu, "Low-temperature growth of well-aligned ZnO nanorods by chemical vapor deposition," *Advanced Materials*, vol. 14, no. 3, pp. 215-+, Feb 5, 2002.
- [44] L. E. Greene, B. D. Yuhas, M. Law, D. Zitoun, and P. D. Yang, "Solution-grown zinc oxide nanowires," *Inorganic Chemistry*, vol. 45, no. 19, pp. 7535-7543, Sep 18, 2006.
- [45] Z. Y. Fan, D. W. Wang, P. C. Chang, W. Y. Tseng, and J. G. Lu, "ZnO nanowire field-effect transistor and oxygen sensing property," *Applied Physics Letters*, vol. 85, no. 24, pp. 5923-5925, Dec 13, 2004.
- [46] Q. H. Li, Y. X. Liang, Q. Wan, and T. H. Wang, "Oxygen sensing characteristics of individual ZnO nanowire transistors," *Applied Physics Letters*, vol. 85, no. 26, pp. 6389-6391, Dec 27, 2004.
- [47] B. S. Kang, Y. W. Heo, L. C. Tien, D. P. Norton, F. Ren, B. P. Gila, and S. J. Pearton, "Hydrogen and ozone gas sensing using multiple ZnO nanorods," *Applied Physics a-Materials Science & Processing*, vol. 80, no. 5, pp. 1029-1032, Feb, 2005.
- [48] T. J. Hsueh, Y. W. Chen, S. J. Chang, S. F. Wang, C. L. Hsu, Y. R. Lin, T. S. Lin, and I. C. Chen, "ZnO nanowire-based CO sensors prepared at various temperatures," *Journal of the Electrochemical Society*, vol. 154, no. 12, pp. J393-J396, 2007.
- [49] T. J. Hsueh, Y. W. Chen, S. J. Chang, S. F. Wang, C. L. Hsu, Y. R. Lin, T. S. Lin, and I. C. Chen, "ZnO nanowire-based CO sensors prepared on patterned ZnO : Ga/SiO₂/Si

- templates,” *Sensors and Actuators B-Chemical*, vol. 125, no. 2, pp. 498-503, Aug 8, 2007.
- [50] J. B. K. Law, and J. T. L. Thong, “Improving the NH₃ gas sensitivity of ZnO nanowire sensors by reducing the carrier concentration,” *Nanotechnology*, vol. 19, no. 20, May 21, 2008.
- [51] M. W. Ahn, K. S. Park, J. H. Heo, J. G. Park, D. W. Kim, K. J. Choi, J. H. Lee, and S. H. Hong, “Gas sensing properties of defect-controlled ZnO-nanowire gas sensor,” *Applied Physics Letters*, vol. 93, no. 26, Dec 29, 2008.
- [52] C. H. Wang, X. F. Chu, and M. W. Wu, “Detection of H₂S down to ppb levels at room temperature using sensors based on ZnO nanorods,” *Sensors and Actuators B-Chemical*, vol. 113, no. 1, pp. 320-323, Jan 17, 2006.
- [53] W. An, X. J. Wu, and X. C. Zeng, “Adsorption of O₂, H₂, CO, NH₃, and NO₂ on ZnO nanotube: A density functional theory study,” *Journal of Physical Chemistry C*, vol. 112, no. 15, pp. 5747-5755, Apr 17, 2008.
- [54] J. Kong, N. R. Franklin, C. W. Zhou, M. G. Chapline, S. Peng, K. J. Cho, and H. J. Dai, “Nanotube molecular wires as chemical sensors,” *Science*, vol. 287, no. 5453, pp. 622-625, Jan 28, 2000.
- [55] T. Someya, J. Small, P. Kim, C. Nuckolls, and J. T. Yardley, “Alcohol vapor sensors based on single-walled carbon nanotube field effect transistors,” *Nano Letters*, vol. 3, no. 7, pp. 877-881, Jul, 2003.
- [56] J. Kong, M. G. Chapline, and H. J. Dai, “Functionalized carbon nanotubes for molecular hydrogen sensors,” *Advanced Materials*, vol. 13, no. 18, pp. 1384-1386, Sep 14, 2001.
- [57] K. G. Ong, K. F. Zeng, and C. A. Grimes, “A Wireless, Passive Carbon Nanotube-Based Gas Sensor,” *Ieee Sensors Journal*, vol. 2, no. 2, pp. 82-88, Apr, 2002.
- [58] Y. J. Lu, J. Li, J. Han, H. T. Ng, C. Binder, C. Partridge, and M. Meyyappan, “Room temperature methane detection using palladium loaded single-walled carbon nanotube sensors,” *Chemical Physics Letters*, vol. 391, no. 4-6, pp. 344-348, Jun 21, 2004.
- [59] C. Dinatale, F. Davide, and A. Damico, “Pattern-Recognition in Gas-Sensing - Well- Stated Techniques and Advances,” *Sensors and Actuators B-Chemical*, vol. 23, no. 2-3, pp. 111-118, Feb, 1995.
- [60] J. Gimsa, “A comprehensive approach to electro-orientation, electrodeformation, dielectrophoresis, and electrorotation of ellipsoidal particles and biological cells,” *Bioelectrochemistry*, vol. 54, no. 1, pp. 23-31, Aug, 2001.
- [61] Y. J. Kang, D. Q. Li, S. A. Kalams, and J. E. Eid, “DC-Dielectrophoretic separation of biological cells by size,” *Biomedical Microdevices*, vol. 10, no. 2, pp. 243-249, Apr, 2008.

- [62] X. J. Wang, X. B. Wang, and P. R. C. Gascoyne, "General expressions for dielectrophoretic force and electrorotational torque derived using the Maxwell stress tensor method," *Journal of Electrostatics*, vol. 39, no. 4, pp. 277-295, Aug, 1997.
- [63] H. A. Pohl, and J. S. Crane, "Dielectrophoretic Force," *Journal of Theoretical Biology*, vol. 37, no. 1, pp. 1-&, 1972.
- [64] G. Schwarz, "General Equation for Mean Electrical Energy of a Dielectric Body in an Alternating Electrical Field," *Journal of Chemical Physics*, vol. 39, no. 9, pp. 2387-&, 1963.
- [65] L. D. Sher, "Dielectrophoresis in Lossy Dielectric Media," *Nature*, vol. 220, no. 5168, pp. 695-&, 1968.
- [66] V. P. Pastushenko, P. I. Kuzmin, and Y. A. Chizmadzhev, "Dielectrophoresis and Electrorotation of Cells - Unified Theory for Spherically Symmetric Cells with Arbitrary Structure of Membrane," *Biologicheskie Membrany*, vol. 5, no. 1, pp. 65-78, Jan, 1988.
- [67] E. R. Mognaschi, and A. Savini, "The Action of a Non-Uniform Electric-Field Upon Lossy Dielectric Systems Ponderomotive Force on a Dielectric Sphere in the Field of a Point-Charge," *Journal of Physics D-Applied Physics*, vol. 16, no. 8, pp. 1533-1541, 1983.
- [68] R. Krupke, F. Hennrich, M. M. Kappes, and H. V. Lohneysen, "Surface conductance induced dielectrophoresis of semiconducting single-walled carbon nanotubes," *Nano Letters*, vol. 4, no. 8, pp. 1395-1399, Aug, 2004.
- [69] H. C. Berg, *Random Walks in Biology*: Princeton University Press, 1993.
- [70] K. Keshoju, H. Xing, and L. Sun, "Magnetic field driven nanowire rotation in suspension," *Applied Physics Letters*, vol. 91, no. 12, Sep 17, 2007.
- [71] W. B. S. Russel, D. A.; Schowalter, W. R., *Colloidal Dispersions*: Cambridge University Press, 1989.
- [72] Y. Han, A. M. Alsayed, M. Nobili, J. Zhang, T. C. Lubensky, and A. G. Yodh, "Brownian motion of an ellipsoid," *Science*, vol. 314, no. 5799, pp. 626-630, Oct 27, 2006.
- [73] C. T. Chen, *Linear System Theory and Design*: Oxford University Press, 1999.
- [74] D. L. Fan, F. Q. Zhu, R. C. Cammarata, and C. L. Chien, "Controllable high-speed rotation of nanowires," *Physical Review Letters*, vol. 94, no. 24, Jun 24, 2005.
- [75] D. T. Greenwood, *Advanced Dynamics*: Cambridge University Press, 2003.
- [76] L. Meirovitch, *Methods of Analytical Dynamics*: McGraw-Hill Book Company, 1970.

- [77] U. M. P. Ascher, L. R., *Computer Methods for Ordinary Differential Equations and Differential Algebraic Equations*: Philadelphia : Society for Industrial and Applied Mathematics, 1998.
- [78] K. E. Atkinson, *An Introduction to Numerical Analysis*: New York : Wiley, 1989.
- [79] Y. S. Hu, D. Perello, U. Mushtaq, and M. H. Yun, "A Single Palladium Nanowire Via Electrophoresis Deposition Used as a Ultrasensitive Hydrogen Sensor," *Ieee Transactions on Nanotechnology*, vol. 7, no. 6, pp. 693-699, Nov, 2008.
- [80] C. S. Rout, M. Hegde, A. Govindaraj, and C. N. Rrao, "Ammonia sensors based on metal oxide nanostructures," *Nanotechnology*, vol. 18, no. 20, May 23, 2007.
- [81] J. Li, Y. J. Lu, Q. Ye, M. Cinke, J. Han, and M. Meyyappan, "Carbon nanotube sensors for gas and organic vapor detection," *Nano Letters*, vol. 3, no. 7, pp. 929-933, Jul, 2003.
- [82] G. James, D. Witten, T. Hastie, and R. Tibshirani, *An Introduction to Statistical Learning with Applications in R*, p.^pp. 441: Springer, 2013.
- [83] G. Y. Li, N. Xi, M. M. Yu, and W. K. Fung, "Development of augmented reality system for AFM-based nanomanipulation," *Ieee-Asme Transactions on Mechatronics*, vol. 9, no. 2, pp. 358-365, Jun, 2004.
- [84] G. Y. Li, N. Xi, H. P. Chen, C. Pomeroy, and M. Prokos, "'Videolized" atomic force microscopy for interactive nanomanipulation and nanoassembly," *Ieee Transactions on Nanotechnology*, vol. 4, no. 5, pp. 605-615, Sep, 2005.